Profilometry with volume holographic imaging

by

Wenyang Sun

Submitted to the Department of Mechanical Engineering
in partial fulfillment of the requirements for the degree of

Doctor of Philosophy in Mechanical Engineering

at the

MASSACHUSETTS INSTITUTE OF TECHNOLOGY

June 2006

Author ....
Department of Mechanical Engineering
May 04, 2006

Certified by ....
George Barbastathis
Associate Professor
Thesis Supervisor

Accepted by ....
Lallit Anand
Chairman, Department Committee on Graduate Students

Profilometry with volume holographic imaging

by

Wenyang Sun

Submitted to the Department of Mechanical Engineering
on May 04, 2006, in partial fulfillment of the
requirements for the degree of
Doctor of Philosophy in Mechanical Engineering

Abstract

High resolution, non-contact object profile measurement (profilometry) at long working distance is important in a number of application areas, such as precise parts manufacturing, optical element grounding and polishing, adversary target identification in military, terrace profiling, etc. The Volume Holographic (VH) lens is a novel optical element which process the incident light field in a 3D fashion. It has been shown with promising applications in object profile acquisition and 3D imaging areas. In this thesis, we propose, design and implemented a number of volume holographic computational imaging systems for profilometry related applications. We show that the rich functionalities of the VH lens can be exploited to process the incident optical field. Some of the unique imaging behavior can not be easily achieved by using conventional optics. We first develop the theoretical framework for investigating the VH lens optical behavior. We concentrate on a simple design: using the VH lens as the spatial spectrum plane filter in a $4F$ imaging system. We derived the point spread function (PSF), the depth resolution, the diffraction field distribution of the proposed imaging system. Experimental system characterization and profilometry measurements were carried out with our setups. We find the resolution of the volume holographic imaging (VHI) profilometry system degrades quadratically with the increase of working distance. We addressed this problem by two approaches:

1. We discuss the effect of objective optics design on the VHI resolution. We proposed and implemented the use of appropriately designed telephoto objective optics to achieve very good resolution at long working distance.

2. We developed a maximum likelihood estimation based post-processing method to improve the depth resolution by more than 5 times.

An important issue on VHI profilometry is the "slit-shaped" limited field of view (FoV). This makes measurement over the entire big object is very time consuming because scanning is necessary. Otherwise hundreds or thousands of VH lenses must be multiplexed on a single crystal to concatenate the slit FoV of each VH lens to form a wide exit window. However the multiplexing method suffers the "M/#" penalty on photon efficiency. We solved this problem by utilizing the wavelength degeneracy of the VH lens and designed a rainbow illumination VHI to expand the FoV. We also extended the application of VHI to hyper-spectral imaging. The experimental implementation of the hyper-spectral imaging system shows it is capable of not only reconstructing the 3D spatial profile but also restoring the spectral information of the object, both at high resolution. Finally, we conclude with some directions for the future work in this emerging field.

Thesis Supervisor: George Barbastathis
Title: Associate Professor

Acknowledgments

Firstly, I would like to thank my advisor Prof. George Barbastathis. I exposed to related research area before I came to MIT but lack of solid physics background which is necessary to diffraction optics and optical imaging research, as well as the optics lab working experience. He has been warmly and patiently guiding me during the course of my research and giving me many helpful suggestion. More importantly, he silently impressed me with his passion on scientific research. His humor brought our research group a lot of fun in the past four years. I also enjoyed many fantastic trips together with him to conferences. He is my academic advisor, but at most of the time, more like elder friend. For all of this, I will forever be grateful to him.

I would also like to thank my thesis committee. Professors Mark A. Neifeld, Jeffrey H. Shapiro and Daniela, Pucci De Farias for taking time to offer valuable advice about my work. I thoroughly appreciated the discussion we had and suggestions you gave in my research.

I would also like to thank my colleges (past and present) at the 3D Optical Systems group for all their help and many helpful discussion: Andy Stein, Carlos Hidrovo, Greg Nielson, Hyun-Jin In, Jose A. Dominguez-Caballero, Laura A Waller, Mirco Vitr, Paul Stellman, Satoshi Takahashi, Sebaek Oh, Stan Jurga, Tina Shih, Tony John, Troy Savoie, Wei-Chuan Shih, Will Aora, Zao Xu. Especially, I want to thank Arnab Sinha and Kehan Tian for their many helps in brainstorming, and setting up the various experiments.

Lastly I would like to thank my family: Dad and mom for their always support and encouragement, especially my wife Yana for her selfishness contribution to our new little family. Her support has being so important to me to finish all this work.

Contents

List of Figures

List of Tables

Chapter 1

Introduction

Imaging technology [1, 2] remains a main research branch of optics. Recently, the rapid development of semiconductor technology made high performance CCD/CMOS imagers and powerful microprocessors available at extremely low cost. This led to increasing research interests on computational imaging, which incorporates traditional and novel optical elements, electronic optical sensors and image post-processing algorithms. A Computational Imaging System (CIS) [3, 4] receives emitted or scattered radiation from an object of interest and transforms this radiation optically before capturing it as an electronic signal on a photoelectric detector or detector array. The transduced signal is then digitally processed to recover object attributes, such as spatial structure and spectral composition.

In general, the hardware of a CIS consists of two categories of elements:

1. Analog optical information transfer elements, such as lenses, mirrors, waveplates, which directly capture the input optical radiation and perform information transformation (refraction, reflection, wavefront retardation, *etc.*) in parallel and generate the output optical radiation.
2. Analog/Digital and Digital/Analog optical information transfer elements, such as CCD/CMOS cameras, Spatial Light Modulators (SLM).

In addition to the hardwares mentioned above, post-processing algorithms are usually necessary to enhance or reconstruct the final image from the raw information captured by CCD/CMOS imagers. In general, for a CIS, the raw image might consist of optical field/intensity distributions that are geometrically similar to the original object, but not necessarily. The raw image might be formed through interaction of the optical radiation with non-imaging optical elements, resulting in interference fringes, speckles, *etc.* Even through these light intensity patterns do not look like traditional images, they still contain the information necessary to reconstruct the original object.

In this thesis, we focus on the recovery of spatial structure from objects of interest, so we classify imaging systems of relevance as follows:

1. Two-dimensional (2D) imaging systems typically recover only the 2D irradiance or intensity information about an object, as shown in Figure 1-1(a). In other words, a 2D image is of the form $I(x, y)$, an intensity distribution defined over the lateral coordinates. The imaging system does not possess the ability to discriminate the distance between the object and the imaging system itself with out digital post-processing. There are post-processing algorithms such as depth from defocus, which can estimate the depth information from the shift invariant defocus response of the camera lens. However, with little prior knowledge of complex scene, this method is very unreliable and usually fails. Photographic cameras and traditional microscopes are examples of 2D imaging systems.

2. Three-dimensional (3D) imaging systems recover the entire 3D intensity information about the object, as shown in Figure 1-1(b). For 3D imaging, the object is required to be at least partially translucent. Thus, a 3D image is of the form $I(x, y, z)$, *i.e.*, a complete 3D intensity distribution. Fluorescence confocal microscopy [5] and optical coherence tomography [6] are examples of 3D imaging methods. Another class of 3D imaging systems is referred to as tomography, *e.g.*, such as x-ray computerized tomography (CT) and magnetic resonance imaging (MRI) [7]. In tomographic systems, the object information is retrieved as a set of projections, and the Radon transform inversion or other techniques map the information back to native object coordinates.

3. Two and One-Half-Dimensional ($2\frac{1}{2}$D) imaging systems [8, 9] also referred to

as profilometers, are typically used for reflective objects. The basic principle of profilometer is similar to that of 3D imaging systems. They both have depth discrimination ability, which allows them to recover, in additional to the lateral 2D image, the depth information of the object, which can not be accquired by the 2D imaging. The difference is that profilometers work on opaque ($2\frac{1}{2}$D) object. These objects are most commonly seen in the natural world (in visible wavelength range), their reflective profile exist on a 2D manifold in the 3D spatial space. The profilometer returns a height map $z(x, y)$ representing the distance of a particular point on the surface from a fixed base as shown in Figure 1-1(c). Confocal microscopes [10, 11] and interferometers such as the Twyman-Green and the Mach-Zehnder are common optical profilometers. Heterodyne and white-light interferometers can yield accuracy as good as a few nanometers in the axial z direction, but their lateral resolution is limited typically to a few micrometers. The recently developed methods of atomic force microscopy (AFM) [12] and scan tunneling microscopy [13] extend profilometry to nanoscale accuracies in all three dimensions.

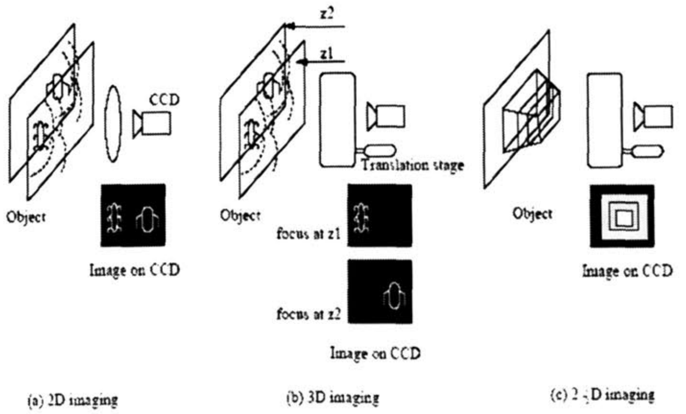

(a) 2D imaging
(b) 3D imaging
(c) $2\frac{1}{2}$D imaging

Figure 1-1: (a) 2D imaging system cannot discriminate the distance between two objects; (b) a 3D imaging system can recover depth by scanning; (c) a $2\frac{1}{2}$D imaging system maps the height of a reflective surface to an intensity on the detector.

Most of the above profilometry systems trade the FoV off the imaging resolution. Therefore, they need scanning or other techniques to recover the complete object height map. In additional to the three spatial dimensions, capturing the spectral information simultaneously is also of interest in various imaging applications. The spectral information can be thought as the fourth dimension of the object. The discussion on multi-dimensional profilometry imaging systems also forms a major content in this thesis.

In this Chapter, we first make a brief introduction of the profilometric measurement with various means, the performance characterization of an optical profilometry system and the multidimensional hyper-spectral profilometry system in Section 1.1. In Section 1.2, we will introduce the Volume Holographic (VH) lens as a 3D optical imaging element, followed by introduction of the outline of this thesis in Section 1.3.

1.1 Fundamentals of optical profilometry and spectral imaging

Highly precise and accurate profile measurement (profilometry) is important in precision engineering such as precise parts manufacturing, optical element grinding and polishing, *etc.* Several techniques have been developed for high-resolution profilometry in different application areas [14, 9, 15, 11, 16, 17]. A profilometer acquires a height map $z(x, y)$ where z denotes the "longitudinal" distance between a reference plane and the object surface at coordinate x, y as shown in Figure 1-2. Often, profilometers make the assumption that the object image brightness $b(x, y)$ is constant to simplify the height acquisition process. When the constant brightness assumption does not hold, an additional regular image can be captured to acquire the brightness information $b(x, y)$, which is then used to normalize the profilometric measurements. Therefore, for the rest of this thesis, the constant brightness of the object is implicitly assumed without specific notation.

In general, profilometry techniques can be categorized as contact and non-contact. Contact methods measure the object profile by scanning a stylus over the entire object surface. Contact scanning may scratch, and thus damage the surfaces of the object.

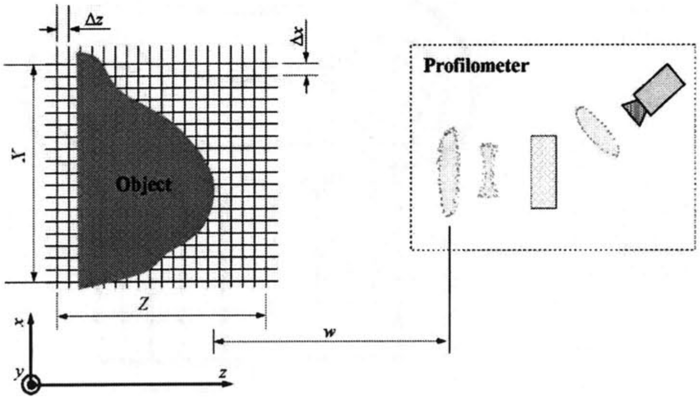

Figure 1-2: Schematic of a non-contact profilometer.

Non-contact methods have the inherent advantage of measuring the object 3D profile without mechanical contact with the object and can be used to measure objects with fragile surfaces. Non-contact methods are also important for objects that (a) can not be touched, *e.g.* inconvenient location and/or too hot/cold *etc.* (b) stealthy interrogation is preferable. Optical probing based techniques such as interferometry [16], stereo imaging [15] and confocal imaging [10, 11] are widely used as non-contact profilometry methods. The performance of a profilometer can be characterized by a number of attributes shown in Figure 1-2.

1. Longitudinal resolution Δz is the minimum height difference that the profilometer can resolve.
2. Lateral resolutions Δx and Δy represent the minimum features that the profilometer can resolve in the x and y directions.
3. Longitudinal range Z is the maximal depth range over which the profilometer can measure.
4. Lateral ranges X and Y are the maximal measurement ranges in lateral directions.
5. Minimal working distance w is the shortest distance by which the front surface of the instrument is allowed to approach the object. The minimal working distance definition applies only to non-contact profilometers.

6. Measuring time T is the sum of the integration time required by the transducer to complete one measurement and by the scanning time required to cover the entire object.

Non-contact profilometry methods may also be divided into two categories according to working distance. Close-up working distance methods can acquire the object profile with very high accuracy. For example, the Scanning Confocal Microscope (SCM) measures the object's profile by rejecting out-of-focus light with a pinhole [10, 11]. Commercial SCMs customarily achieve sub-micron resolution. Dual-wavelength interference profilometers measure the height map by heterodyning two wavelengths, and can achieve even better depth resolution at the level of nanometers [16]. However, these methods usually impose critical measuring requirements, *i.e.*, no vibration, and are not applicable outside laboratories. For field and/or industrial applications, long working distance methods are more convenient but they typically yield poorer depth resolution. Examples are triangulation based stereo vision methods [15].

The most common optical imaging method used to acquire the object spectral information is spectrography. The schematic of a spectrograph is shown in Figure 1-3. The light irradiated or reflected from the object is collected by an objective lens, and then projected to a diffraction grating. The grating then diffracts the incident light to different directions according to the wavelength, because the dispersion relation of the grating is highly wavelength dependent. The diffracted light is then refocused by an imaging lens, forming a rainbow-like spectrum. Therefore, by placing a narrow slit at the back focal plane of the imaging lens, light within a very narrow range of wavelengths is measured by a optical powermeter or CCD camera. The full range measurement can be accomplished by scanning the narrow slit over the entire spectral distribution. There are two different types of spectrograph: simple spectrometer and imaging spectrograph.

1. A simple spectrometer measures only the integrated radiance of the object as a function of wavelength so it does not form image of the object.

2. An imaging spectrograph can form a image of the object like a traditional 2D

imaging system, and in addition it can measure the wavelength distribution irradiated at each pixel.

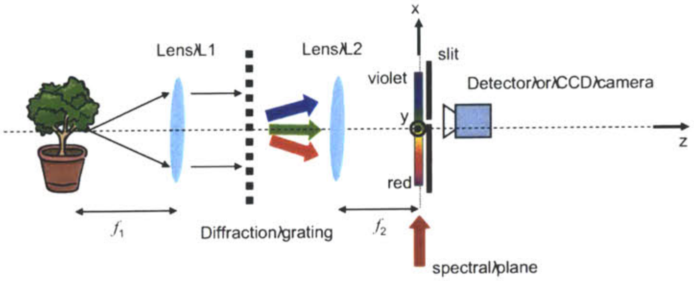

Figure 1-3: Schematic of a spectrograph.

1.2 Imaging using volume holographic lenses

Traditional 2D imaging systems process the incident radiation with a sequence of 2D optical elements. An optical element is referred to as 2D when it interacts with the optical field in a 2D fashion, *i.e.*, through refraction, reflection and diffraction at a sequence of discrete 2D surfaces. For example, an optical lens refracts the incident light at the curved front and back air/glass interfaces. The entity of the lens only acts as spacing medium to separate these two surfaces. 2D optical elements prevail in today's optical imaging instrument design. Their optical properties are well known and a number of computer aided optical design software, such as CODEV$^{\text{TM}}$ and Zemax$^{\text{TM}}$ have been developed to characterize and optimize the performance of optical design using 2D optical elements.

A simplified imaging system using lenses is shown in Figure 1-4. The refractive surfaces of lenses collect rays from each point of the object and then refocus them to the corresponding image points on the image. From the point of view of wave optics, this object/image mapping relation is formulated by the convolution between the 2D object and point spread function (PSF) of the imaging system as [2]

$$g\left(x,y\right)=\iint h\left(x'-x,y'-y\right)U\left(x,y\right)\,\mathrm{d}x\mathrm{d}y. \tag{1.1}$$

For a monochromatic, abberation-free system, the PSF relates to the exit pupil function of the imaging system as

$$h\left(u,v\right)=\mathcal{F}\{P\left(x,y\right)\}_{u=\frac{x'}{\lambda s_2},v=\frac{y'}{\lambda s_2}}, \tag{1.2}$$

where, $\mathcal{F}\left(\cdot\right)$ denotes Fourier transformation, λ is the wavelength of the light and s_2 is the distance from the exit pupil of the imaging system to the image plane.

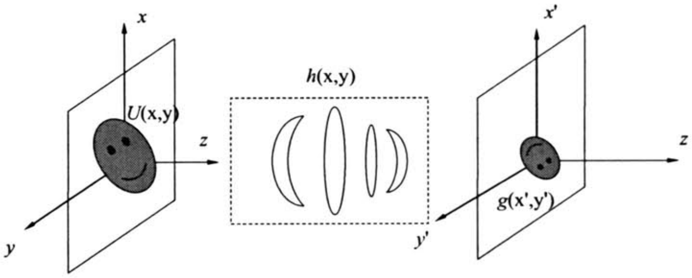

Figure 1-4: Illustration of a imaging system using conventional 2D lenses.

From Eq. (1.1) and (1.2) it can be seen that the impulse response or PSF for conjugate object and image planes of a 2D imaging system is shift-invariant. For a diffraction limited imaging system, the PSF is usually a point-like function in x', y' coordinates [1, 2], resulting in a sharp image analogous to the object over the entire field of view (FoV). For an object not on the corresponding in-focus object plane, the PSF becomes defocus dependent and can be formulated by the well-known *Lommel* function $\mathcal{L}\left(R,\delta\right)$, where $R=\sqrt{x'^2+y'^2}$ and δ is the defocus distance. *Lommel* function expands as δ increases, resulting in an image blur for the defocused objects. This implies that the lens-based 2D imaging system can not discriminate the depth or distance information of the object precisely. The consequence of defocus blur usually deteriorates the image signal to noise ratio (SNR).

The other disadvantages of 2D optical elements are also apparent, such as:

1. The design freedom is limited, because only the few discrete surfaces actually interact with the incident optical field. Therefore, in a complicated design, a large number of optical elements are needed. For example, a telephoto photo-

graphic zoom lens usually consists of 12-16 pieces of singlets to reduce/correct various of abberations;

2. Spacing between the 2D elements is usually necessary for light to propagate from one surface to another, resulting in bulky size and heavy weight of the instruments;

3. Because an optical design usually consists of multiple 2D elements, high precision assembly is critical to the final performance. This incurs high manufacturing costs.

Different from the 2D optical elements, 3D optical elements interact with the incident optical field throughout the entire volume of the element. A restricted class of 3D optical elements have been used in optic design for years. One example is the gradient refractive index (GRIN) lens [18]. A typical GRIN lens has the refractive index decreasing gradually from the central optical axis to the edge of the lens. Therefore, light rays incident at the edge of the GRIN lens are bent towards the center due to this refractive index modulation and then focus at the back focal point.

Another example of 3D optical element is the volume hologram [19]. Volume hologram, as opposite to the thin holograms, refers to the holograms of thickness at least 20-50 times of optical wavelengths. Thin holographic imaging was originally proposed by Gabor [20] to recover both the amplitude and the phase of the light coming from an object with the intent of using the phase to store and reconstruct spatial 3D information about the object. A Gabor or Leith-Upatnieks hologram [20, 21] is a thin hologram. It is recorded by reference beam and the light scattered by the object. Both analog [22] and digital [23, 24] holograms have been used extensively for 3D and $2\frac{1}{2}$D imaging. Figure 1-5(a) is a simplified holographic image recording setup; auxiliary optical elements such as lenses have been omitted. It is possible to recover the amplitude and phase of the light originated from the object and somehow form a 3D reconstruction of the object when we probe the hologram optically with a probe beam. Analog holography requires recording a new fresh hologram for each object and then optically reconstructing them section-by-section. Reconstruction can also be done in digital way, as long as the holographic interference pattern is recorded with a digital imager. Digital holography requires a deconvolution operation for each frame recorded by the camera to accomplish the reconstruction.

Volume holograms were first introduced by van Heerden [19]. Since then, the properties of these "thick" diffractive elements have been studied extensively [25, 26]. Volume holograms have been used in several sub-areas of optical information processing, namely data storage [25, 27, 28, 29], optical interconnects [30], artificial neural networks [31, 32, 33] and communication [34, 35, 36, 37, 38]. Prior to the spectacular improvement of VLSI technology in the 1990's [39, 40], volume holograms were considered as a primary contender for the efficient storage and implementation of the massive interconnections needed for complex pattern recognition tasks.

A volume hologram diffracts in the Bragg regime (as opposed to the Raman-Nath regime of thin holograms [41]). This means that the volume holograms have a single diffraction order, corresponding to the direction in which all the diffracted optical fields from the entire volume of the hologram interfere constructively with each other. This constructive interference results in highly selective angular dependence as well. In general, volume holograms can be recorded with the interference of two mutually coherent light beams, namely, signal beam and reference beam at a photo-sensitive material, or by other means, as long as the same refractive index modulation is achieved.

A VH lens is created by recording the interference pattern of the reference and signal beams, within the entire volume of a thick photosensitive material [41]. It does not involve recording the radiation from any particular object. The VH lens is embedded into the optical imaging instrument as a regular lens. Figure 1-5(c) depicts a VH lens recorded by a point-source reference and plane-wave signal. Holographic lenses that are sufficiently thick [41] are sensitive to the nature of the illumination and diffract only when the input field matches the recording conditions. For arbitrary object illumination, as shown in Figure 1-5(d), the VH lens diffracts only the so called Bragg matched components of the incident field. Thus one can see only a particular section, *i.e.*, the on-focus section, of the entire object on the detector. The advantages of VH lenses compared to traditional volume holography are

1. The VH lens is pre-recorded and not object dependent. Therefore, there is no need to erase and record new volume holograms when imaging different objects.
2. The imaging process of the VH lens does not involve interference of light, which is very sensitive to vibration in working environments, as in traditional holography. So, generally, there is no special care or maintenance necessary when using the VH lens compared to regular optical lenses and gratings.

The use of volume holograms as imaging optical elements, referred to as VH lenses in this thesis, was first proposed by G. Barbastathis, M. Balberg, and D. J. Brady [42]. It has been demostrated in the context of a confocal microscope with a VH lens replacing the pinhole [42], a VH lens as a long range surface profilometer [43, 44], a real-time (scan-free) hyperspectral imaging instrument [45], VH lens based imaging spectrometer [44] *etc.* An important property of VH lenses in imaging is the phenomenon of Bragg selectivity. To understand Bragg selectivity, suppose that a VH lens is recorded with a certain reference beam and a signal beam (see Figure 1-6 (a)). After recording is complete, the VH lens is probed with a third beam. Depending

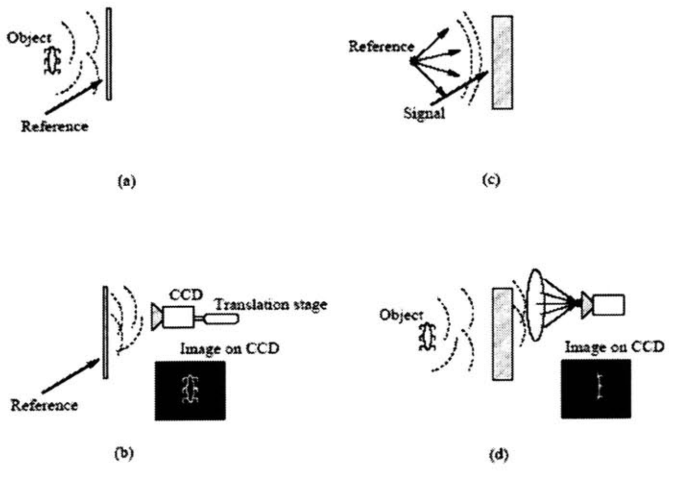

Figure 1-5: Simplified schematics of VH lens recording and read out: (a) recording, (b) Bragg matched readout, (c) Bragg mismatched readout and (d) Bragg degenerate readout.

on the relationship between the probe beam and the reference beam, we can obtain three types of diffraction:

1. Bragg matched, where the probe beam is the exact replica of the reference beam, as shown in Figure 1-6(b). In this case, the full diffraction efficiency of the recorded hologram is recovered.

2. Bragg mismatched, where the probe beam wave front differs from the reference beam wave front. For example, the probe beam could have a different angle of incidence or wavelength [25, 46]. For a Bragg-mismatched probe, which is not degenerate (see below), the hologram does not diffract at all or at least the diffraction efficiency obtained from the hologram is much weaker than the Bragg-matched case. This is shown in Figure 1-6(c).

3. Bragg degenerate diffraction is obtained for a special class of probe beams that differ from the reference beam yet still give rise to strong diffraction of a magnitude comparable to the Bragg-matched case. For VHs recorded with a plane wave reference, degenerate diffraction can be obtained by either a combined change in wavelength and angle of a plane-wave probe, as shown in Figure 1-6(d) [47, 48], or by tilting the probe beam in a direction parallel to the fringes that constitute the VH lens [25, 41]. Generally, degenerate diffraction occurs if the probe beam can be obtained from the reference beam by a transformation that is invariant with respect to the orientation of the interference pattern that constitutes the hologram.

Because of the different responses to Bragg matched, mismatched and degenerated probe sources, the PSF or impulse response of a VH lens is shift variant. This property is usually undesirable in conventional optics design, since shift variant response usually complicates the imaging process. However, by incorporating scanning or multiplexing and suitable digital post-processing algorithms, this shift invariance can be exploited to extract object information which could not be acquired with a 2D optical imaging system, e.g, the depth (shape) information, the spectral information, *etc.*

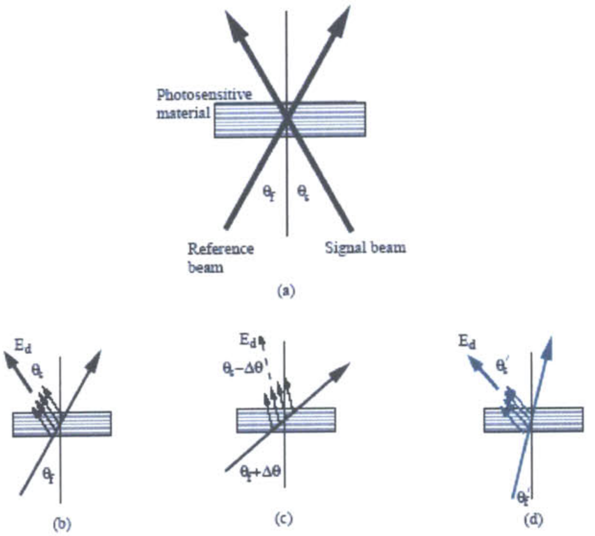

Figure 1-6: Simplified schematics of traditional holography: (a) recording and (b) readout by scanning. Schematics of VH lens imaging: (c) making VH lens and (d) readout.

1.3 Outline of this thesis

We start by developing the theoretical framework for VH lens based imaging systems in Chapter 2, based on the three dimensional diffraction formulation. Then we analyze a laser profilometry system with a VH lens recorded by a planar reference beam. The following procedure is adopted: First, we derive the diffraction formulation for Bragg matched, mismatched, and degenerated probe, then we calculate the profilometry resolution of the setup and discuss optical design methods that optimize resolution, working distance, *etc.* Finally, we present experimental verification of the theory and the optimized designs.

In Chapter 3, we propose digital post-processing algorithms based on maximum likelihood (ML) estimation by adopting the Viterbi algorithm (VA). The digital post-processing model is built based upon the VH imaging channel analysis. Post-processing is used to: (a) Clean up the raw profilometic images and improve depth resolution; (b) interpolate detail features of the objects between the directly imaged depth layers to reduce the amount of required depth scanning. Digital post-processing framework is built for both coherent and incoherent illumination cases. Experimental implementations are shown to demonstrate that the post-processing algorithms are effective.

Real-time non-scanning VH profilomety system using rainbow illumination is then presented in Chapter 4. The goal is to expand system FoV to reduce or eliminate lateral scanning. The same analysis procedure as used in Chapter 2 is adopted: theoretical framework followed by experimental validation. A multi-dimensional hyper-spectral profilometry imaging system is then introduced based on the rainbow VH imaging design. Experiments show that the hyper-spectral system extracts both the 3D spatial and the spectral information of the object with very high resolution.

We conclude in Chapter 5 by summarizing the major benefits and drawbacks of using VH lenses for depth selective profilometric imaging. We propose some promising directions for future work in this area.

Chapter 2

Volume holographic lens and profilometry with laser scanning volume holographic imaging system

In this chapter, we present the theory of diffraction from VH lenses and then describe a monochromatic laser illumination profilometry system that uses VH lenses. A VH lens is manufactured by recording the three-dimensional interference pattern of two (or more) mutually coherent beams as shown in Figure 2-1(a). After recording, the VH lens is fixed and can be used in optical systems the same way as refractive lenses, mirrors, *etc.* Despite the apparent simplicity of the recording, VH lenses offer unique imaging capabilities that are not available from traditional lenses. Assume a simple VH lens is recorded with the interference of two planar waves. In imaging, the VH lens is used as shown in Figure 2-1(b). Because of the angular Bragg selectivity of the VH lens, light originating off the y-axis points in the in-focus $x-y$ plane is rejected. The rejection ratio relating the diffracted intensity to the deviation angle from the y axis is a $sinc^2$ function. Along the y axis, there is no selectivity due to the degeneracy of the VH [17]. Thus, the VH defines a "visible slit", oriented along the y-dimension in the object plane. Now consider the defocused point sources; for example, point source $A(x{=}0,\ y{=}0,\ z=-\delta)$ as shown in Figure 2-2. According to the Huygens principle, point source A is equivalent to an extended source B at the in-focus $x-y$ plane, as long as the power conservation and phase delay due the propagating are taken into account. The size of B can be approximated according to geometrical optics as the intersection between the light cone, subtended by point source A and objective lens L_1, and the $x - y$ plane, as shown in Figure 2-2. However, as we mentioned before, a large portion of the extended source B is rejected by the volume hologram. This means that the out-of-focus but on-axis point source A is partially obstructed by the VHI system. For point sources that are both out-of-focus and off-axis, the rejection is contributed by both the depth and the angular shift. Therefore, it is clear that the use of VH lens improves longitudinal or depth discrimination. Here we refer to the depth selectivity in a simplified fashion, neglecting portions of the object that are outside of the "visible slit." A rigorous derivation of the depth and angular selectivity of the VHI is given in [17] and later in this Chapter. By scanning along the x and z axes, the object is optically sliced layer by layer [17]. Images of every layer are captured by a digital camera and then sent to computer for post-processing and reconstruction. Finally, a high quality 3D digital model of the object is obtained based on the intermediate "raw" images.

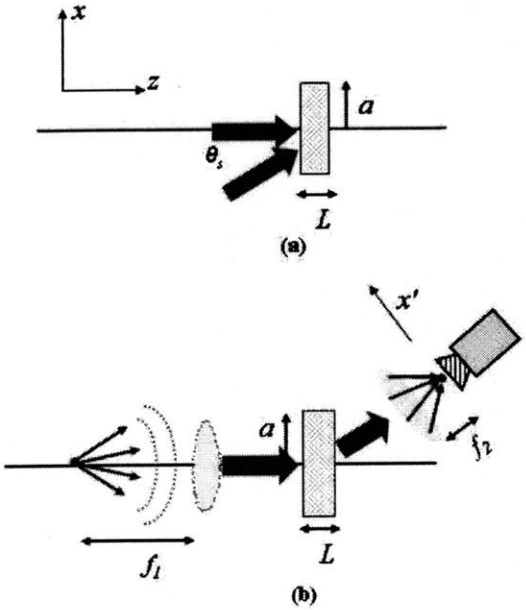

Figure 2-1: Rcording (a) and readout (b) schematics of a VHI setup.

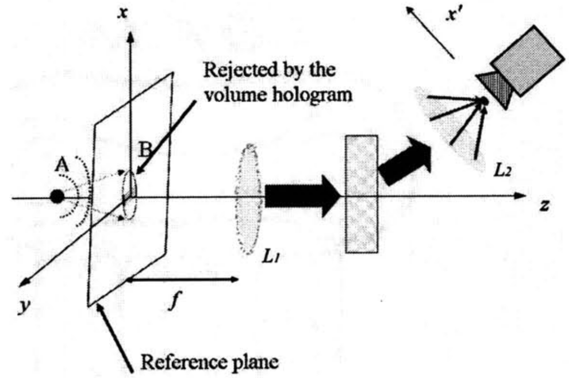

Figure 2-2: Illustration for depth selectivity of a VHI setup.

2.1 3D diffraction framework of volume holographic lenses

Figure 2-3 shows the schematic used to analyze the diffraction properties of VH lenses. It consists of a $4F$ system formed by two ideal (abberation free) thin lenses L_1 and L_2 of focal lengths f_1 and f_2, respectively. The object is placed in the vicinity of the front focal plane of L_1, and the optical radiation originated from the object is assumed to be monochromatic and spatially coherent with wavelength λ and amplitude $p\,(x, y)$. Our goal is to derive diffracted field distribution $q\,(x', y')$ at the back focal plane of L_2.

If a thin transparency (amplitude or phase mask) is placed at the confocal plane of L_1 and L_2, the answer of $q\,(x', y')$ is well known [2]. Lens L_1 forms the Fourier transform $P\,(x'', y'')$ at the confocal plane. This Fourier transformed light distribution is then filtered by the think transparency and then another Fourier transform is performed by the second lens L_2. The output image is formed at the back focal plane of L_2. The difference in this case from the well-know $4F$ system is that the transparency function of VH lens $\epsilon\,(x, y, z)$ is 3D. Therefore, 3D filtering at the Fourier domain occurs at the Fourier plane as opposed to 2D filtering in conventional $4F$ systems. As result, more degrees of freedom in determining the filter characteristic are obtained.

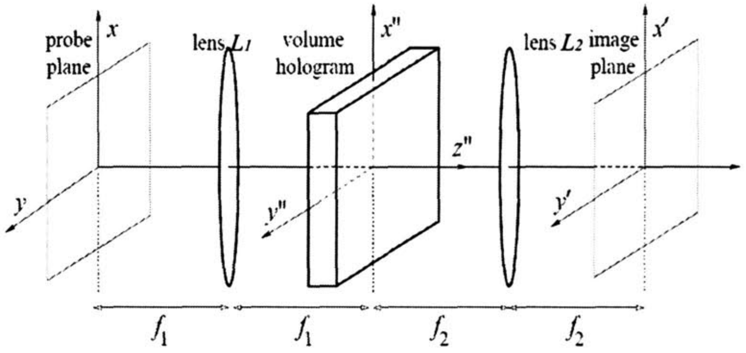

Figure 2-3: Geometry of the $4F$ optical system with volume holographic aperture filter.

Consider the field generated from the propagation of $p(x, y)$ through L_1 to the vicinity of the confocal plane. It is given by Fresnel integral and quadratic phase moadulation of the lens, as [1, 2]

$$P(x'', y'', z'') = \exp\left\{i2\pi\frac{z''}{\lambda}\right\} \iint p(x, y) \exp\left\{-i2\pi\frac{xx'' + yy''}{\lambda f_1}\right\} \cdot \exp\left\{-i\pi\frac{(x^2 + y^2) z''}{\lambda f_1^2}\right\} \mathrm{d}x\mathrm{d}y. \quad (2.1)$$

Here and in the rest of this thesis we will be neglecting amplitude terms of the form $1/i\lambda z$ in Fresnel integral. Because the depth selectivity is the measurement of the ratio of Bragg-matched and mismatched diffraction, this constant factor does not contribute to it.

After passing through the VH lens, the optical field is filtered by the 3D pupil as

$$g(x'', y'', z'') = P(x'', y'', z'') \cdot \epsilon(x'', y'', z'') \quad (2.2)$$

Lens L_2 performs the second Fourier transform with respect to the probing field $g(x'', y'', z'')$ at the vicinity of its focal plane. Therefore, the optical field distribution at the back focal plane is the 3D Fourier transform of $g(x'', y'', z'')$, evaluated at a parabolic 2D manifold, as

$$q(x',y') = \sqrt{\eta} G\left[\frac{x'}{\lambda f_2}, \frac{y'}{\lambda f_2}, \frac{1}{\lambda}\left(1 - \frac{x'^2 + y'^2}{2f_2^2}\right)\right] \tag{2.3}$$

From Eq. 2.3, it can been seen the three dimensional Fourier transform is evaluated at the parabolic plane given by that $\left[\frac{x'}{\lambda f_2}, \frac{y'}{\lambda f_2}, \frac{1}{\lambda}\left(1 - \frac{x'^2+y'^2}{2f_2^2}\right)\right]$. when the object is a point source at (x_o, y_o). By substituting $p(x,y) = \delta(x - x_o, y - y_o)$ into Eq.(2.1), Eq.(2.2) and Eq.(2.3), the shift variant impulse response or PSF is obtained as

$$\begin{aligned} h(x',y';x_o,y_o) = \mathcal{E}\left[\frac{1}{\lambda}\left(\frac{x_o}{f_1} + \frac{x'}{f_2}\right), \frac{1}{\lambda}\left(\frac{y_o}{f_1} + \frac{y'}{f_2}\right),\right. \\ \left.\frac{1}{\lambda}\left(\frac{x_o^2 + y_o^2}{2f_1^2} + \frac{x'^2 + y'^2}{2f_2^2}\right)\right], \end{aligned} \tag{2.4}$$

where $\mathcal{E}(u,v,w)$ denotes the 3D Fourier transform of the dielectric modulation $\epsilon(x,y,z)$. Therefore, the system input-output relation can be written as

$$q(x',y') = \iint p(x,y)\, h(x',y';x,y)\, \mathrm{d}x\mathrm{d}y. \tag{2.5}$$

2.1.1 Bragg-matched response of a volume holographic lens

In this section, we investigate Bragg-matched diffraction property of the VH lens quantitatively. As mentioned before, the Bragg-matched probe should be identical to the phase conjugate of the reference which was used to record the VH lens. Assume that the VH lens is recorded with two planar waves incident onto the recording crystal. These two plane waves can be thought of as originating from two point sources on the front focal plane of L_1, *i.e.*, $\delta(x_f, y_f)$ and $\delta(x_s, y_s)$. In the vicinity of the Fourier plane, the field distributions are:

$$\begin{aligned} P_f(x'',y'',z'') = \iint \delta(x_f,y_f) \exp\left\{-i2\pi\frac{xx''+yy''}{\lambda f_1}\right\} \\ \cdot \exp\left\{-i\pi\frac{(x^2+y^2)z''}{\lambda f_1^2}\right\} \mathrm{d}x\mathrm{d}y, \end{aligned} \tag{2.6}$$

$$Q_s(x'',y'',z'') = \iint \delta(x_s,y_s)\exp\left\{-i2\pi\frac{xx''+yy''}{\lambda f_1}\right\} \cdot \exp\left\{-i\pi\frac{(x^2+y^2)\,z''}{\lambda f_1^2}\right\} \mathrm{d}x\mathrm{d}y, \quad (2.7)$$

After exposure, the refractive index of the holographic crystal is modulated according to the intensity of the interference between P_f and Q_s as

$$|P_f+Q_s|^2 = |P_f|^2 + |Q_s|^2 + P_f^* Q_s + P_f Q_s^*. \quad (2.8)$$

When probed by the Bragg-matched beam, *i.e.*, $p(x,y) = p_f(x,y)$, the reconstructed field filtered by the VH lens is

$$P_f \cdot |P_f+Q_s|^2 = \left(|P_f|^2 + |Q_s|^2\right) P_f + |P_f|^2 Q_s + P_f Q_s^* P_f. \quad (2.9)$$

Only the third term contributes to the diffracted field, so we neglect the other three terms from now on. The VH lens is then represented by

$$\epsilon(x'',y'',z'') = P_f^*(x'',y'',z'')\,Q_s(x'',y'',z'')\,s(x'',y'',z''), \quad (2.10)$$

where $s(x'',y'',z'')$ is the function that defines the geometry of the VH lens as

$$s(x'',y'',z'') = \begin{cases} 1 & \text{if } (x'',y'',z'') \text{ is inside the VH lens, and} \\ 0 & \text{otherwise.} \end{cases} \quad (2.11)$$

By substituting Eq.(2.10) into Eq.(2.3) and carrying out the integral, we find

$$q(x',y') = \frac{1}{V}\iint q_s(x,y) \cdot S\left[\frac{1}{\lambda}\left(\frac{x}{f_1}+\frac{x'}{f_2}\right), \frac{1}{\lambda}\left(\frac{y}{f_1}+\frac{y'}{f_2}\right), \frac{1}{\lambda}\left(\frac{x^2+y^2}{2f_1^2}+\frac{x'^2+y'^2}{2f_2^2}\right)\right], \quad (2.12)$$

where the normalization factor V is the VH lens volume

$$V = \iiint s(x'',y'',z'')\,\mathrm{d}x''\mathrm{d}y''\mathrm{d}z''. \quad (2.13)$$

2.1.2 Angular selectivity of a volume holographic lens

We now consider a VH lens recorded by two planar waves originated from $p_s\left(x_s, 0\right)$ and $q_f\left(0,0\right)$, then from Eq.(2.7), Eq.(2.6) and Eq.(2.10), we find

$$\epsilon\left(x'', y'', z''\right) = \exp\left\{i\frac{2\pi}{\lambda}\left(\frac{-x''x_s}{f_1} + z''\frac{-x_s^2}{2f_1^2}\right)\right\} s\left(x'', y'', z''\right). \tag{2.14}$$

Suppose we probe the VH lens with a point source at the position (x, y). Substituting into Eq.(2.2) and Eq.(2.3), we obtain

$$q\left(x', y'\right) = \sqrt{\eta} S\left[\frac{x' + m\left(x_s + x\right)}{\lambda f_2}, \frac{y' + my}{\lambda f_2}, \frac{m^2\left(x_s^2 + x^2\right) - x'^2}{2f_2^2}\right], \tag{2.15}$$

where

$$m = \frac{f_2}{f_1} \tag{2.16}$$

is the lateral magnification ratio of the $4F$ system. For simplicity, we assume that the VH lens is a slab with infinite lateral size and thickness L, then

$$s\left(x'', y'', z''\right) = \operatorname{rect}\left(\frac{z''}{L}\right). \tag{2.17}$$

Substituting into Eq.(2.15), we find

$$q\left(x', y'\right) = \sqrt{\eta}\operatorname{sinc}\left(L\frac{m^2\left(x_s^2 + x^2\right) - x'^2}{2f_2^2}\right)\delta\left(x' + m\left(x_s + x\right)\right)\delta\left(y' + my\right). \tag{2.18}$$

From Eq.(2.18), it can be obtained that the diffracted image corresponding to the probe source is at $\left(-m\left(x_s + x\right), -my\right)$. Substituting it into Eq.(2.18) and the intensity of the point is

$$I\left(-m\left(x_s + x\right), -my\right) \propto \eta\operatorname{sinc}^2\left(L\frac{-m^2 x_s x}{f_2^2}\right). \tag{2.19}$$

It can be clearly seen from Eq.(2.24) that the VH lens is Bragg-matched only when the term inside the *sinc* function is zero, *i.e.*, $x = 0$. Physically it means the probe source is at the identical position of the reference source (in our derivation $x = x_f =$

0). When the probe source is displaced, the VH lens is Bragg-mismatched and the diffracted intensity drops as a $sinc^2$ function of the offset x.

One can also find from Eq.(2.18) that the diffraction is independent on the probe's vertical position y. This means that when the probe source is shifted along the y axis, the diffraction field remains the same. This property is named *shift degeneracy* of VH lens. It can be physically understood as the VH lens is recorded by two planar waves in the $x - z$ plane, the interference fringes are then vertically aligned, parallel to the y axis. Therefore, by shifting the probe source vertically, the refractive index modulation remains invariant with respected to the probe wave, and the diffraction efficiency remains high.

2.1.3 Wavelength degeneracy of a volume holographic lens

Now consider the same VH lens, but probed with point source (x, y) of wavelength λ_p rather than the recording wave length λ. Following the same derivation in Section 2.1.2, we can find

$$q(x', y') = \sqrt{\eta} S \left[\frac{x' + m(\mu x_s + x)}{\lambda f_2}, \frac{y' + my}{\lambda f_2}, \frac{m^2 (\mu x_s^2 + x^2) - x'^2}{2 f_2^2} \right]. \tag{2.20}$$

where

$$\mu = \frac{\lambda_p}{\lambda} \tag{2.21}$$

is the wavelength ratio. Therefore, the field diffracted from a slab shaped VH lens is

$$q(x', y') = \sqrt{\eta} \operatorname{sinc} \left(L \frac{m^2 (\mu x_s^2 + x^2) - x'^2}{2 f_2^2} \right) \delta(x' + m(\mu x_s + x)) \delta(y' + my). \tag{2.22}$$

The image point is located at

$$x' = -m(\mu x_s + x), y' = -my. \tag{2.23}$$

Substituting into Eq.(2.22), the intensity of the diffracted image is

$$I\left(-m\left(x_s+x\right),-my\right)\propto\eta\mathrm{sinc}^2\left(L\frac{m^2\mu x_s\left[\left(1-\mu\right)x_s-2x\right]}{f_2^2}\right). \tag{2.24}$$

Then the Bragg match condition is

$$m^2\mu x_s\left[\left(1-\mu\right)x_s-2x\right]=0. \tag{2.25}$$

It can be seen from Eq.(2.25) that even if the probe source is shifted away the position of the reference source $(0,0)$, it is still possible to make it Bragg-match the VH lens by tuning its wavelength to

$$\lambda_p=\left(1-\frac{2x}{x_s}\right)\lambda \tag{2.26}$$

This shift-variant imaging property of the VH lens is known as *wavelength degeneracy.* It has been used for non-destructive readout of holograms at wavelengths where the material sensitivity to photoexposure is very small. It also serves as the basis of using rainbow illumination to parallelize the VH imaging across a large FoV, as we will see in Section 4.

2.2 Monochromatic laser scanning profilometry using a volume holographic lens

2.2.1 Derivation and properties of the diffracted field

Figure 2-4(a) is the recording setup for VHI with the VH lens recorded by planar reference waves. The collimating objective lens ensures that the reference beam is approximately a plane wave when it is incident on the hologram. Thus the front focal length of the objective lens is the reference depth at which the VHI system operates.

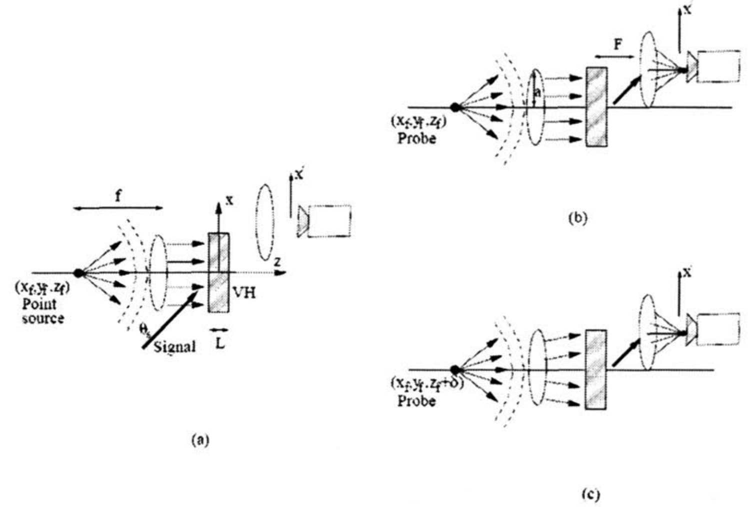

Figure 2-4: Plane wave reference VHI schematic, (a) Recording; (b) Bragg matched readout and (c) Bragg mismatched readout.

During recording, the reference beam is a normally incident plane wave:

$$E_f\left(\mathbf{r}\right) = \exp\left(i2\pi \frac{z}{\lambda}\right). \tag{2.27}$$

The hologram and the Fourier transform (FT) lens are assumed to have infinite lateral extent. L is the thickness of the hologram, f is the focal length of the collimating objective lens, and a is its radius. Thus, the numerical aperture (NA) of the entire imaging system equals a/f. The focal length of the FT lens is F. The signal beam is a plane wave propagating at a small angle θ_s with respect to the z axis. In the paraxial approximation, the signal beam is expressed as

$$E_s\left(\mathbf{r}\right) = \exp\left[i2\pi\left(1-\frac{\theta_s^2}{2}\right)\frac{z}{\lambda} + i2\pi\theta_s\frac{x}{\lambda}\right]. \tag{2.28}$$

Then, the Bragg-matched term of the VH lens refractive index modulation is given by

$$\epsilon\left(\mathbf{r}\right) = \exp\left[\frac{i2\pi}{\lambda}\left(x\theta_s - z\frac{\theta_s^2}{2}\right)\right]. \tag{2.29}$$

Figures 2-4(b) and (c) show the readout procedure. A probe point source is placed in front of the objective lens at coordinates $\mathbf{r}_p = (x_p, y_p, z_p)$. We now derive the dependence of the diffracted power on the displacement δ of the probe source from the reference plane. To do this, it is mathematically convenient to express the defocused spherical probe as well as the diffracted field in terms of their plane-wave components with wave vectors $\mathbf{k}_p$ and $\mathbf{k}_d$, respectively. The transfer function [41]

$$\tilde{A}\left(\mathbf{k}_p, \mathbf{k}_d\right) = S \int_{v} \epsilon\left(\mathbf{r}\right) \exp\left[i\left(\mathbf{k}_p - \mathbf{k}_d\right) \cdot \mathbf{r}\right] \mathrm{d}^3\mathbf{r} \tag{2.30}$$

specifies the spatial spectrum of the hologram response to a single spatial frequency in the input field. In Eq.(2.30) , S is a constant determined by the polarization and index modulation; our analysis will normalize the diffracted intensities, and so this factor can be neglected. $\tilde{A}\left(\mathbf{k}_p, \mathbf{k}_d\right)$ can be interpreted as the 3D Fourier transform of the dielectric constant modulation $\epsilon\left(\mathbf{r}\right)$ evaluated at $\mathbf{k}_p - \mathbf{k}_d$. In the more general case, in which the spatial spectrum of the probe field is given by $\tilde{E}_p\left(\mathbf{k}_p\right)$, the spatial spectrum of the diffracted field is obtained from Eq.(2.30) as

$$\tilde{E}_d\left(\mathbf{k}_d\right) = \iint \tilde{E}_p\left(\mathbf{k}_p\right) \tilde{A}\left(\mathbf{k}_p, \mathbf{k}_d\right) \mathrm{d}k_{px}\mathrm{d}k_{py}, \tag{2.31}$$

where k_{px} and k_{py} are the $\hat{\mathbf{x}}$ and $\hat{\mathbf{y}}$ components of the probe wave vector, respectively, whereas the $\hat{\mathbf{z}}$ component is given by the Bragg constraint $|\mathbf{k}_p| = 2\pi/\lambda$. Because the detector is located at the Fourier transform plane of the FT lens, the diffracted field as a function of the detector plane coordinates (x', y') is obtained from Eq.(2.31) when we substitute $k_{dx} = 2\pi x'/\lambda F$, $k_{dy} = 2\pi y'/\lambda F$ for the $\hat{\mathbf{x}}$ and $\hat{\mathbf{y}}$ components of the wave vector $\mathbf{k}_d$, respectively.

In the specific case of interest, where the probe is a spherical wave, we express its spatial spectrum using Weyls identity:

$$\tilde{E}_p\left(k_{px}, k_{py}\right) = \exp\left[\frac{iz_p'\left(k_{px} + k_{py}\right)^2}{2\left|\mathbf{k}\right|}\right], \tag{2.32}$$

where z'_p is the position of the virtual point point and can be calculated with the lens imaging equation as $z'_p = f^2/\delta$. We evaluate integral Eq.(2.30) using Eq.(2.29) and then substitute the result of the integral and Eq.(2.32) into Eq.(2.31). We find that the diffracted field on the detector plane

$$\tilde{E}_d\left(x', y'\right) = \exp\left\{-i\pi\frac{z'_p}{\lambda}\left[\left(\frac{x'}{F} - \theta_s\right)^2 + \left(\frac{y'}{F}\right)^2\right]\right\}\operatorname{sinc}\left[\frac{L\sin\theta_s}{\lambda}\left(\frac{x'}{F} - \theta_s\right)\right]. \tag{2.33}$$

is almost zero outside a disk of radius $Fa\delta/f^2$ centered at $(x' = \theta_s F, y' = 0)$. This disk represents the geometric image of the aperture of the objective lens on the detector plane. Therefore the normalized intensity is expressed approximately as

$$\frac{I\left(x', y'\right)}{I_b} = \operatorname{circ}\left[\frac{\sqrt{\left(x' - \theta_s F\right)^2 + y'^2}}{Fa\delta/f^2}\right]\operatorname{sinc}^2\left[\frac{L\sin\theta_s}{\lambda}\left(\frac{x'}{F} - \theta_s\right)\right], \tag{2.34}$$

where $I_b = I(x' = \theta_s F, y' = 0)$ is the peak intensity produced by the probe. The approximation neglects diffraction ripples at the disk edges; these ripples have negligible effect in practice. The diffraction pattern contains two contributions, shown in Figure 2-5:

1. a disk, represented by the *circ*$(\cdot)$ function, whose radius is proportional to the defocus δ;

2. a slit oriented along the $\hat{\mathbf{y}}$ direction, represented by the *sinc*$^2(\cdot)$ function, whose width is inversely proportional to the hologram thickness L. This term rejects out-of-focus light because of the Bragg mismatch.

We want to emphasize here that Eq.(2.34) agrees with the derivation through section 2.1 if the VH lens geometry function Eq.(2.17) includes the imaging system aperture, *i.e.*,

$$s\left(x'', y'', z''\right) = \operatorname{circ}\left(\frac{\sqrt{x''^2, y''^2}}{a}\right)\operatorname{rect}\left(\frac{z''}{L}\right). \tag{2.35}$$

In this case the diffraction field will be in the form of a *Lommel* function, which denotes the rigorous defocused lens response [1].

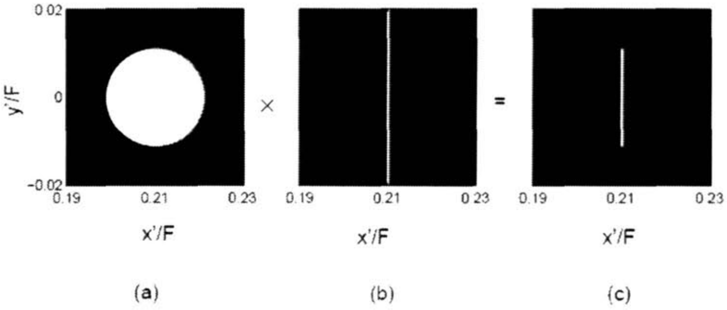

Figure 2-5: Intensity pattern observed on the detector for VHI with (NA)= 0.07, $\theta_s = 12^o$ and $\delta = 8\text{mm}$. (a) Diffraction pattern caused by axial defocus and the finite aperture of collimating lens, (b) Straight Bragg slit of PR hologram, (c) Diffracted pattern observed on the detector.

2.2.2 Depth resolution

To measure the depth resolution of the VHI, we use the metric of longitudinal PSF. The physical meaning of longitudinal PSF is the integrated diffraction intensity at the image plane while the probe point source is shifted off the reference plane. It is well known that in a conventional imaging system, such as telescope or microscope, the longitudinal PSF is a flat line independent on defocus. due to energy conservation. The calculation proceeds as follows. First we integrate the diffracted intensity of Eq.(2.34) with respect to the detector coordinates (x', y'). To accomplish this step, we change the Cartesian coordinates to polar coordinates. Then we normalize to the peak Bragg-matched integral power I_0. The result is

$$\frac{I_d}{I_0}(\delta) = \frac{1}{\pi}\int_0^{2\pi}\int_0^1 \rho \text{sinc}^2\left(\frac{aL\sin\theta_s\delta}{\lambda f^2}\rho\sin\phi\right) \mathrm{d}\rho \mathrm{d}\phi. \tag{2.36}$$

So far, all the derivations are performed with angles, distances, and a wavelength of light measured inside the holographic material of refractive index n. The corrected longitudinal PSF for quantities measured in air is

$$\frac{I_d}{I_0}(\delta) = \frac{1}{\pi}\int_0^{2\pi}\int_0^1 \rho \mathrm{sinc}^2\left(\frac{aL\sin\theta_s\delta}{n\lambda f^2}\rho\sin\phi\right) \mathrm{d}\rho\mathrm{d}\phi. \tag{2.37}$$

Figure 2-6 shows theoretical and experimental plots of the longitudinal PSF as a function of defocus δ for a NA approximating 0.07, $a = 3.5\text{mm}$, $f = 50.2\text{mm}$, and $\theta_s = 30^o$ outside the hologram. In both the experiment and the simulation, the hologram was recorded in a 2mm thick Fe-doped LiNbO_3 crystal ($n \approx 2.2$). Both the experimental and the theoretical curves yield a $\Delta z_{FWHM} \approx 1.7\text{mm}$.

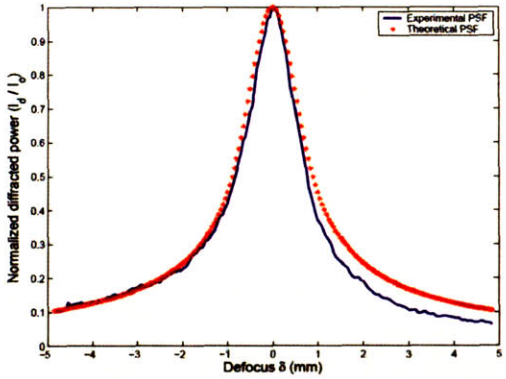

Figure 2-6: Longitudinal PSF for PR VHI.

The trend of longitudinal resolution Δz_{FWHM} versus working distance d is computed directly from the longitudinal PSF expression. In this case, we select the focal length of the objective lens such that $f = d$, and from the scaling factors in the argument of the integrand in Eq.(2.37) we find

$$\Delta z_{FWHM} = \frac{G\lambda d^2}{aL}, \tag{2.38}$$

where G is a factor that depends linearly on θ_s. Numerical regression on Eq.(2.37) yields

$$G = \frac{5.34}{\theta_s}. \tag{2.39}$$

2.2.3 Analysis of the objective optics

We now discuss whether it is possible to improve depth resolution by appropriate choice of objective optics. From Eq.(2.38) we observe that the Δz_{FWHM} of the VHI system varies quadratically with f but only inverse linearly with a. Consider the objective optical system shown in Figure 2-7. The first and second principal planes of this system are denoted as PP_1 and PP_2, respectively. The working distance d is measured between the object and the entrance pupil of the objective optics. The radius of the entrance pupil is a. The effective NA of the optical system is

$$NA_{obj} = \frac{a}{d}. \tag{2.40}$$

The purpose of the objective optics is to illuminate the hologram with a collimated beam when the object is in focus, *i.e.*, located exactly at d. Therefore, the front focal length (FFL) must be equal to d. Let (EFL) denote the effective focal length of the objective optics and r the radius of the collimated beam. In the simplest case, the objective optics consist of a single thin positive lens, as described above. Then EFL=FFL=f=d and r=a.

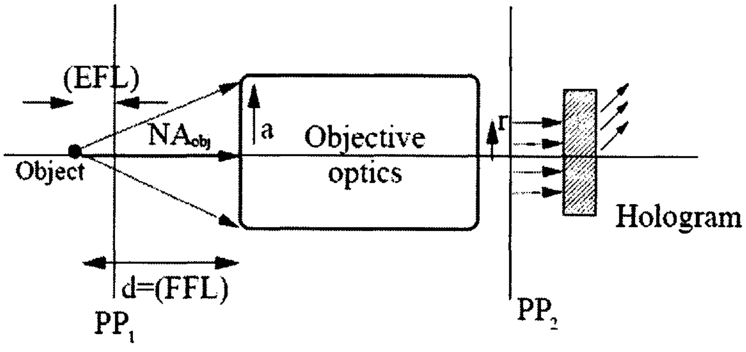

Figure 2-7: Schematic for design of an objective optical system to obtain high depth resolution at large working distances in VHI systems.

For an out-of-focus object, Eq.(2.38) can be rewritten in terms of NA and a as

$$\Delta z_{FWHM} = \frac{G\lambda a}{(NA)^2 L} \tag{2.41}$$

From Figure 2-7, we can see that $r = (NA) \cdot EFL$, which on substitution in Eq.(2.41) yields

$$\Delta z_{FWHM} = \frac{G\lambda r d^2}{a^2 L}. \tag{2.42}$$

This indicates that the quadratic degradation of Δz_{FWHM} with increasing d can be compensated with the physical size r of the collimated beam illuminating the hologram reduced. Equivalently, this is accomplished when the objective optics is designed so that PP_1 is as close to the probe as possible. An example of a standard optical system with this property is a telephoto lens, which is analyzed in detail in the next subsection.

One side effect of making r arbitrarily small is that the ray bundle exiting the objective optics would cease to behave like a plane wave. To make sure that this does not happen, we need to place a lower bound r_{min} on r. A reasonable method to calculate the lower bound is to ensure that the spread of the ray bundle due to diffraction beyond the exit pupil and throughout the length L of the hologram remains a small fraction of r itself. This leads to a condition of the form [2]

$$r_{min} = c\sqrt{\lambda L}, \tag{2.43}$$

where c is selected depending on the amount of diffraction that we are willing to tolerate. For example, in the midvisible range of wavelengths and for L = 2mm, r_{min} = 100mm ensures less than 5% diffraction.

Replacing Eq.(2.43) in Eq.(2.42) we find that the best achievable depth resolution Δz_{FWHM} for VHI varies as

$$\Delta z_{FWHMopt} = \frac{G\lambda r_{min} d^2}{a^2 L}. \tag{2.44}$$

Therefore, the resolution of the optimized VHI system still degrades quadratically with working distance d, but the objective optics provide a favorable (reduced) constant of proportionality by a factor r_{min}/a, compared with the value without objective optics.

It is also possible to design objective optics for VHI such that the resolution degrades with d at a rate slower than quadratic, *e.g.*, linear or even constant. This is accomplished when we use zoom optics in the objective to vary r as a function of d. For example, if we maintain $r \propto 1/d$ then we obtain $\Delta z_{FWHM} \sim d$. However, because of the constraint on the minimum allowable r, the subquadratic behavior is possible only if we are willing to tolerate $\Delta z_{FWHM} > \Delta z_{FWHM_{opt}}$.

To conclude, the objective optics move the effective focal distance much closer to the object than the actual working distance d. Therefore, resolution is improved by as much as r_{min}/a, where a is the physical aperture of the objective optics and r_{min}, the minimum allowable collimated beam diameter. Next we quantify these differences for the specific case of a VHI system implemented with a telephoto lens.

2.2.4 Design of telephoto objective optics for planar reference volume holographic imaging systems

To analyze objective optical systems, we consider a system similar to the one depicted in Figure 2-8 and use the generalized ray-tracing matrix representation [18]:

$$\mathbf{M} = \begin{bmatrix} M_{11} & M_{12} \\ M_{21} & M_{22} \end{bmatrix}. \tag{2.45}$$

The key parameters to determine the resolution and working distance are then given by

$$M_{12} = -\frac{1}{EFL}, \tag{2.46}$$

$$M_{11} = \frac{FFL}{EFL}. \tag{2.47}$$

A telephoto system comprises two lenses of focal lengths f_1, and f_2, with $f_2 < 0$. The lenses are separated by distance t. For the matrix elements M_{11} and M_{12} specified by Eqs.(2.46) and (2.47), the focal lengths are selected as

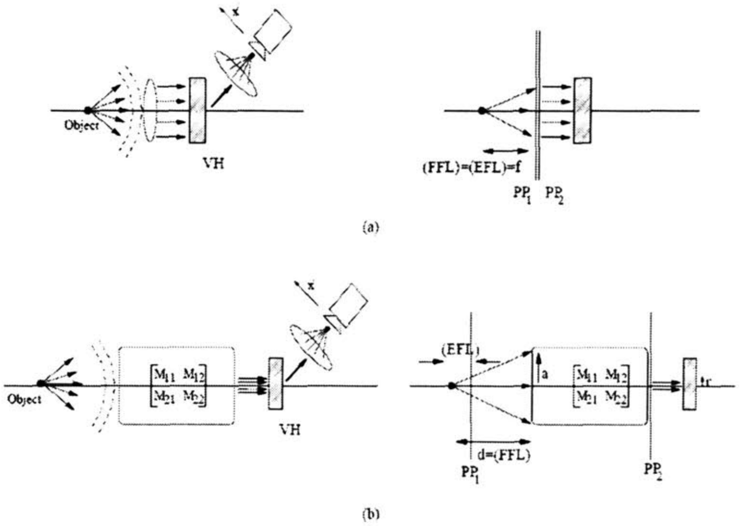

Figure 2-8: Appropriately designed objective optics can improve the Δz_{FWHM} of a VHI system. (a) VHI schematic without objective optics (b) VHI schematic with objective optics.

$$f_1 = \frac{M_{11}t}{M_{11} - 1 - M_{12}t}, \tag{2.48}$$

$$f_2 = \frac{t}{1 - M_{11}}. \tag{2.49}$$

The separation t is selected to locate PP_2 immediately behind the second lens (otherwise the r_{min} requirement becomes more stringent.) PP_2 is exactly on the second lens if $t = f_1$, so in practice we select a slightly higher value for t. It should be noted that the same improvement in resolution can be accomplished by use of a demagnifying telescope or other optical systems; however, the telephoto is one of the most compact and widely available implementations.

Figure 2-9 shows that a telephoto system can be used to increase the working distance without any degradation in the Δz_{FWHM} for VHI. The standalone VHI system had a

NA_{obj} approximating 0.08 by use of a collimating objective lens with $d = f = 50$mm and radius $a = 4$mm to record the hologram and $\theta_s = 30^o$(outside VH lens). The telephoto system was composed of two lenses with $f_1 = 250$mm and $f_2 = 25$mm separated by a distance $t = 500$mm. The object was placed at a working distance $d = FFL = 500$mm in front of the positive lens that had an aperture $a = 12.7$mm. Thus, for the telephoto system, the NA_{obj} approximated 0.025. The actual size of the recorded hologram was $r = 0.65$mm and $\theta_s = 30^o$. It can be seen that both PSFs have the same $\Delta z_{FWHM} \approx 1$mm despite the fact that the stand-alone PR VHI system has a working distance $d = 50$ mm and the telephoto system has a working distance $d = 500$mm.

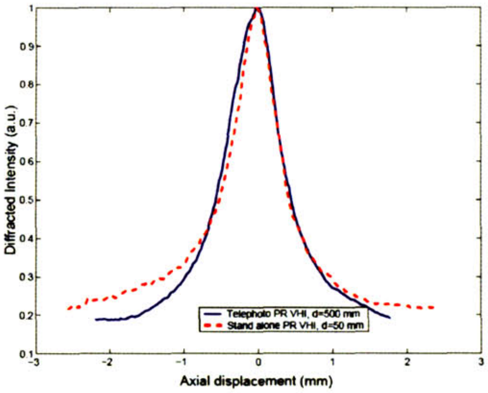

Figure 2-9: An appropriately designed telephoto system can improve working distance d without any degradation in the resolution. PSFs for stand alone VHI system (dashed line) and telephoto VHI system (solid line) show that both systems have $\Delta z_{FWHM} = 1$mm for $d = 50$mm and $d = 500$mm respectively.

VH lenses can also be recorded with other configurations. For example, a spherical reference wave can be used to record the VH and construct a VHI system [17]. Figure 2-10 compares the optimum depth resolution for a planar reference VHI system with a spherical reference VHI system and a confocal profilometry (CF) system as a function of working distance d on a *loglog* scale. We substitute the values $\theta_s = 30^o$, $L = 2$mm, $a = 12.7$mm, $r_{min} = 0.1$mm, and pinhole radius $1.22\lambda d/4a$ in the expressions for a depth resolution for each of these systems. The resulting equations [17] are

$$\Delta z_{FWHM}(PR)_{opt} = 1.5 \times 10^{-6} d^2, \tag{2.50}$$

$$\Delta z_{FWHM}(CF) = 3.50 \times 10^{-6} d^2. \tag{2.51}$$

Thus, the planar reference VHI system has better resolution than the confocal system, and that in turn has better resolution than the spherical reference VHI system. In addition, it is possible to design zoom objective optics for a planar reference VHI system to operate along the lines (1), (2), or (3) as shown in Figure 2-10. Operating along (1) achieves the optimal depth resolution. However, if we are willing to sacrifice some depth resolution, the planar reference VHI system can operate anywhere between lines (3) and (1). In(2), some depth resolution is sacrificed to ensure that the resolution degrades linearly with increasing $d < d^*$, and in (3) more depth resolution is sacrificed to ensure that the depth resolution stays constant over the range $0 \sim d^*$. For the telephoto system, the hologram must be placed at the second principal plane

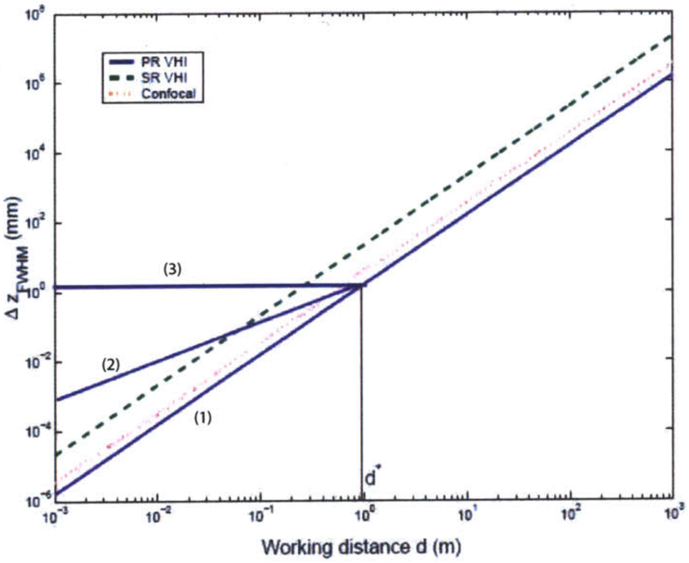

Figure 2-10: Plots of Δz_{FWHM} versus object distance d for PR VHI (solid lines), Confocal systems (dotted line).

PP_2 of the system. An additional consideration for the size r of the collimated beam is that it must act as a field stop. To see why, consider Figure 2-11 where the hologram is placed suboptimally at a distance b behind PP_2. The FoV of this telephoto system is

$$FoV = \frac{2rEFL}{b+L}. \tag{2.52}$$

Thus, it is beneficial to select b as small as possible to fully utilize the parallelism of line scanning.

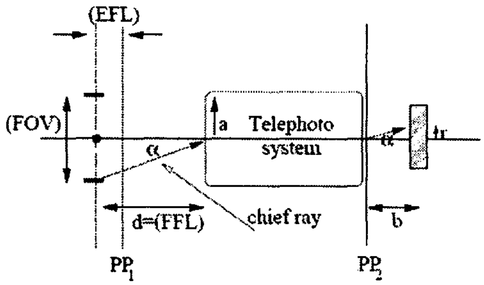

Figure 2-11: Calculation of FOV for telephoto PR VHI system, the chief ray makes an angle α with the optical axis.

2.2.5 Experimental results

For signal beam angle $\theta_s = 30^o$ outside the hologram, Eq.(2.39) yields G =10.2. We performed a series of experiments to determine the experimental value of G in the identical geometry and found experimental G=10.09 as shown in Figure 2-12. The small disagreement with the theory can be explained by the aberrations in our experimental system that were not accounted for in our paraxial theory.

Figure 2-13 compares the theoretical and experimental diffraction patterns captured on a camera for a displacement of δ = 8mm from a Bragg match. A collimating objective lens of focal length f = 50.2mm and radius a = 3.5mm was used to record the hologram. The signal beam was inclined at an angle $\theta_s = 30^o$ outside the hologram and the FT lens had a focal length F = 63.9mm. We can see that the experimentally

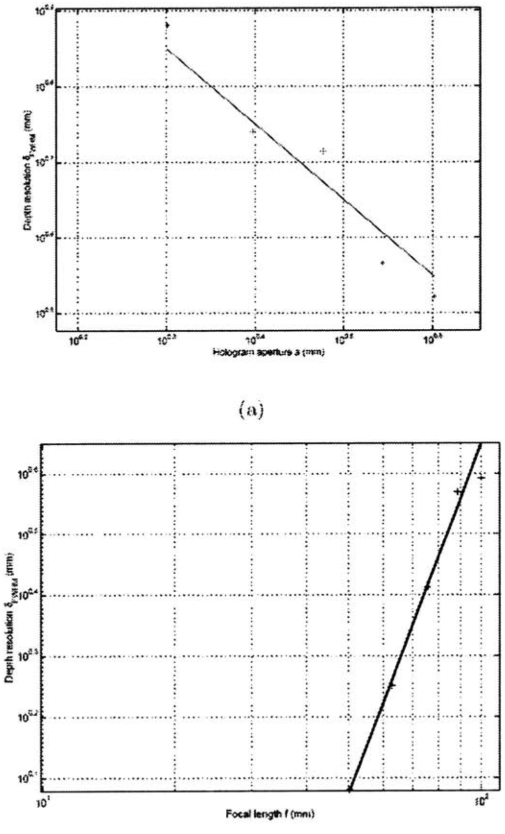

(a)

(b)

Figure 2-12: (a)Theoretical (solid line) and experimental (crosses) Δz_{FWHM} vs a for fixed f and L, confirming the inversely proportional relationship to NA in this case. (b) Theoretical (solid line) and experimental (crosses) Δz_{FWHM} vs f for fixed a and L, confirming the quadratic dependence on f.

and theoretically predicted diffracted patterns match well. Again pixel brightness saturation results in a slightly thicker experimental degeneracy line.

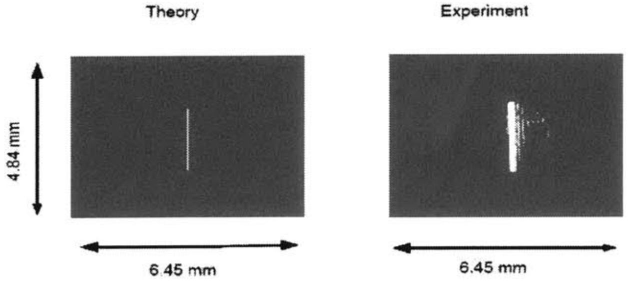

Figure 2-13: Theoretical and experimental diffracted patterns on CCD for PR VHI with a point source displaced $\delta = 8$mm from Bragg match.

Figure 2-15 presents line scan VHI images of what we call "the MIT artifact". The artifact was manufactured on aluminum and consisted of the letters *M, I, T* at different heights as a staircase with a 2mm step size. The letter M was the tallest letter and T was the shortest. A computer-aided design rendering from the model used to machine the artifact is given in Figure 2-14. For the imaging experiments, we employed 2D scanning using two orthogonal Newport$^{\text{TM}}$ CMA-25CCCL actuators and a CCD camera to acquire images of the object one slit at a time by exploiting the straight-line y degeneracy of VHI. The entire experimental setup for image acquisition was controlled with MATLAB. The experimental setup was identical to the one described in Figure 2-4. Figure 2-15(a) is a profilometry image of the object with the surface of the letter M located at the Bragg-matched height. As a result, the letter M appears brightest. The letters I and T are 2 and 4 mm away from the Bragg-matched location and thus appear progressively darker. Figure 2-15(b) is the image with the surface of the letter I located at the Bragg-matched height. Note that the letters M and T appear equally dark. Figure 2-15(c) is the image with the surface of the letter T located at the Bragg-matched height; note that the letters I and M again appear progressively darker. To quantify the Bragg mismatch, we define $P_{i,j}$ to be the average intensity of the letter i when the letter j is at the Bragg-matched location.

The measured values of the intensity are given in Table 2.1. The corresponding ratios are given in Table 2.2, which are in good agreement with the estimates from the PSF calculation and experiments (Figure 2-6.)

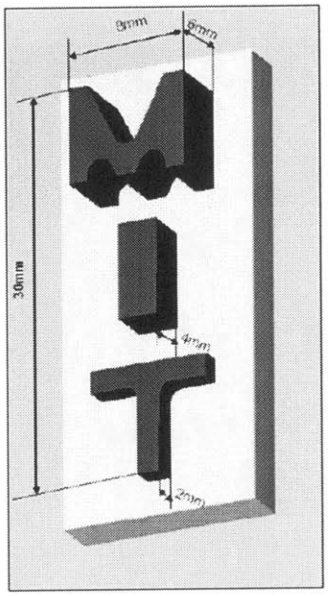

Figure 2-14: The actual CAD rendering of the object, fabricated letters MIT.

Finally, Figure 2-16 presents profilometry image of the same object with use of telephoto objective optics. The telephoto consisted of the same optical elements and setup as described in Section 2.2.4. From the PSF of Figure 2-9, we can see that the collector optics allow us to achieve a $\Delta z_{FWHM} \approx$ 1mm for an object located $d =$ 500mm away. Figure 2-16 shows a progression of images referenced at the three characteristic heights of the artifact similar to Figure 2-15. The average powers and power ratios are given in Tables 2.3 and 2.4, respectively. Again, good agreement with the PSF data of Figure 2-9 is observed.

2.3 Summary

We have presented analysis and characterization of a VHI profilometry system by using a transmission VH lenses recorded with planar wave reference beams. The

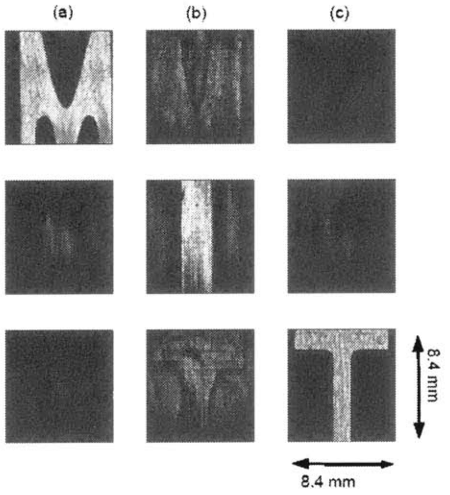

Figure 2-15: VH images of the fabricated letters MIT placed 50.2mm away from the entrance pupil of the system. (a) is a volume holographic image of the object obtained by a 1D scan with surface of the letter M being placed at Bragg matched location, (b) is an image of the object obtained by a 1D scan with surface of the letter I being placed at Bragg matched location and (c) is an image of the object obtained by a 1D scan with surface of the letter T being placed at Bragg matched location.

Table 2.1: Measured intensity values for the stand-alone VHI (a.u.)

Measured intensity
$P_{M,M} = 10.6 \pm 0.13$
$P_{I,M} = 2.05 \pm 0.28$
$P_{T,M} = 1.89 \pm 0.27$
$P_{M,I} = 2.51 \pm 0.25$
$P_{I,I} = 9.21 \pm 0.14$
$P_{T,I} = 2.18 \pm 0.29$
$P_{M,T} = 1.80 \pm 0.24$
$P_{I,T} = 2.05 \pm 0.31$
$P_{T,T} = 9.59 \pm 0.13$

Table 2.2: Ratios of intensity values calculated from Table 2.1

Intensity ratios
$\frac{P_{I,M}}{P_{M,M}} = 0.19 \pm 0.05$
$\frac{P_{T,M}}{P_{M,M}} = 0.17 \pm 0.03$
$\frac{P_{M,I}}{P_{I,I}} = 0.27 \pm 0.04$
$\frac{P_{T,I}}{P_{I,I}} = 0.24 \pm 0.07$
$\frac{P_{M,T}}{P_{T,T}} = 0.19 \pm 0.05$
$\frac{P_{I,T}}{P_{T,T}} = 0.21 \pm 0.04$

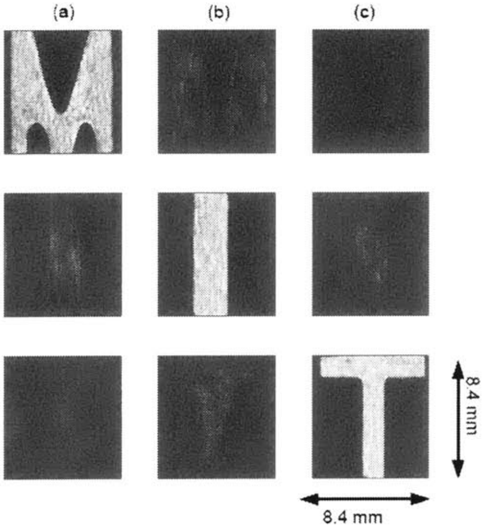

Figure 2-16: VH images using collector optics of the fabricated letters MIT placed 500 mm away from the entrance pupil of the system. (a) is a volume holographic image of the object obtained by a 1D scan with surface of the letter M being placed at Bragg matched location, (b) is an image of the object obtained by a 1D scan with surface of the letter I being placed at Bragg matched location and, (c) is an image of the object obtained by a 1D scan with surface of the letter T being placed at Bragg matched location.

Table 2.3: Measured intensity values for the telephoto VHI (a.u.)

Measured intensity
$P_{M,M} = 10.3 \pm 0.14$
$P_{I,M} = 1.96 \pm 0.35$
$P_{T,M} = 1.55 \pm 0.3$
$P_{M,I} = 2.06 \pm 0.28$
$P_{I,I} = 9.83 \pm 0.16$
$P_{T,I} = 2.00 \pm 0.33$
$P_{M,T} = 1.50 \pm 0.24$
$P_{I,T} = 1.89 \pm 0.35$
$P_{T,T} = 9.40 \pm 0.15$

Table 2.4: Ratios of intensity values calculated from Table 2.3

Intensity ratios
$\frac{P_{I,M}}{P_{M,M}} = 0.19 \pm 0.07$
$\frac{P_{T,M}}{P_{M,M}} = 0.15 \pm 0.04$
$\frac{P_{M,I}}{P_{I,I}} = 0.21 \pm 0.04$
$\frac{P_{T,I}}{P_{I,I}} = 0.20 \pm 0.07$
$\frac{P_{M,T}}{P_{T,T}} = 0.16 \pm 0.05$
$\frac{P_{I,T}}{P_{T,T}} = 0.20 \pm 0.05$

behavior of VHI with respect to depth resolution is summarized as follows:

1. inverse linear dependence on hologram thickness L,
2. quadratic dependence on the working distance d,
3. inverse quadratic dependence on the numerical aperture (NA), and
4. reduced scanning time by exploiting the Bragg degeneracies of the volume holograms.

We also comprehensively investigated the approach of using auxillary objective optics design to optimize the imaging resolution of VHI over long working distance. A maxium likelihood estimation method that accomplish this goal at the post-processing stage is the topic of the next chapter.

Our experimental tests of VHI were conducted using an artifact which was fabricated specifically for the purposes of our characterization, and we presented the "raw" image data, *i.e.*, the intensity measurements directly as they were returned by the detector or camera. It would also have been possible to apply post-processing techniques to further improve image quality. This possibility is promising for two reasons: first, because the system PSF can be very well characterized; second, because the PSF itself can be fine-tuned to improve the deconvolution results by simple modifications to the holographic recording process, *e.g.*, using deliberately aberrated reference beams or non-planar signal beams.

Chapter 3

Digital post-processing in volume holographic profilometry

In Chapter 2, we studied the imaging behavior of VH lens and discussed the design of laser illumination VHI system for optical profilometry. The objective optical design to extend the working distance of VHI while preserving depth resolution was studied and implemented experimentally. The 3D reconstruction model shows that the planar wave reference (PR) VHI profilometry system with active monochromatic illumination can achieve < 2mm depth resolution at a relatively long (50cm) working distance. For step-wise object metrology, the resolution can be improved to $< 150\mu$m at the same working distance using the oblique axis setup [15]. These methods require two dimensional scanning (one lateral and one longitudinal) to complete the measurement.

For optical profilometry instruments based on filtering at the spatial spectrum plane to achieve depth discrimination, longitudinal resolution typically has inverse quadratic dependence on the numerical aperture (NA). Since NA is typically much smaller than 1 (without immersion), especially for the long working distance profilometry, longitudinal resolution is worse than lateral resolution, which is inversely proportional to the NA. Therefore, to improve the depth or longitudinal resolution is a major concern for improving the performance of VHI profilometry system. The telephoto objective optics design in Chapter 2 gives the solution based on optimizing the optics design.

In this Chapter, we discuss an alternative, digital post-processing. To characterize the resolution improvement and the costs of post-processing in a concrete fashion, we introduce two gain factors γ and β defined as follows:

1. Resolution gain factor

   $$\gamma = \frac{\text{depthresolution } \Delta z \text{ without post} - \text{processing}}{\text{depthresolution } \Delta z \text{ with post} - \text{processing}},$$

   denotes the depth resolution improvement through post-processing;

2. Interpolation gain factor

   $$\beta = \frac{\text{number of depth layers reconstructed}}{\text{number of raw images acquired}},$$

   denotes the reduction in image acquisition time because of post-processing.

One way to achieve satisfactory reconstruction with resolution gain is to acquire more raw images. The number of raw images needed for reconstruction with an arbitrary post-processing method is γ/β times more than that for reconstruction without post-processing ($\gamma = 1, \beta = 1, \gamma/\beta = 1$).

In Section 3.1 we discuss the mathematical formulation to implement the digital post-processing, including digitization the VHI imaging process, and analyze the cause which lowering the depth resolution. In Section 3.2, we propose a digital post-processing model based on the maximum likelihood (ML) estimation, followed by discussion of using the Viterbi algorithm (VA) to solve the ML problem. We showed that by combining the use of the reduced complexity Viterbi algorithm (RCVA) and physical constraints due to the reflective nature of the object, computational cost can be reduced dramatically. In Section 3.3, we propose using digital post-processing not only to improve imaging resolution [14] but also to interpolate object features between the depth layers which were captured in the new image. We show that this technique can be combined with multiplexing VH lenses to reduce or eliminate depth scanning [49, 50].

3.1 Crosstalk in volume holographic profilometry - the imaging channel characteristics

To realize post-processing, the object and image space must be discretized. The image plane is naturally discretized by the pixel size of the CCD camera. Because our interest here is only to improve the longitudinal resolution, we chose to discretize the object space in the lateral y dimension according to the pixel size of the CCD camera (see Figure 2-2), taking into account of the lateral magnification of the imaging system. The lateral x dimension is slightly different. Since the 3D ML estimation is computationally intensive, we intend to simplify it by breaking it into multiple independent 2D problems. This is done by taking advantage of the Bragg matching slit property of the VHI. That is, x-discretization must ensure that adjacent $y-z$ slices can be processed independently. Let us use p_x and p_y to denote the size of camera pixels. If the holographic slit width $\Delta x_B < p_x f_1/f_2$, the holographic slit falls onto a single column of CCD pixels. The pixel size thus becomes the resolution limit of the imaging system and $p_x f_1/f_2$ is naturally chosen as the discretization step. On the other hand, if $\Delta x_B > p_x f_1/f_2$, Δx_B must be chosen as the discretization step to ensure that adjacent $y-z$ slices are approximately independent of each other. In the longitudinal dimension z, we simply choose the discretization size as $\Delta z_{FWHM}/\gamma$,where γ is the resolution gain function defined in the preemble to this chapter. So the object space is finally discretized to a 3D mesh grid with voxel dimensions

$$\begin{aligned} v_x &= \max\left(\Delta x_B, \frac{p_x f_1}{f_2}\right), \\ v_y &= \frac{p_y f_1}{f_2}, \\ v_z &= \frac{\Delta z_{FWHM}}{\gamma}. \end{aligned} \tag{3.1}$$

Because we have assumed that object reflectance is uniform, we can further quantize the object space to a binary mesh grid according to the following rule: each voxel takes the value '1' if there is a reflective surface segment in it, and '0' if there is no surface. Let us consider the 2D $y - z$ frames extracted from the 3D binary mesh grid model. According to the discretization rules given in Eq.(3.1), by neglecting the diffraction by the hologram outside the Bragg-matched angular range (*i.e.*, what in the holographic storage context was called "inter-page crosstalk" [41]), we can process the data frame-by-frame independently. The schematic of discretization and quantization in a $y-z$ holographic slit is shown in Figure 3-1. With this discretization and quantization, the profilometric imaging problem can be treated as the problem of reconstructing a 3D binary model from raw data that are blurred by the imaging channel and corrupted by noise. We use $f(m, n)$ to denote the binary object profile along a single holographic slit, where m and n are the indices along the z and y directions, respectively. Because of quantization, $f(m, n)$ is a binary-valued matrix.

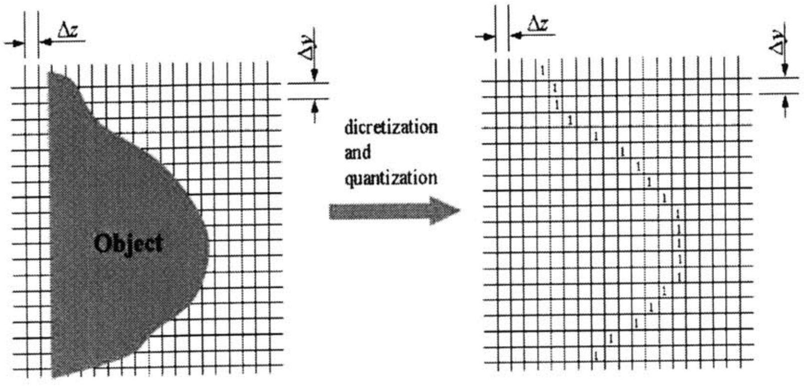

Figure 3-1: Discretization and quantization of a holographic slit. Pixels denote object reflective surface are assigned binary value of '1'.

The original object $f(m, n)$ must be reconstructed from the measured raw images that have been corrupted by crosstalk in the imaging process and by additive noise. Crosstalk is due to the non-zero extent of the system PSF. This means that not only the desired voxel but also its neighbors within the $y-z$ slice contribute to the photon flux arriving at the corresponding CCD pixel. This effect is usually referred to as Inter Symbol Interference (ISI) in communication theory. ISI, in conjunction with the noise, eventually reduce the resolution of the imaging process. VHI can be operated with both coherent and incoherent illumination, therefore different system PSF and ISI functions must be analyzed. In coherent illumination, the two dimensional (2D) ISI within a single $y-z$ slice can be derived from Eq. (2.34) as

$$h_c(i,j) = \iint \operatorname{rect}\left(\frac{x'-\theta_s F}{v_x}\right)\operatorname{rect}\left(\frac{y'}{v_y}\right) \cdot \operatorname{circ}\left[\frac{\sqrt{(x'-\theta_s F)^2 + (y'+iv_y)^2 f^2}}{Fa\left|jv_z\right|}\right] \mathrm{d}x'\mathrm{d}y'. \quad (3.2)$$

The incoherent PSF can be derived by taking the magnitude square of the corresponding coherent PSF as [2]

$$h_i(i,j) = \left|h_c(i,j)\right|^2. \quad (3.3)$$

Generally, $h_c(i,j)$ and $h_i(i,j)$ have infinite support in both dimensions. However, in practice, for computational implementation, we truncate it to a finite size, such that 99% energy remains within the support. A calculated and truncated $h_i(i,j)$ (99% energy, with extent of l=3, s=9) for a VHI with f_1 = 25mm, a=4mm is shown in Figure 3-2. Consider the case when the VHI profilometer is focused on the n_f-*th* longitudinal layer of the object. Then the image formed on the CCD is a one dimensional intensity distribution (along y). We denote it as $I_c(m,n_f)$ and $I_i(m,n_f)$, corresponding to coherent and incoherent illumination, where m is the pixel index along y and n_f is the index indicating the corresponding focusing depth layer. Thus, $I_c(m,n_f)$ and $I_i(m,n_f)$ are given as

$$I_c(m,n_f) = \left|\sum_{i=-(l-1)/2}^{i=(l-1)/2}\sum_{j=-(s-1)/2}^{j=(s-1)/2} f(m+i,n_f+j)\,h_c(i,j)\right|^2 + w(m,n_f), \quad (3.4)$$

and

$$I_i(m,n_f) = \sum_{i=-(l-1)/2}^{i=(l-1)/2}\sum_{j=-(s-1)/2}^{j=(s-1)/2} f(m+i,n_f+j)\,h_i(i,j) + w(m,n_f), \quad (3.5)$$

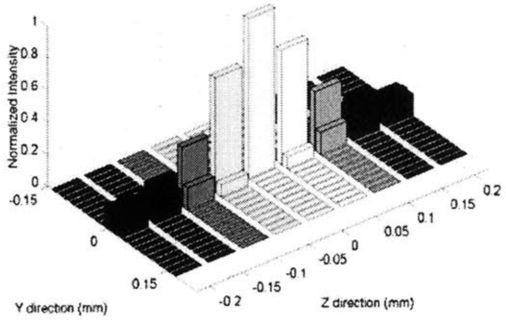

Figure 3-2: A calculated ISI (99% energy) for a VHI with $f = 25\text{mm}$, $a = 4\text{mm}$.

where s and l are the physical extents of the ISI in the z and y dimensions respectively, and $w(m, n_f)$ is the additive noise. After carrying out the square term in Eq.(3.4), $I_c(m, n_f)$ can be written as

$$I_c(m,n_f) = \sum_{i=-(l-1)/2}^{i=(l-1)/2} \sum_{j=-(s-1)/2}^{j=(s-1)/2} f\left(m+i, n_f+j\right) \left|h_c\left(i,j\right)\right|^2$$

$$+\,2 \sum_{i=-(l-1)/2}^{i=(l-1)/2} \sum_{j=-(s-1)/2}^{j=(s-1)/2} \sum_{\substack{i'=-(l-1)/2 \\ i'\neq i}}^{i=(l-1)/2} \sum_{\substack{j'=-(s-1)/2 \\ j'\neq i}}^{j=(s-1)/2} f\left(m+i, n_f+j\right) f\left(m+i', n_f+j'\right)$$

$$h_c\left(i,j\right) h_c\left(i',j'\right) + w\left(m,n_f\right), \quad (3.6)$$

It can be seen that the first term in Eq.(3.6) is exactly the same as Eq.(3.5), after substituting Eq.(3.3). The difference lies on the second term, which is given by the cross-product between the field responses from different reflective surface segments within the truncated ISI area. In profilometry of a reflective object, the distribution of $f(m,n)$ is highly constrained, as in each row of $f(m,n)$, there must exist one and only one single '1', corresponding to a single reflective surface segment at each lateral position. If $f(m,n)$ is an uncorrelated random profile and consists of N depth layers, the expectation value of the second term in Eq.(3.6) is given as

$$\langle e\left(m,n_f\right)\rangle \propto \frac{l}{N}\sum_{i=-(l-1)/2}^{i=(l-1)/2}\sum_{j=-(s-1)/2}^{j=(s-1)/2} f\left(m+i,n_f+j\right)\left|h_c\left(i,j\right)\right|^2 \tag{3.7}$$

Since $\left|h_c\left(i,j\right)\right|^2 < 1$, it can be seen that if $N \gg 1$, contribution from this term can be neglected and one may use the incoherent linear imaging model Eq.(3.5) even if the illumination is coherent. This is the case in the numerical simulations shown later in Section 3.3.1. Real world objects are not purely random, *i.e.*, the lateral correlation length is comparable with the number of the object depth layers. In this circumstance, the above approximation does not hold any more, and one must use the nonlinear (coherent) model Eq.(3.4) and (3.6) to formulate the imaging process.

3.2 Post-processing with Maximum Likelihood (ML) estimation via Viterbi algorithm to improve depth resolution

3.2.1 ML estimation formulation

When each depth position of the entire object space is covered by longitudinal scanning, multiple intensity measurement vectors as given by Eq.(3.5) or (3.4) are obtained. By concatenating these measurement vectors we form an intensity measurement matrix under coherent illumination

$$I_c(m,n) = \left|\sum_{i=-(l-1)/2}^{i=(l-1)/2}\sum_{j=-(s-1)/2}^{j=(s-1)/2} f\left(m+i,n+j\right)h_c\left(i,j\right)\right|^2 + w\left(m,n\right), \tag{3.8}$$

or under coherent illumination

$$I_i(m,n) = \sum_{i=-(l-1)/2}^{i=(l-1)/2}\sum_{j=-(s-1)/2}^{j=(s-1)/2} f\left(m+i,n+j\right)h_i\left(i,j\right) + w\left(m,n\right), \tag{3.9}$$

We would like to emphasize here that $h_c(i,j)$, $h_i(i,j)$, and $w(m,n)$ are not binary, therefore $I(m,n)$ is not a binary matrix either, different from $f(m,n)$. The aim of post-processing for super-resolution is to reconstruct $f(m,n)$ at the desired voxel size, *i.e.*, with a desired resolution gain γ. To accomplish this goal, we treat Eq.(3.8) and (3.9) as parameter estimation problems, where f is a deterministic but unknown binary matrix. I is obtained through a particular realization of the imaging process, which is treated as a random process. One of the most commonly used solutions to the parameter estimation problem is the Maximum Likelihood (ML) estimation. It is known that when an efficient estimator exists, the ML estimation always converges to it. The ML estimation of f from measurement I is

$$\hat{f}(I) = \arg\max_{\hat{f}} \left\{ p\left(I|\hat{f}\right) = \prod_{m,n} p\left[I(m,n)\,|\hat{f}\right] \right\}, \tag{3.10}$$

where $p(\cdot|\cdot)$ denotes conditional probability density function of an intensity measurement given the object shape. Here we assume that the optical signal received by the profilometer is strong enough such that the noise $w(m,n)$ is well represented by a white Gaussian process of zero mean and variance σ^2. Thus, Eq.(3.10) can be explicitly solved as

$$\hat{f}(I) = \arg\max_{\hat{f}} \left\{ \prod_{m,n} \left(\frac{1}{2\pi\sigma^2}\right)^{\frac{m+n}{2}} \exp\left\{ \frac{-\sum_{m,n}\lambda(m,n)}{2\sigma^2} \right\} \right\} \tag{3.11}$$

and, finally

$$\hat{f}(I) = \arg\min_{\hat{f}} \left(-\sum_{m,n} \lambda(m,n) \right), \tag{3.12}$$

where

$$\lambda(m,n) = \left[\left(\hat{f} * h_i\right)(m,n) - I(m,n) \right]^2 \tag{3.13}$$

when the illumination is incoherent, and

$$\lambda(m,n) = \left[\left| \sum_{i=-(l-1)/2}^{i=(l-1)/2} \sum_{j=-(s-1)/2}^{j=(s-1)/2} \hat{f}(m+i,n+j)\, h_c(i,j) \right|^2 - I(m,n) \right]^2 \tag{3.14}$$

when the illumination is coherent.

3.2.2 The Viterbi algorithm solution and computational complexity reduction

The Viterbi algorithm (VA) is a commonly used approach for solving ML estimation. VA is widely used in CDMA channel estimation and signal detection [51]. In VA, all the possible combinations of the ISI values (called states) in each phase of the measured sequences (called stages) are listed in a two dimensional trellis. The trellis for an example 1-D Viterbi decoding is shown in Figure 3-3. In the example, the signal f is a binary sequence $\{1, 0, 1\}$, passing through a linear system characterized by the ISI function h=$\{0.5, 0.3, 0.2\}$ and corrupted by additive noise w=$\{0.1, -0.1, 0, -0.1, -0.1\}$. Thus, the measurement is a sequence g=$\{0.6, 0.2, 0.7, 0.2, 0.1\}$. A stage, or a column in the trellis encompasses all the possible values of the estimate signal bits named "state". For an ISI of length s, there are totally 2^{s-1} states for binary signal f. Without loss of generality, we can assume $\hat{f} = 0$ outside the boundary of f, *i.e.*, all the paths start from '00' state at stage 1. The value of the current estimate of signal bit is implied by the path connecting the current stage and the next stage. As an example, consider stage 1 and trace the two paths which lead to state '00' or '01' at the stage 2, depending on whether $\hat{f}\,(i)$ takes the value of '0' or '1', respectively. The numbers superimposed on the arrows denote the corresponding $\hat{f}\,(i)$ and $\lambda\,(i)$ associate with current path segment. VA finds the path with minimal accumulated λ by an efficient dynamic way according to the following steps:

1. Compute $\lambda(i)$ for each path leaving stage i (see, Figure 3-3, $\hat{f}\,(i)$ and $\lambda\,(i)$ are labeled for stage 1 and stage 2);

2. For each state in stage $i+1$, keep only the path with minimal accumulated error $\sum_{j=1}^{i} \lambda\,(i)$ arriving at that state, and eliminate all the other paths.

All the sub-optimal paths that were eliminated in step 2 must not be part of the final global optimal path. This is because, though the future path evolutions are unknown,

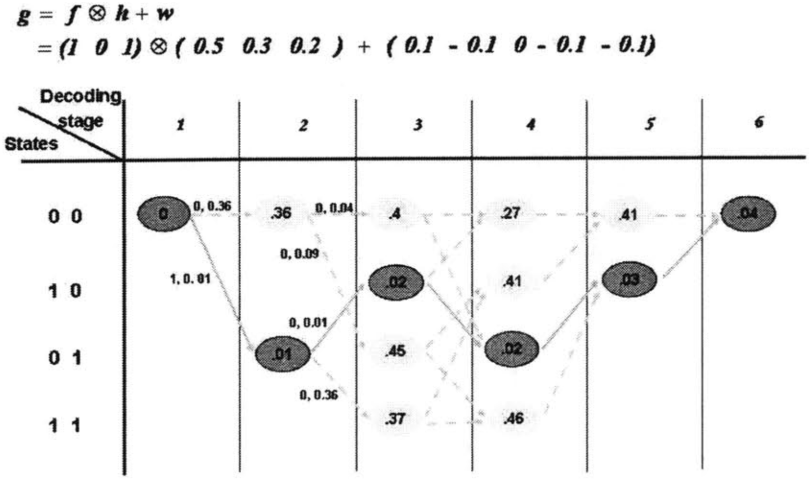

Figure 3-3: Trellis for a 1D binary decoding using the Viterbi algorithm.

they must start from one of the four states at stage $i+1$. Since there are multiple paths from stage i leading to each of the four states in stage $i+1$, the path with larger accumulated λ must not be the optimal, thus this path can be eliminated. The dynamic eliminations can be done at every stage except the starting and ending stages. Therefore, for relatively long signal sequences, VA reduces computational complexity exponentially. Rigorous explanation of the Viterbi algorithm is beyond the scope of this thesis. Interested readers may refer to [15] and [19].

For the 2D ML estimation problem stated in Eq.(3.13) and (3.14), a straightforward but inefficient method is to treat each column of the binary-valued object slice in the extent of the ISI as an $M-ary$ variable, where $M=2^l$. Thus, the 2D binary matrix estimation problem can be solved as a 1D estimation problem [52]. However, the computational complexity of VA increases exponentially with the number of the states in the trellis. The number of states for each stage in this $M-ary$ method is $2^{l(s-1)}$, which also increases exponentially with the size of the ISI. So when the lateral size of the ISI is larger than 3, the $M-ary$ method becomes computationally impractical for fast reconstruction. The computational complexity can be reduced by using the row-by-row decision feedback VA, referred to as Reduced Complexity Viterbi Algorithm (RCVA) [52]. RCVA uses each estimated row as prior knowledge in the estimation of the next row of $\hat{f}$. RCVA solution is sub-optimal, but gives very good reconstruction results in practice. The number of states after applying RCVA is reduced from $2^{l(s-1)}$ to $2^{l(s-1)/2}$. In profilometry, because the object is opaque and consists of a "single reflective surface", there is a single '1' in each row along the z direction in the 3D binary object model. In another words, this constraint means that in the 2D object $f(m,n)$, there exists one and only one single '1' in each row. Therefore, the possible combinations for each row are reduced from 2^s to s. Thus, in the 2D trellis, only $(s-1)l$ states are consistent with the "single reflectance surface" constraint. For a 3×9 ISI and 10 stages trellis, the computational complexity is thus reduced by factor of 1.4×10^{45} compared to the normal $M-ary$ method.

Further reduction of the computation can be achieved by applying the scanning transition constraint as follows. By using the decision feedback with RCVA method, only two rows of the 3 ISI are considered. Then the possible state values for an arbitrary column (stage) are $[00]^T$, $[10]^T$, $[01]^T$, $[11]^T$. These denote estimates of the object when there is no surface in either voxel, a surface segment in the upper voxel, lower voxel and both voxels, respectively. We denote the four states as 0, 1, 2, 3 in a $4-ary$ notation. Because depth scanning in our experiment are implemented along one way, forward or backward, the transitions are also highly constrained as can be seen from the following example. For simplicity, let us consider an ISI which $s = 4$. Suppose that a path starts with the state '0000', which indicates no surface segment in either neighboring lateral voxel within the longitudinal extent. The only four valid evolutions to the next stage are '0000', '1000', '2000', and '3000', shown as thick arrows in Figure 3-4. Figure 3-4 also gives the full transition map between two arbitrary stages in the Viterbi trellis. It can be seen that only a few transitions are valid between stages. A transition map with full 9 bit ISI length can be plotted similarly.

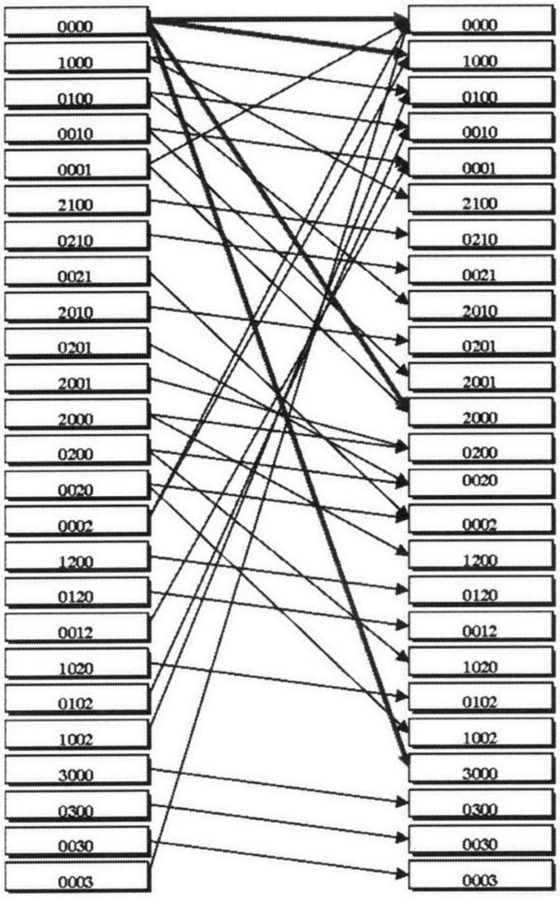

Figure 3-4: Constrained state transition map for using Viterbi algorithm in VHI profilometry image restoration.

3.2.3 Experimental results of the depth resolution improvement through digital post-processing

Numerical simulations were carried out with a 3-step object. For simplicity, only a single holographic slit, *i.e.*, the slice in the $y - z$ plane of the object was used. The VHI system used was modeled after the setup of Figure 3-5, with the ISI plotted in 3×9 pixels as shown in Figure 3-2. Optical parameters such as f_1, f_2, a, L, *etc.* determine the actual extent of the ISI. However, to demonstrate the reconstruction with simulation, these parameters can be chosen arbitrarily as long as the pixel sizes of the object slice and the ISI of the VHI match each other. Figure 3-6 shows results from numerical experiments of VHI profilometry surface reconstruction using our method. The testing surface consisted of 3 steps as shown in cross-section in Figure 3-6(a). Figure 3-6(b) shows the simulated images captured on the CCD using VHI optics. The images were numerically corrupted by the 3×9 ISI shown in Figure 3-2 and by additive white Gaussian noise with SNR=10dB (first row) and 7dB (second row) respectively. Figure 3-6(c) shows the reconstructed surface with a thresholding method, which simply picks up the maxima at each row as the estimated positions of the surface segments. Figure 3-6(d) shows the VA reconstructed surface. It can be seen that when noise is low, VA can reconstruct the original surface with very few errors. When noise is high, VA is considerably more robust than thresholding.

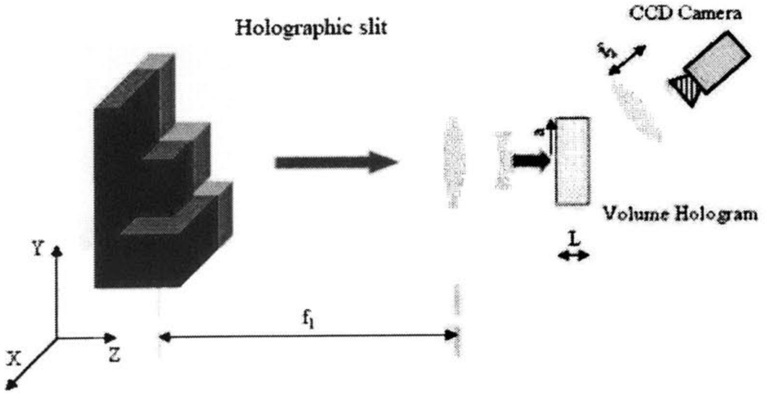

Figure 3-5: Schematic of a VHI profilometer.

We applied the VA-corrected VHI surface profilometry method in experiment to the

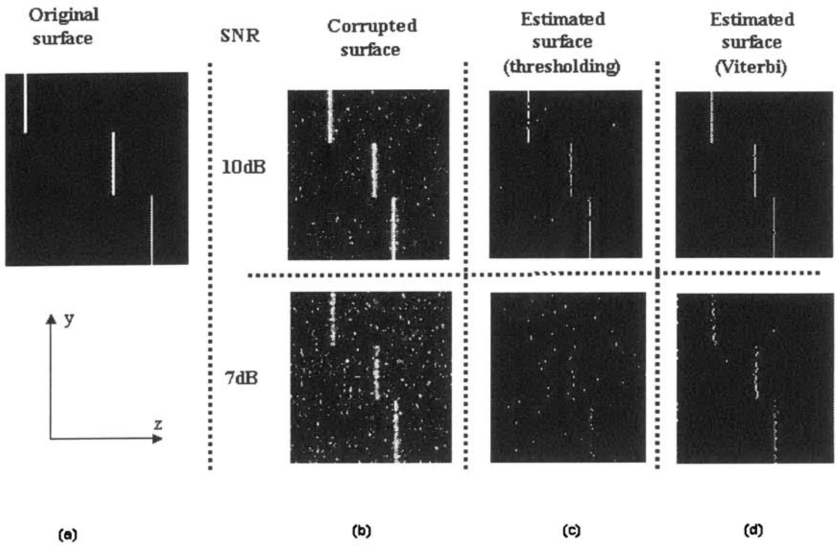

Figure 3-6: Numerical experiments of using VA to improve VHI reconstruction of a simulated surface consisting of 3 steps.

same aluminum "MIT" artifact (see Figure 2-14). We employed 2D scanning using two orthogonal Newport$^{\text{TM}}$ CMA-25CCCL actuators and a CCD camera to acquire images of the object, one slit at a time. The experimental setup was identical to the one described in Figure 3-5. We intentionally degraded the nominal depth selectivity of the VHI to 2.5mm by closing down the aperture of the optics. In order to demonstrate that VA does not degrade lateral resolution while achieving super-resolution in the depth dimension, we manufactured a 0.2mm wide, 0.5mm deep trench on the letter I. The trench width was chosen to correspond to one pixel on CCD through the magnification of the VHI optics. Figure 3-7(a) shows five measured images focused on different depth positions. Figure 3-7(b) shows the Viterbi-corrected reconstructed surface. The pixel error rate, defined as the fraction of falsely estimated pixels, was less than 0.1%. In the magnified image of the I, it can be seen on the reconstructed object that a small trench with lateral size of v_y=0.2mm and depth size of v_z=0.5mm has been reconstructed. Thus, our claim that VA preserves lateral resolution is verified.

In summary, we demonstrated the use of the Viterbi algorithm to clean up VHI images for high resolution profilometry object reconstruction. We achieved $\gamma = 5$ and $\beta = 1$ in the depth dimension, without sacrificing the lateral resolution. The cost for depth resolution is that more scanning is needed, thus resulting in $\gamma/\beta = 5$ times more imaging time. This trade-off will be addressed in the next section by the use of digital post-processing to interpolate the object.

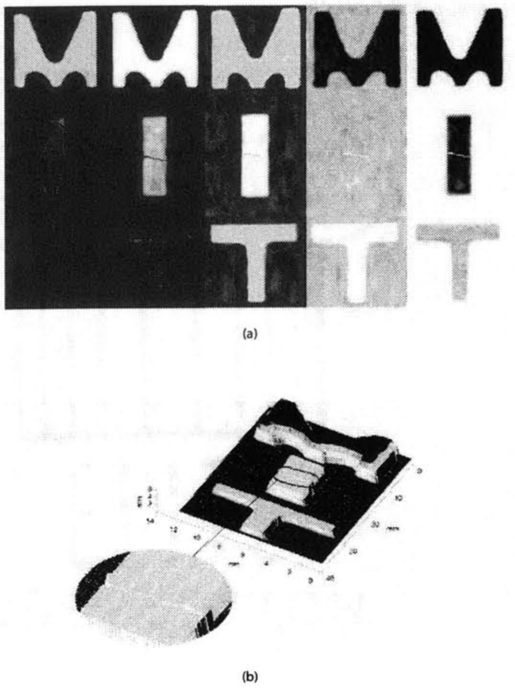

Figure 3-7: (a) reconstructed artifact of five times super-resolution with low error bits, (b) five consecutive raw images captured by a deliberately degraded VHI.

3.3 Interpolating depth features with digital post-processing

In this section we show that, the RCVA can be used to reconstruct the object even if the VHI profilometer does not acquire raw data for every object slice; we demonstrate that a multi-layer object may be perfectly reconstructed even if only one out of every four depth layers are measured, *i.e.*, in Eq.(3.9) and (3.8), we only know the values of

$I(m, n)$ every four column. Since the raw images were not acquired at every desired depth, imaging acquisition (scanning) time was reduced. Despite the apparent lack of data, reconstruction recovered all the features with depth resolution equivalent to the depth between the desired layers. Using the gain terminology developed in the preemble to this chapter, we achieved $\gamma = 4, \beta = 4$. The RCVA application was as follows: When tracing the paths in the VA trellis, we compare the accumulated mean square error (MSE) $\lambda(m, n)$ through each path with the measurements at every four stages, since the measured value at the interlaced stages is unknown. The MSE accumulated while evolving through these "missing" stages is assumed to be nearly constant for all the paths. This assumption is approximately correct when the noise is much smaller compared to the lowest value in the ISI function. In this case, the accumulated MSE at the "missing" stages of the different paths varies in a very narrow region. Because path elimination happens every four stages instead of every stage, the computational complexity increases. Thanks to the computational complexity reduction by use of surface and translation constraints, the computation is still manageable in practice even with a personal computer. Numerical simulations and experimental results in the next two sections show that even though the reconstruction method is not rigorously guaranteed for optimality, the estimation works well, especially when measurement noise is low. This is because of the single reflectance property of the object, *i.e.*, the possible values of the "signal" are strongly constrained.

3.3.1 Numerical simulations

Numerical simulations were carried out with a randomly generated object (see Figure 3-8). The simulation scheme is the same as described in Section 3.2.3. The VHI was simulated to scan the object once every four depth layers and the acquired images were concatenated as shown in Figure 3-9. The raw images were generated based on the assumptions of coherent illumination and white Gaussian noise distribution. It is seen that the raw images were degraded by the ISI function of the imaging channel and the noise. Images were concatenated so that the columns corresponding to the un-scanned depth positions were entered as zeros (black). The metric used to evaluate the performance of the reconstruction was the mean reconstruction error (MRE) between the reconstruction and the real object, defined as

$$e = \frac{1}{M} \sum_{k=1}^{M} |d|_k , \tag{3.15}$$

where M=64 is the lateral size (count in pixels) of the object and $|d|_k = \left|\hat{f} - f\right|$. We compared the performance of our reconstruction method with a commonly used peak finding algorithm based on cross-correlation [53]. In the cross-correlation based method, raw images were first concatenated as mentioned above. Then, the 2D ISI function was used as the kernel to compute the correlation with the concatenated raw data. The locations where the object surface exists were estimated as the locations of the cross-correlation peaks. Simulations were carried out at three different noise levels, with SNR =10, 15, and 20. The corresponding concatenated raw images are shown in Figure 3-9. Reconstructions using the RCVA based method (both coherent and incoherent reconstruction models were used) and the cross-correlation peak finder method are shown in Figures 3-10 through 3-12. The MREs of the reconstructions using these three methods at the three different noise levels are listed in Table 3.1. It can be seen that the RCVA based method outperforms the cross-correlation peak finder at all noise levels, and reconstructs the object nearly without error when the SNR is high. However, the theoretically exact coherent RCVA reconstruction only

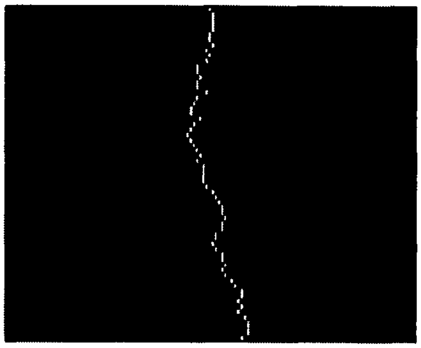

Figure 3-8: Random generated 2D surface for VHI profilometry post-processing simulation using RCVA.

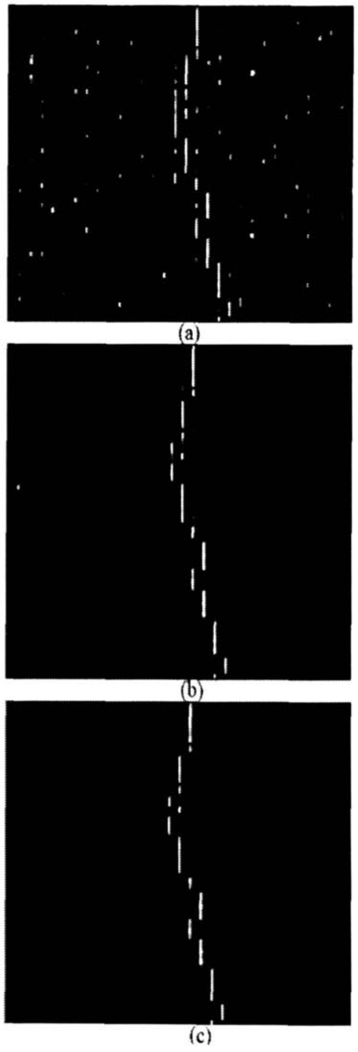
(a)

(b)

(c)

Figure 3-9: Concatenated raw images for VHI profilometry post-processing simulation using RCVA, with SNR (a)=10, (b)=15 and (c)=20

Table 3.1: Comparison MRE of simulated object surface reconstruction with RCVA and Cross-correlation based algorithms, at three different noise levels.

SNR	10	15	20
RCVA(incoherent)	3.9125	0.7500	0.0469
RCVA(coherent)	3.5531	0.6370	0.0335
Cross-correlation	7.6499	1.7343	0.2344

gives marginal improvement over the its linear approximated counterpart. This results agree with the discussion in section 3.1, which pointed out that when $N \gg 1$, the cross terms in the nonlinear model can be neglected (In this case, $N = 128$, $l = 9$).

3.3.2 Experimental results

The experimental demonstration of the VA based super-resolution VHI profilometry was applied using a plastic LEGO$^{\text{TM}}$ model as object. The VHI profilometer was setup as shown in Figure 3-5, with the following parameters: $f_1 = 100$mm, f_2=25mm, $a =$ 4.2mm, $L = 2$mm, $\theta_s = 30^o$. To demonstrate super-resolution, we deliberately used a small aperture to degrade the depth resolution to 6.5mm. The target object consisted of eight layers at different depths (see Figure 3-13). The layers were separated by approximately 1.6mm, which is four times less than the nominal resolution. The embossed "LEGO" logos on the disk area which is slightly out of plane, but the height was very small ($<$ 0.5mm) and beyond our super-resolution goal in the experimental demonstration. So the logo features were treated as noise, therefore were filtered out at the imaging processing workflow. The final results show the reconstructions with steps and disk shape mesas, but without the "LEGO" logos. The active illumination was from a Coherent$^{\text{TM}}$ Verdi-5 Nd:YAG laser operated at 532nm, focused to a line by a cylindrical lens of focal length 25mm. The CCD captured a holographic slit portion of the object with lateral size $\Delta x = 0.0532$mm.

Two multiplexed holograms recorded in a single $LiNbO_3$ crystal were used as VHI lenses in the experiment [11]. The two holograms were each focused to a different layer, the 3rd and 7th, respectively, separated in the depth direction by 6.4mm. This

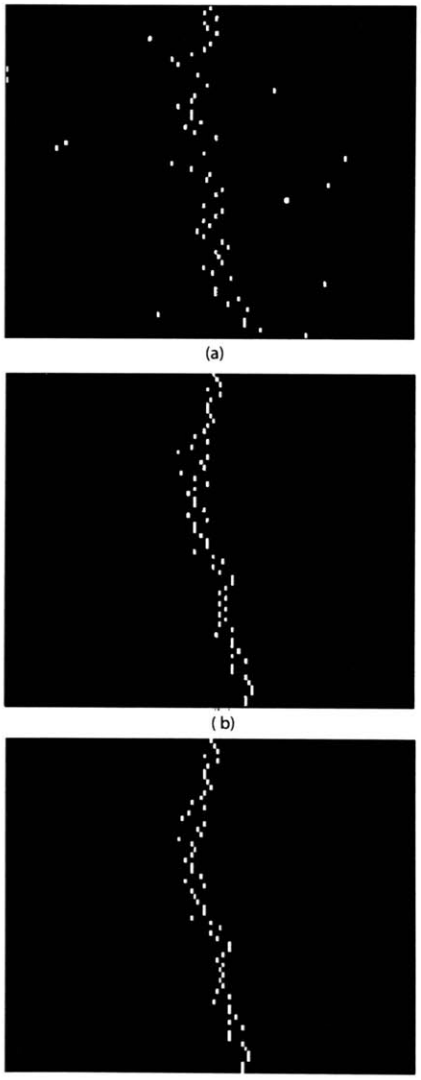

(a)

(b)

(c)

Figure 3-10: Reconstructed object surface by using (a) cross-correlation based peak finder algorithm, (b) RCVA (incoherent model) and RCVA (coherent model) with SNR=10.

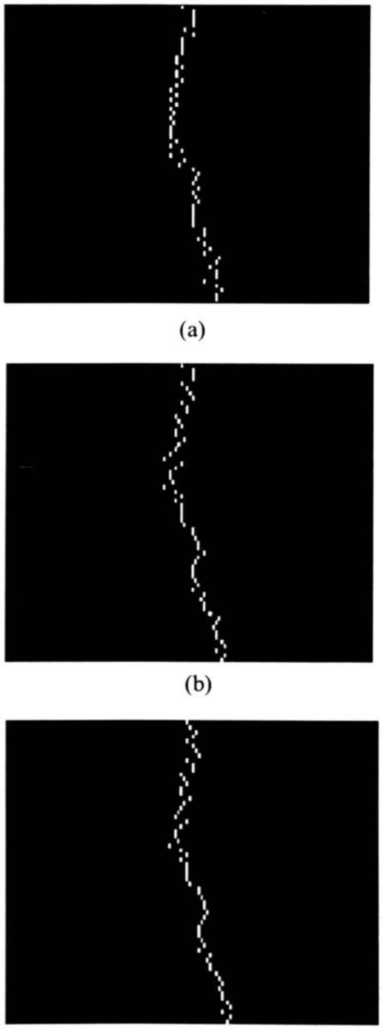

(a)

(b)

(c)

Figure 3-11: Reconstructed object surface by using (a) cross-correlation based peak finder algorithm, (b) RCVA (incoherent model) and RCVA (coherent model) with SNR=15.

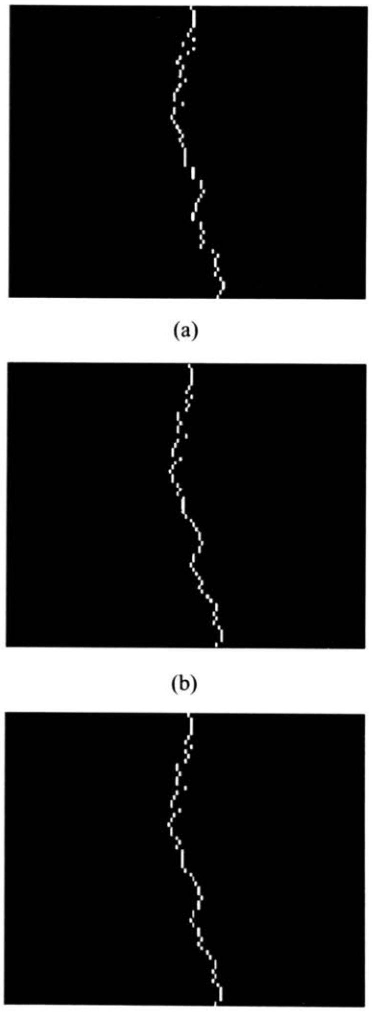

(a)

(b)

(c)

Figure 3-12: Reconstructed object surface by using (a) cross-correlation based peak finder algorithm, (b) RCVA (incoherent model) and RCVA (coherent model) with SNR=20.

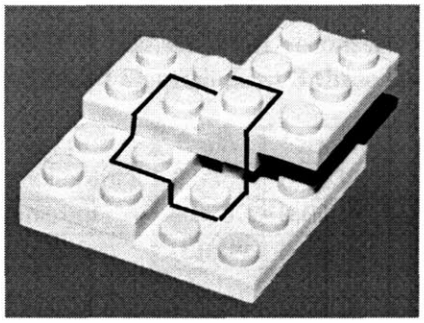

Figure 3-13: Lego^{TM} model used in VHI profilometry experiment. Area inside the black boundary was imaged.

separation is equivalent to four LEGO^{TM} layers, or one FWHM of the PSF. So at each measurement, two columns of the measurement matrix $I(m, n)$ were obtained (see Figure 3-14). These two columns were sufficient for the improved RVCA algorithm to recover the rest of the object, *i.e.*, to resolve all the eight depth layers in this longitudinal holographic slit. With lateral scanning driven by a Newport^{TM} CMA-25CC computer controlled motorize stage, images of the holographic slits over the entire object focusing on the 3rd and 7th layers were acquired. These slit-like images were then concatenated together to form the raw images of the LEGO^{TM} model, focusing on the 3rd and 7th layers.

To reduce the reconstruction error, the two holograms must have nearly identical PSF response. This was achieved in experiment by accurately controlling the exposure time when recording the holograms. Figure 3-15 shows the longitudinal PSFs of the two multiplexed holograms. For readers to easily compare the two PSFs, the two curves were shifted to overlap each other in the illustration. With lateral scanning at every step over the entire holographic slit width, and repeating the image registration and RVCA estimation, the object profile in every lateral holographic slit was restored. By concatenating different depths together, the LEGO^{TM} model was finally reconstructed with $\gamma = 4, \beta = 8$ (here multiplexing VH lenses increased the gain factor β from 4 to 8). We repeated the experiments at laser output powers of 25mW, 15mW, and 8mW to test the super-resolution performance at different SNR levels. Figure 3-16(a)-(f) show these raw images acquired at the three different laser illumination powers, with

Table 3.2: Comparison MRE of experimental reconstructed LEGO^{TM} model with RCVA and Cross-correlation based algorithms at 3 three laser illumination intensities.

Illumination power	8mW	15mW	25mW
RCVA(incoherent)	0.0349	0.0133	0
RCVA(coherent)	0.0737	0.0209	3.6×10^{-5}
Cross-correlation	0.1699	0.0479	0.0073

the LEGO^{TM} logo pattern filtered out. The peak finder algorithm was also used in these processing experiments. Reconstructed LEGO^{TM} models using the RCVA based method with both incoherent illumination model and coherent illumination model, as well as the correlation-based method at all three SNR levels are shown in Figures 3-17 through 3-19, respectively. The incoherent model RCVA method is not theoretically exact with reconstruction of a step-wise object as the LEGO^{TM} model used in this experiment as mentioned in Section 2. However, it is still interesting to compare the results from both formulations side-by-side. It can be seen from the reconstruction results that at a low noise level, all the methods can restore the original object with $e < 0.01$. If the processing model is exact, the RCVA method generates error-free reconstruction. As the laser illumination power was reduced, *i.e.*, at low SNR, more reconstruction error appeared in the results of all the methods. However, even at the lowest SNR, the RCVA is significantly more robust than the correlation peak finder method even if the processing model is not theoretically exact. Moreover, if the theoretically exact processing model is used, the RCVA outperforms the cross-correlation method even more. The MRE of all post-processing methods under the above-mentioned three laser illumination power levels is shown in Table 3.2.

3.4 Summary

To summarize this chapter, we first built a digital post-processing framework for improving the VHI profilometry raw images. The mathematical model for the VHI imaging channel was built. We demonstrated the use of the Viterbi algorithm to clean

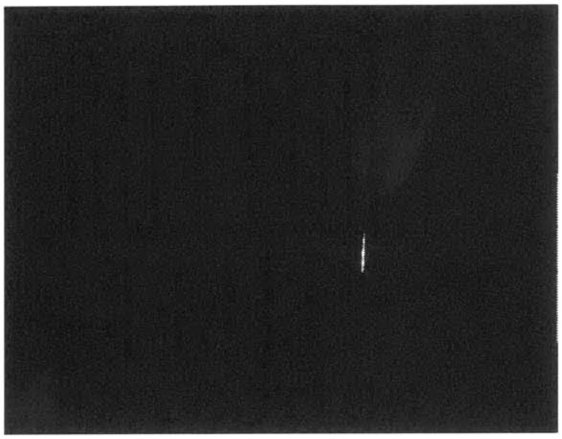

Figure 3-14: Two holographic slits were imaged by multiplexing two holographic lenses at a single measurement procedure.

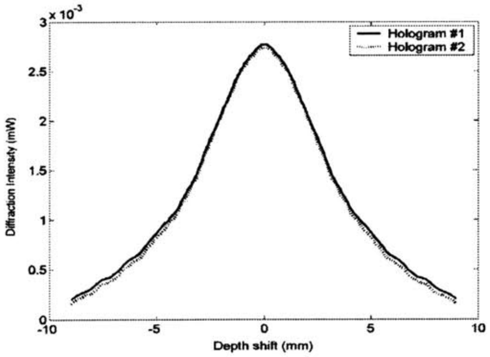

Figure 3-15: Longitudinal PSFs of the two multiplexed holographic lenses used in experiment.

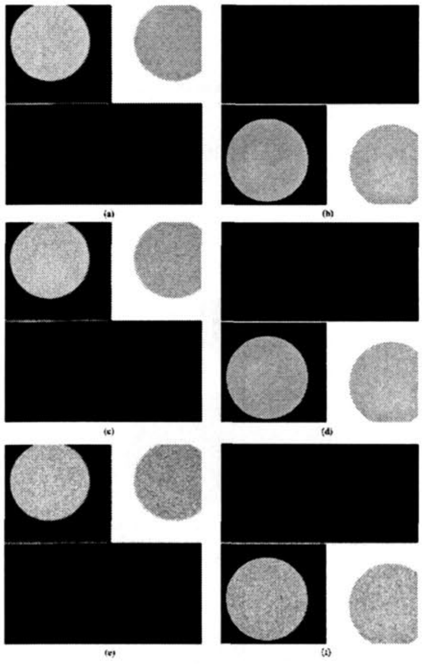
(a) (b) (c) (d) (e) (f)

Figure 3-16: Raw LEGO^{TM} images acquired by the VHI profilometer with (a) hologram #1 focused on the 3rd layer under illumination power of 25mW, (b) hologram #2 focused on the 7th layer under illumination power of 25mW, (c) hologram #1 focused on the 3rd layer under illumination power of 15mW, (d) hologram #2 focused on the 7th layer under illumination power of 15mW, (e) hologram #1 focused on the 3rd layer under illumination power of 8mW, (f) hologram #2 focused on the 7th layer under illumination power of 8mW.

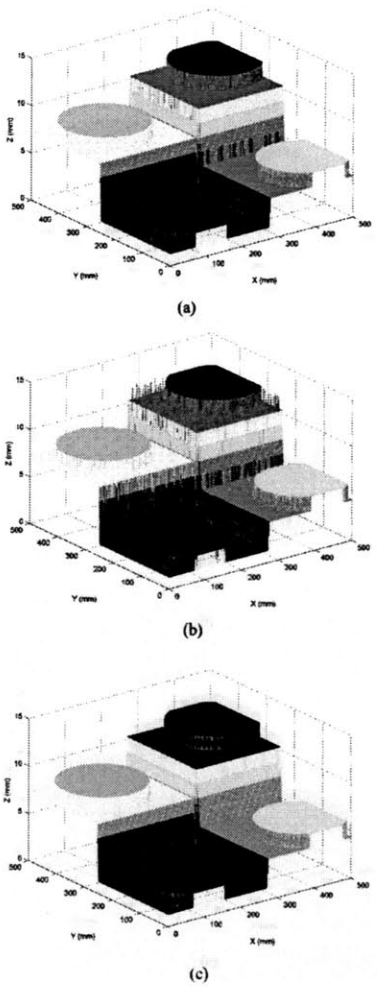

Figure 3-17: Reconstructed LEGO$^{\text{TM}}$ model with (a) RCVA with incoherent model, (b) cross-correlation based peak finder algorithm and (c) RCVA with coherent model under illumination power of 25mW.

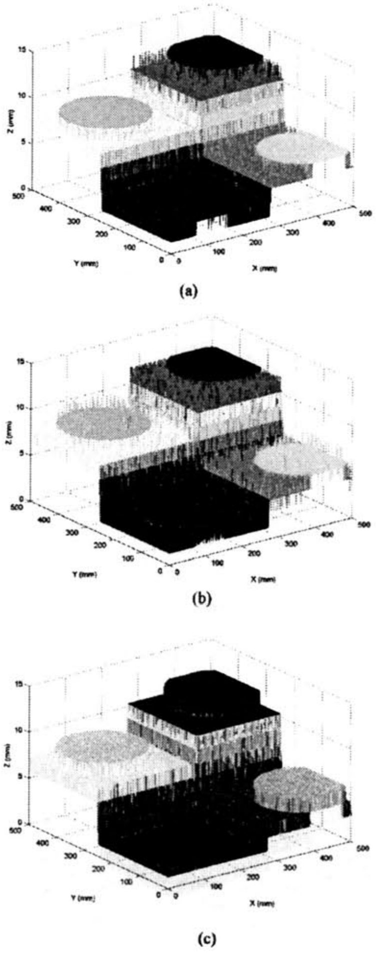

Figure 3-18: Reconstructed LEGO$^{\text{TM}}$ model with (a) RCVA with incoherent model, (b) cross-correlation based peak finder algorithm and (c) RCVA with coherent model under illumination power of 15mW.

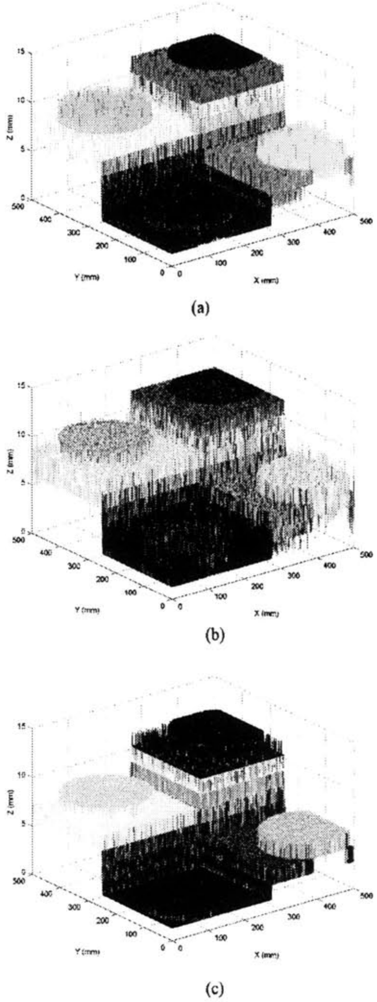

(a)

(b)

(c)

Figure 3-19: Reconstructed LEGO$^{\mathrm{TM}}$ model with (a) RCVA with incoherent model, (b) cross-correlation based peak finder algorithm and (c) RCVA with coherent model under illumination power of 8mW.

up VHI images for high resolution profilometry object reconstruction. We achieved a resolution gain factor of 5 in the depth dimension, without sacrificing the lateral resolution. The surface and transition constraints were exploited to dramatically reduce the computational complexity. We also modified the post-processing method to accomplish depth interpolation. The new method requires fewer experimental profilometry data (raw images.) Simulation and experimental results showed that the RCVA method generates reconstruction models with fewer errors than other commonly used interpolation methods. In experiment, with the help of multiplexing two holograms in a single $LiNbO_3$ crystal, we reconstructed a target object with eight different height levels via a single lateral scanning and image acquisition. Depth features as small as one-quarter of the nominal depth resolution of the VHI profilometer were resolved after post-processing.

Chapter 4

Rainbow and Hyperspectral imaging

4.1 Introduction

We have presented the monochromatically illuminated VHI profilometry system in Chapter 2 based on the optical behavior analysis of VH lens. So far the depth resolution improvement over long working distance is our major concern. In Chapters 2 and 3 we developed both optical methods and digital post-processing methods to improve the depth resolution over long working distance. Moreover, as seen in Section 3.3, by combining the digital post-processing and multiplexing of VH lenses, longitudinal scanning can be reduced or eliminated. However, line scanning across the object plane remains a problem to realize non-scan real-time imaging system because the FoV of the monochromatic VHI is limited to a slit. Actually, the trade-off between resolution and FoV exists in most 3D imaging techniques employing a pupil plane filter, such as confocal microscopic imaging. In confocal microscopic imaging, methods such as scanning the pinhole [54, 55] and using chromatic dispersion of white light source to focus the probe at multiple depths simultaneously [56, 57, 58, 59, 60, 61] are used to reduce scanning. In VHI systems, it has been demonstrated that the wavelength degeneracy of the VH lens can be used to extend the FoV using broadband illumination [45, 62]. However, it has been shown in Ref. [63] that directly using broadband illumination to expand the FoV in VHI results in losing depth resolution drastically. In this Chapter, we propose a rainbow illumination scheme to address this problem. Through rainbow illumination the FoV is effectively expanded, while the depth resolution of the imaging system remains with little degradation. In section 4.2, we first revisit the VH lens wavelength degeneracy property using an alternative approach, the *K-sphere* diagram to form the basis for rainbow illumination system design. Then we present the non-scan rainbow illumination VHI design that exploits this wavelength degeneracy property. We will also address the derivation of the rainbow illumination VHI depth selectivity and PSF in this section. Based on the rainbow illumination VHI design, a hyper-spectral VHI system is proposed in 4.3. The hyper-spectral VHI can capture not only the 3D spatial information of the object but also the spectral information, under a focused line broad band illumination.

4.2 Rainbow volume holographic imaging

In Section 2.1.3, we introduced the wavelength degeneracy of the VH lens. It was found that when the probe point source shifts off from the reference position, the VH lens usually will be Bragg-mismatched. However, by tuning the wavelength of the point source according to Eq.(2.25), Bragg-matching can be re-obtained.

Wavelength degeneracy can be best understood using the *K-sphere*, as shown in Figure 4-1. Suppose the VH lens is recorded by two mutually coherent green plane waves. The VH lens grating vector is $\mathbf{K}_G$ pointing from the tip of the reference wave vector $\mathbf{K}_F$ to the tip of the signal wave vector $\mathbf{K}_S$. When the VH lens is readout by probe beam with different wavelength, the diameter of the *K-sphere* changes. However, the length of the VH lens grating vector $\mathbf{K}_G$ remains the same. To Bragg-match the VH lens, the incident angle has to be changed to match the translated VH lens grating vector translated onto the new *K-sphere*. Figure 4-1 shows how a red and a blue probe plane wave can Bragg-match the VH lens. The diffraction angle changes correspondingly. For a VHI setup as shown in Figure 2-3, assume the VH lens is pre-recorded with 532nm Nd:YAG laser and $\theta_s = 30^o$ signal beam angle. Because of the angular degeneracy, we know that a 532nm line source anywhere along the the y axis can Bragg-match the VH lens. Furthermore, because of the wavelength degeneracy, line sources with simultaneous x shift and wavelength shift may also Bragg-match the VH lens. The relation between the x shift and wavelength shift can be derived from the *K-Sphere* as

$$\frac{\Delta\lambda}{\lambda} \approx -\frac{\theta_s}{2} \cdot \frac{\Delta x}{f}, \tag{4.1}$$

where λ is the recording wavelength, $\Delta\lambda$ and Δx are the wavelength shift and lateral shift in the x direction of the probe light from the original recording conditions, respectively. θ_s and f are the recording signal beam angle and the focal length of the objective lens L_1 (see Figure 2-3), respectively. This equation holds in paraxial range only.

By substituting $\theta_s = x_s/f$, one can find that Eq.(4.1) agrees with (2.25).

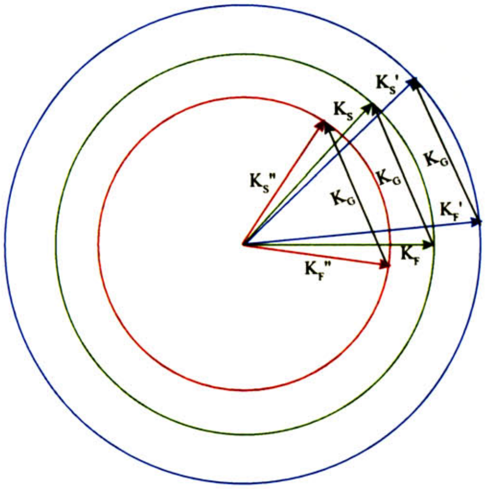

Figure 4-1: *K-sphere* illustration of VH lens wavelength degneracy, $\mathbf{K}_G$ is the VH lens grating vector. $\mathbf{K}_S$ and $\mathbf{K}_F$ are the recording signal and reference wave vectors. $\mathbf{K}'_S$ and $\mathbf{K}'_F$ denote the probe with shorter wavelength, and $\mathbf{K}''_S$ and $\mathbf{K}''_F$ denote the probe with longer wavelength.

An experimental setup which demonstrated the wavelength degeneracy is shown in Figure 4-2(a). The VH lens was pre-recorded with a Coherent$^{\text{TM}}$ 532nm Nd:YAG laser. The recording angle θ_s between the signal beam and reference beamwas 30^o (outside the hologram), and the reference beam was normally incident. The Nd:YAG laser and another 632.8nm He:Ne laser were used to probe the VH lens by focusing to two point sources at the front focal plane of the objective lens. The parameters of the experiment were as follows: The numerical aperture of the objective lens was 0.07, focal length of objective lens was 50.2mm, and the thickness of the hologram was 2mm. The location of the He:Ne laser point source was shifted laterally at the front focal plane of the objective lens by 36mm, according to Eq.(4.1). Figure 4-2(b) shows the diffracted image captured with a CCD camera. It can be seen clearly that the two probe sources are both Bragg-matched with the VH lens, resulting in two well separated bright spots. The principle of wavelength degeneracy can be used to expand the FoV of a VHI system. Assume the object plane is not illuminated by a discrete number of sources with different wavelengths as described above, but a continuous spectrum of line sources with wavelength from λ_1 to λ_2, spread out over the object plane, like a rainbow. The lateral location and the wavelength of an arbitrary spectrum line in this rainbow satisfies Eq (4.1). Then the entire front focal plane is illuminated by a rainbow-like source, and can Bragg-match the VH lens simultaneously. Therefore, if the object is placed in the vicinity of the front focal plane of the objective lens, the FoV is expanded to the size of the rainbow, whereas

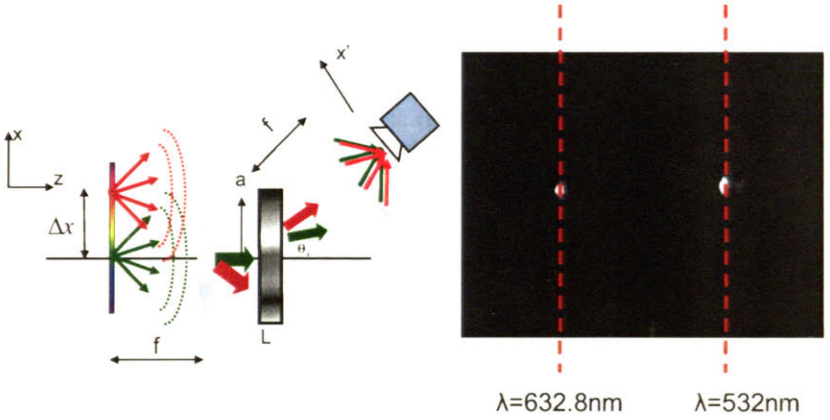

(a) (b)

Figure 4-2: (a)Experimental setup of the wavelength degeneracy experiment; (b)diffraction of both probe sources with different wavelength imaged onto CCD camera.

with the monochromatic illumination, the FoV is limited to a narrow slit. Moreover, each quasi-monochromatic spectrum line within the rainbow probes the VH lens the same way as the monochromatic laser does, so the depth selectivity of the VH imaging system is preserved.

4.2.1 Rainbow volume holographic imaging system principle

An experimental setup to implement this rainbow VHI is shown in Figure 4-3. The illumination part consists of a collimated white light source, a diffraction grating to disperse it, and an achromatic cylindrical lens (focal length f_c) which focuses each color into a sharp strip. The color strips are oriented in the y dimension, as shown in Figure 4-3. The object is placed in the vicinity of the focal plane of the cylindrical lens. The reflected light from the object is first directed to an objective lens (focal length f_o), and then diffracted by the VH lens. A digital camera is placed on the diffraction path, at the back focal plane of the Fourier lens (focal length f_F). This schematic

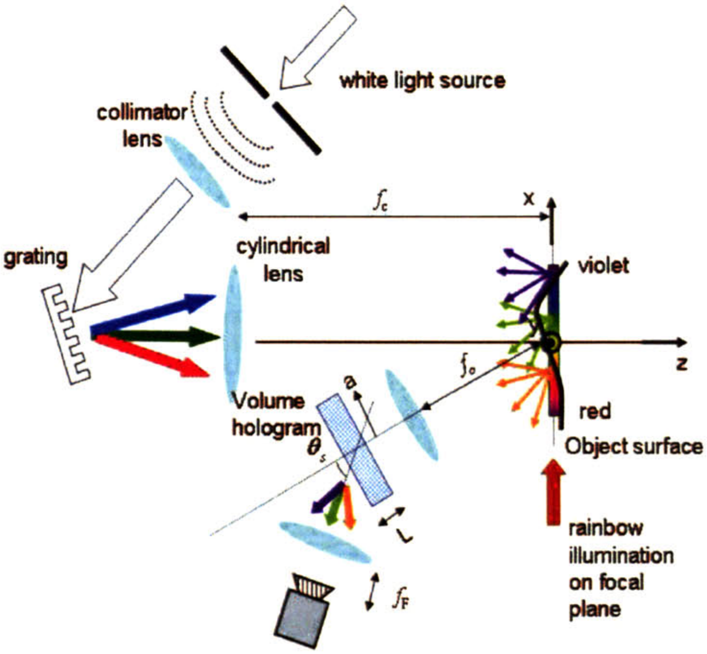

Figure 4-3: Illustration of rainbow volume holographic imaging system.

shows the setup for imaging a reflective system. A semi-transparent diffusive object can also be imaged with the rainbow VHI systems, however, with the VH lens imaging part located at the opposite side of the rainbow illumination part, with respect to the object. Consider a quasi-monochromatic strip within the rainbow projected onto the object in this arrangement. The portions of the object surface which are out-of-focus of the quasi-monochromatic illumination strip will be Bragg-mismatched, thus photons originated from there will not reach the camera. On the other hand, the in-focus portions of the object surface are Bragg-matched so that they can be imaged. As we know, this happens simultaneously for all quasi-monochromatic strips if Eq.(4.1) is satisfied. In the rainbow VHI setup, the lateral spread-out of the quasi-monochromatic strips is determined by the grating period Λ of the thin grating used to analyze the white light. Consequently, derived from grating equation and Eq.(4.1), the Bragg-matching condition for rainbow volume holographic imaging is

$$\frac{f_c}{\Lambda} \approx -\frac{\theta_s f_o}{2\bar{\lambda}}, \tag{4.2}$$

where $\bar{\lambda}$ is the recording wavelength of the VH lens. With this arrangement, we obtain depth-selective images simultaneously over the entire illuminated surface, *i.e.*, from each color in the rainbow. Scanning along z is still necessary to recover the full object shape. The field of view FoV_x along the x dimension is only limited by the size of the CCD camera, or the bandwidth B of the rainbow. Assuming the latter is the limiting factor, then the $\mathrm{FoV_x}$ is given by

$$\mathrm{FoV_x} = \frac{B\theta_s}{\bar{\lambda}}(rad). \tag{4.3}$$

4.2.2 Rainbow volume holographic imaging system point spread function and depth selectivity

As described before, one can understand the rainbow VHI system as a parallelized multi-channel laser illumination VHI system. The rainbow illumination can be imagined as an infinite number of quasi-monochromatic illumination strips stitched together. Each quasi-monochromatic illumination strip defines an imaging slit, and these imaging slits work independently. Therefore it is straightforward to see that the depth selectivity of an arbitrary quasi-monochromatic imaging slit should be the same as a monochromatic laser illumination VHI system, given that these two systems use the same objective and VH lenses, as well as the working wavelength and lateral position of the the monochromatic VHI are the same as that of the corresponding quasi-monochromatic strip of the rainbow VHI system. Assume that the depth selectivity is defined as the full width at half maximum (FWHM) of the longitudinal PSF. The FWHM is obtained from the three-dimensional diffraction theory in Ref. [17] and it is given, approximately, by

$$\Delta z_{FWHM} = G(\lambda)\frac{\lambda f_o^2}{\theta_s a L}, \tag{4.4}$$

where a is the hologram aperture radius, L is the hologram thickness, and $G(\lambda)$ is a wavelength-dependent coefficient calculated numerically and shown in Figure 4-4. At λ=532nm, G=5.34 in agreement with Ref. [17].

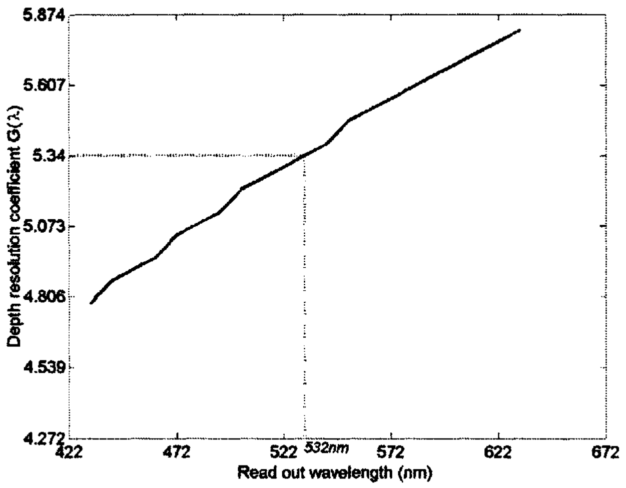

Figure 4-4: $G(\lambda)$ dependence on probe wavelength.

We implemented an experiment to verify this prediction. A CUDA$^{\text{TM}}$ halogen lamp with B=400nm-650nm was used as the white light source. The rainbow was projected to the object plane using a blazed grating with spatial frequency $1/\Lambda$=600 lp/mm and a cylindrical lens with f_c=25mm. Two achromatic spherical lenses were used as objective and Fourier lenses. The volume hologram had thickness L=0.2mm and signal beam angle $\theta_s = 30^o$, and was pre-recorded by Ondax, Inc. A wide spectrum Newport^{TM} 2832-C optical power meter were placed at the imaging plane to collected all the diffracted radiation over the entire rainbow spectrum. The objective lens, fourier lens, VH lens and powermeter was mounted on a bread board and translated through a computer control translation stage, moving along z direction. The measured superimposed longitudinal PSFs is shown in Figure 4-5. Rainbow VHI can also be set with optical axis inclined with respected to the object surface to improve profilometry depth resolution [44]. The PSF of a 30^o inclined system is shown in Figure 4-5. It can be seen that the integrated diffracted power of Rainbow VHI drops off

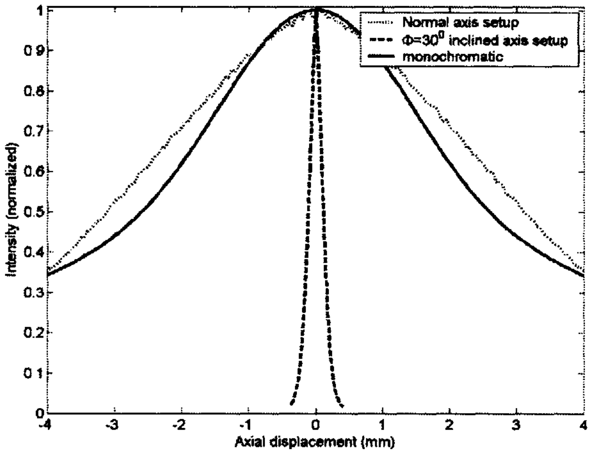

Figure 4-5: Experimental measurement of the integral diffracted intensity varying as the rainbow VHI shifted off focus.

slightly slower than its monochromatic laser illumination VHI counterpart, as to the same defocus shift. This is because of the following reasons:

1. The dispersion grating and the cylindrical lens used to generate the rainbow have limited resolution. Therefore, each quasi-monochromatic strip on the object plane consists of wider range of wavelength components than the laser

system. This color blurring cause the degradation of depth selectivity;

2. Besides the color blurring at the on-focus object plane described above, when the object is out-of-focus, the quasi-monochromatic strips partially overlap with each other because of the defocus blur of the cylindrical lens. Therefore, at an arbitrary lateral position on the object, the bandwidth of the corresponding quasi-monochromatic strip expands due to the color blur. This bandwidth expanding causes more ambiguity in VH lens Bragg selection. Consequently, for Rainbow VHI, when object is defocused, the degree of Bragg-mismatch is less than laser illumination system.

To quantitatively analyze the imaging property of the rainbow VHI, we derive the PSF using the similar approach as used in [11] for the scanning microscope. The similarity is that they both consist of an illumination part and an imaging part. The PSF, under the assumption of incoherent illumination, which is the case in rainbow VHI system, can be written as the product of the incoherent PSFs of the illumination part and that of the imaging part as

$$I\left(x,y,\delta\right)=\left|h_I\left(x,y,\delta\right)\right|^2\cdot\left|h_H\left(x,y,\delta\right)\right|^2, \tag{4.5}$$

where x, y are the lateral coordinates of the object plane and δ is the defocus.
The physical meaning of this incoherent PSF $I\left(x,y,\delta\right)$ is the diffracted intensity distribution on the CCD camera plane when an infinite small point object is placed in the vicinity of the object plane, at the position (x,y,δ). Firstly, let us consider the first effect described above. The limited resolution power of the dispersion grating and the limited aperture of the grating and the cylindrical lens cause a finite extent of the illumination PSF $\left|h_I\left(x,y,\delta\right)\right|^2$ and the degradation of the color purity of the rainbow. The PSF of the illumination system can be numerically calculated by the Fresnel integral. Figure 4-6 shows a simulation result with the following optical parameters: $\delta=0.25$mm, f_c=50mm and the grating size 10mm × 10mm, with grating constant 300lp/mm and blazed at 60^o, 532nm. The imaging part PSF $\left|h_H\left(x,y,\delta\right)\right|^2$ can be numerically calculated with the 3D diffraction framework presented in Chapter

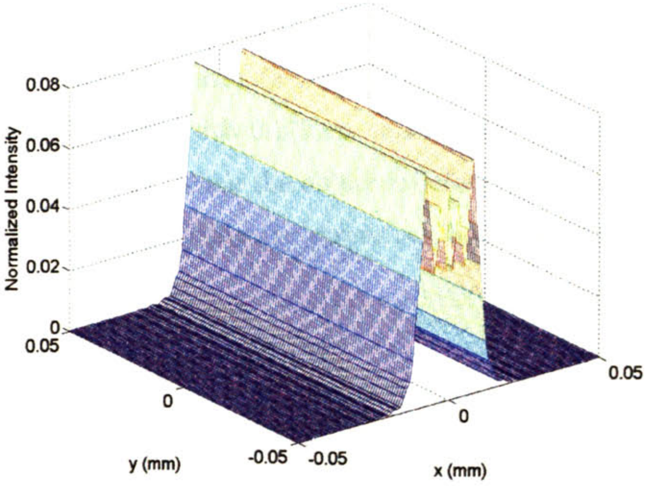

Figure 4-6: Simulated PSF of the illumintaion part of a rainbwo VHI shown as Figure 4-3 at an out-of-focus plane with defocus of δ =0.25mm. The PSF of single wavelength λ=532nm is shown here.

2. Therefore, the complete rainbow VHI PSF corresponding to a single wavelength λ=532nm can be calculated and shown in Figure 4-8 (b) and (d).

However, as described previously, the rainbow VHI is a polychromatic imaging device. Therefore, no matter where the testing point object is located on the object plane, it possesses finite bandwidth because the resolution power of the dispersion grating is limited. Moreover, when the testing point object is shifted out of the object plane, the bandwidth of the light reflected from it increases because the rainbow is blurred at out-of-focus planes.

Let us estimate the bandwidth of the testing point object due to the limited dispersion grating resolution as follows. The resolution power in wavelength of the rainbow is

$$\Delta\lambda_{FWHM} = \frac{\lambda}{N}, \tag{4.6}$$

where N is the total number of the groves of the grating. Substituting into the parameters used above, the bandwidth of the testing point object on the in-focus object plane is 0.177nm.

This defocus color blur when the testing point object is moved out of the object plane can also be calculated numerically with simple diffraction calculation. Figure 4-7 shows the calculated spectrum of the testing object with defocus of $\delta = 0.25$mm. It can be seen that the bandwidth (FWHM) is expanded to around 20nm, which is much more than the bandwidth 0.177nm caused by the resolution power of the dispersion grating. Therefore, when the object is defocused, the bandwidth widening caused by the limited grating dispersion power can be neglected.

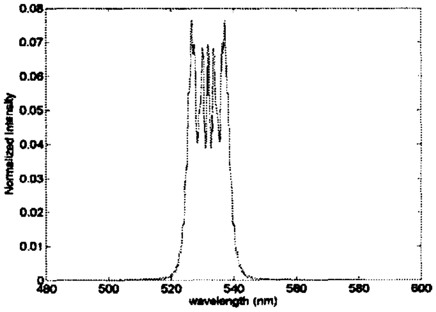

Figure 4-7: Spectrum broadening of the infinite small testing object due to the defocus.

The PSF of the VHI part can be numerically simulated with the 3D diffraction formulation introduced in Chapter 2. Then the PSF of the complete rainbow VHI at a specific wavelength can be calculated as Eq. (4.5). The bandwidth broadening is taken account by calculating rainbow VHI PSFs at each wavelength within the entire broadened testing object bandwidth and adding them incoherently, weighted by the spectrum of the defocused testing object as shown in Figure 4-7. Following this strategy, PSF of the rainbow VHI system (with the same optical parameters as mentioned above) with defocus $\delta = 0.25mm$ was calculated and shown in Figure 4-8(a). Figure 4-8(b) shows the PSF with the same defocus of a monochromatic VHI system with the same optical parameters. The ripples along x direction in monochromatic PSF are from the defocused cylindrical lens illumination pattern, as shown in Figure 4-6. In the rainbow VHI case, only the central wavelength is perfectly Bragg-matched to the VH lens given the position of the infinite small testing object. The other wavelengths are Bragg-mismatched at various degree due to the wavelength deviation from the center, so that the diffractions corresponding to these wavelengths are attenuated accordingly. Each of these diffracted fields corresponding to the shifted wavelength is shifted laterally on the camera plane. This can be found with the *K-sphere* in Figure 4-1. Thus, when all these diffraction patterns corresponding to various wavelengths within the broadened testing object bandwidth are added up together incoherently, the vertical ripples that appear in monochromatic PSF are smeared. The lateral size of the PSF in the x direction is also expanded due to the testing object bandwidth broadening. Figure 4-8(c) and (d) show the monochromatic PSF and rainbow PSF in 3D, respectively. The intensity is normalized to the peak intensity of the in-focus response. The higher intensity and the wider extent of the PSF in rainbow VHI contribute the slower defocus rejection shown in Figure 4-5.

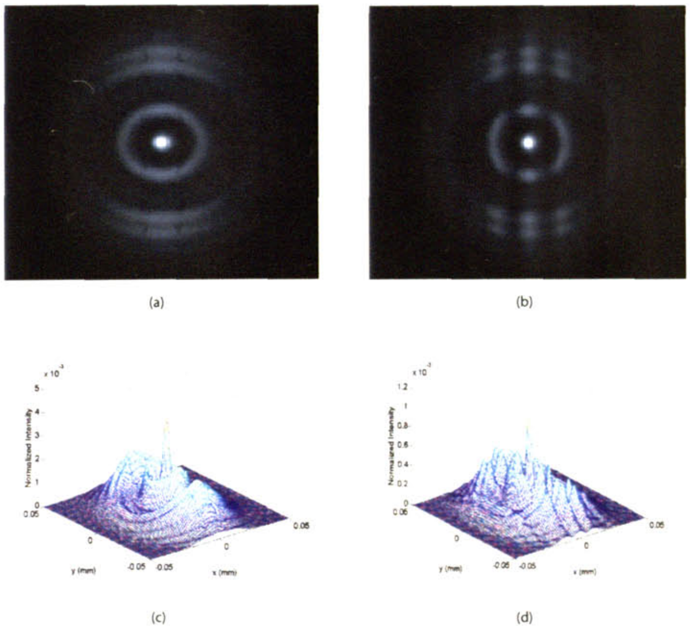

Figure 4-8: Image plane defocused diffraction distrubtions of (a), (c) rainbow illuminated VHI and (b),(d) monochromatic line illumination VHI.

4.2.3 Imaging experiment results

We used the same experimental setup to demonstrate image acquisition with rainbow VHI as shown in Figure 4-3. A Newport$^{\text{TM}}$ CMA-25CCCL actuator was used for longitudinal scanning, and a monochrome 752 × 480 pixel JAI$^{\text{TM}}$ CCD camera was used to acquire the raw images. Figure 4-9(a) shows a micro-fabricated micro turbine with approximately 250μm feature depth and 9mm diameter, illuminated by the rainbow. Figures 4-9(b) and 4-9(c) show the raw images acquired by rainbow VHI at two different longitudinal positions, separated by 250μm, with inclined illumination at $\phi = 30^o$ to improve depth resolution [44]. The effective FoV provided by the rainbow was approximately 15^o, according to Eq.(4.3), and was bigger than the object window. Figure 4-9(d) shows the reconstructed shape of the micro-turbine from a total of N=8 raw images. Note that the object had only two depth levels, but $N > 2$ was necessary because the illumination was inclined. Imaging experiments were also implemented with another micro object, the nano-gate used in a MEMS pump assembly to control liquid flow. Figure 4-10 (a), (b), (c) and (d) show the regular microscopic image of the nanogate, the rainbow VHI image of nanogate at the top layer, the bottom layer, and the three dimensional reconstructed nanogate profile, respectively.

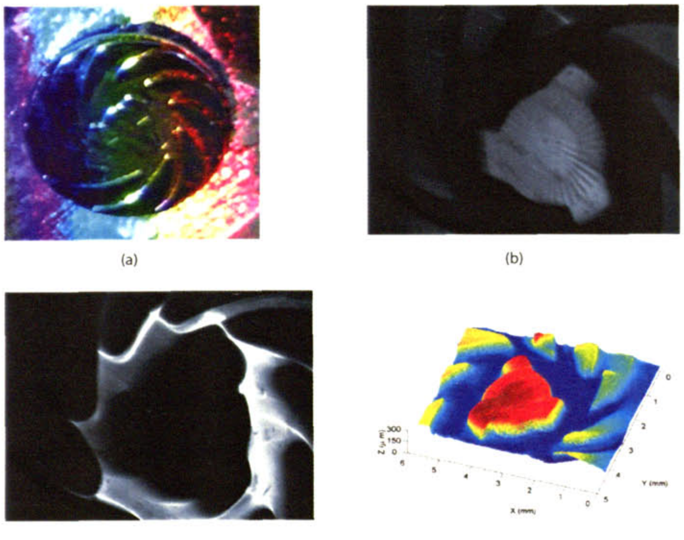

(a) (b) (c) (d)

Figure 4-9: Microturbine image acquisition using Rainbow VHI: (a) microturbine illuminated with a rainbow; (b), (c) raw images showing depth selectivity across the rainbow field; (d) shape reconstruction from four depth-selective raw images.

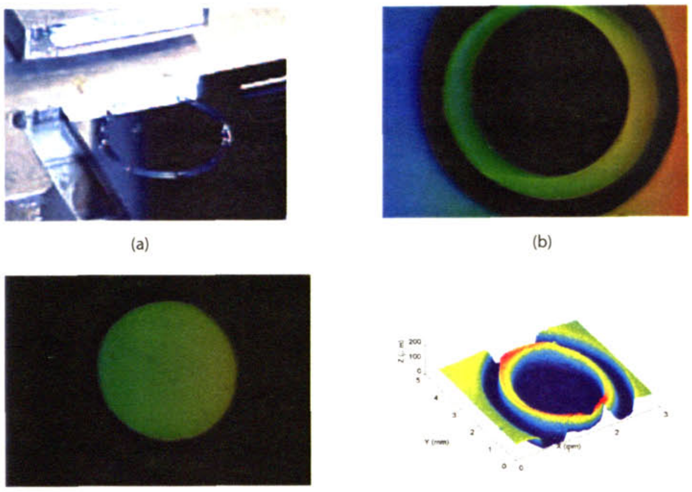

(a)

(b)

(c)

(d)

Figure 4-10: Nanogate image acquisition using Rainbow VHI: (a) Nanogate; (b), (c) raw images showing depth selectivity across the rainbow field; (d) shape reconstruction from four depth-selective raw images.

4.3 Hyper-spectral volume holographic imaging

The Rainbow VHI principle can be used not only to enlarge the FoV so as to reduce or eliminate scanning, but also to achieve hyper-spectral imaging ability. We recently have devised a high resolution hyper-spectral imaging system based on it. This hyper-spectral VHI system works similarly to a spectrograph but with two major differences:

1. The hyper-spectral VHI system has depth discrimination, *i.e.*, it is able to do optical sectioning in both spatial depth dimension as well as the spectral dimension.

2. The hyper-spectral VHI system is an "imaging" device, *i.e.*, it generates point-to-point spatial relations between entrance-window and exit-window planes. This can be best understood with the following example. Imagine there is a broadband line source at the entrance window. Then, at the exit window, the spectrum of this broadband source is fanned out with different colors mapped to different lateral positions. For a conventional spectrograph, if half of the line source is blocked out, one will see the image remains the same but inten-

sity is attenuated, corresponding to size of the object is blocked. However, for the hyper-spectral VHI, half of the output spectrum disappears as half of the source is blocked, because the hyper-spectral VHI focuses the source radiation at the output plane, so that the image shape forms point-to-point relations to the source.

4.3.1 Schematic and imaging principle

The schematic of the hyper-spectral VHI system is shown in Figure 4-11. In the figure, a white light line perpendicular to the paper is used for illumination. This illumination can be generated by focusing radiation from a quartz halogen lamp or other broadband source through a cylindrical lens.

The hyper-spectral imaging system consists of two $4F$ systems as shown in Figure 4-11. The first $4F$ system is commonly seen in a spectrometer or monochromator. The object is illuminated by the slit-like line white light source. The reflected radiation firstly enters a collimation lens L_1 with focal length f_1. A transmissive holographic blazed grating G_1 is placed at the back focal plane of L_1. Because light incident onto the holographic blazed grating is pre-collimated by L_1, the ±1st order diffraction separates the spectrum components of the source into multiple plane waves at slightly different propagation directions. Here we would like to point out that in Figure 4-11 the ±1st order is drawn along the axial direction for simplicity. This is not true in reality. Lens L_2 collects all these diffracted plane waves and refocuses them onto its back focal plane. Therefore, a rainbow corresponding to the spectrum of the line source is formed at this plane, named the spectral plane. The spectral plane is also the input plane to the second $4F$ system, which is actually the rainbow VHI system discussed before.

The lateral spread out $\lambda(x)$ of the rainbow on the spectral plane is controlled by the the focal length of L_2 and the grating constant of the holographic grating G_1. If $\lambda(x)$

is set by choosing the appropriate parameters of L_2 and G_1 such that

$$\frac{d\lambda}{dx} = -\frac{\lambda}{2\theta_s f_3}, \tag{4.7}$$

where θ_s is the recording signal beam angle of the holographic lens G_2 and f_3 is the focal length of rainbow VHI objective lens L_3, the entire spectrum from the illuminated line of the object is then Bragg-matched to the VH lens G_2. Thus, an image of this rainbow spectrum is formed onto the CCD/CMOS imager similar to conventional "imaging spectrograph." Please note here the entire illumination line perpendicular to the $x - z$ plane can be imaged because of the angular degeneracy of the VH lens along y direction. However, if the illumination line is not at center, *i.e.*, on the $x \neq 0$, the "spectrograph" sub-system forms a laterally shifted rainbow at the spectral plane. Obviously, this shifted rainbow does not satisfy Eq.(4.7), thus Bragg-mismatched to the VH lens, and consequently rejected by the rainbow VHI sub-system.

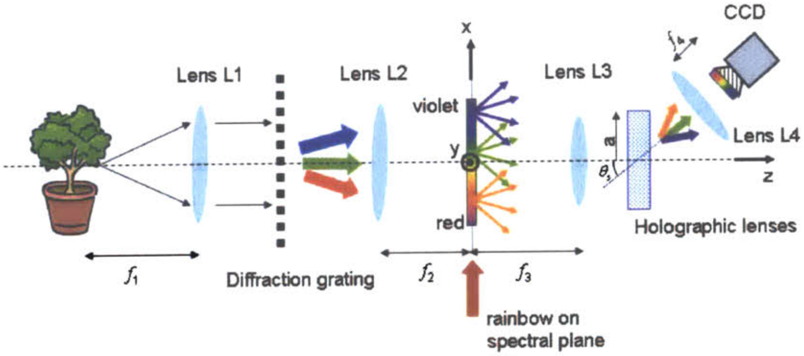

Figure 4-11: Illustration of hyper-spectral VHI system based on double 4F system design.

If the object is defocused, the "spectrograph" sub-system forms the corresponding "rainbow" no longer at the original spectral plane but slightly in front of or behind it. As described in Section 4.2, the rainbow VHI sub-system then rejects this defocused rainbow. Following Eq.(4.4), the depth selectivity of a hyper-spectral VHI system is still given by

$$\Delta z_{FWHM} = G(\lambda)\frac{\lambda}{aL}f_3^2, \tag{4.8}$$

where a and L are the aperture radius and thickness of the VH lens. $G(\lambda)$ is the coefficient which depends weakly on λ as shown in Figure 4-4, carried out through numerical simulation. We note that from both coefficient $G(\lambda)$ and Eq. 4.8 itself, Δz_{FWHM} increases with wavelength. This depth selectivity variation over spectrum can be compensated in post-processing.

4.3.2 4D optical sectioning and configuration modifications

From the discussion above, the imaging principle of the hyper-spectral VHI system can be understood as a non-invasive optical sectioning device working in 4D domain (three spatial dimensions + spectral dimension.) This hyper-spectral VHI system extracts a two dimensional plane from the 4D object space and maps it onto the detector plane [64]. For example, considering the system shown in Figure 4-11, the extracted 2D plane consists of the y dimension and the spectral dimension. The spectral dimension is mapped to the horizontal coordinate x' of the detector plane through $\lambda(x)$ and geometrical optics relation $x' = x \cdot f_3/f_4$. To cover the entire 4D object space, auxiliary scanning or multiplexing holographic lenses which Bragg match multiple 2D object sections are necessary. In the system shown in 4-11, the x and z dimensions need to be covered by scanning and/or multiplexing. As discussed before, illumination lines with lateral shift $x \neq 0$ form rainbows at the spectral plane of the hyper-spectral VHI system with corresponding lateral shift of $f_2/f_1 x$. However, the rainbow spread out relation $x(\lambda)$ remains unchanged. Therefore, by rotating the VH lenses with an angle $\frac{f_2 x}{f_1 f_3}$ one can bring the shifted rainbow back to the Bragg-matching condition, and form spectrographic image of the on-focus but laterally shifted object strip onto CCD/CMOS imager. This scanning can be easily implemented by placing the VH lens on a high speed rotation stage rotating around the y axis. Multiplexing multiple holographic lenses Bragg-matching multiple different depths simultaneously can reduce or eliminate depth scanning along z direction [45, 49].

We note that in the double $4F$ configuration shown in Figure 4-11, the explicit spectral plane allows easy implementation of additional spectral processing and/or filtering by placing various spectral filters and/or modulators at this plane. However, in case of a hyper-spectral profilometry system, no intermediate optical spectral processing is necessary and the system configuration can be simplified as shown in Figure 4-12, where the two intermediate lenses L_2 and L_3 are removed. In this configuration, the VH lens is recorded as the configuration shown as Figure 2-1(a) with a 532nm Nd:YAG laser, thus, the Bragg-matching angle for readout plane waves with wavelength $\lambda >$ 532nm is negative with respected to the normal direction of the VH lens surface. Therefore, only the -1 order diffraction from the dispersion grating can be used.

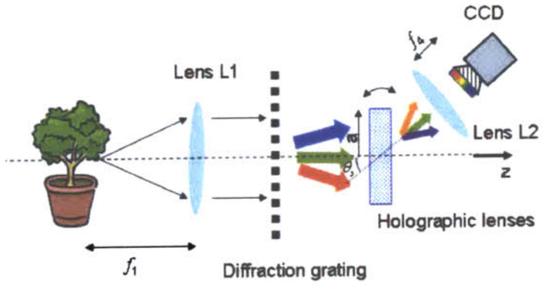

Figure 4-12: Illustration of simplified Hyper-spectral VHI.

4.3.3 Experimental results

A hyper-spectral VHI experiment was set up exactly according to the simplified configuration shown in Figure 4-12. The object was placed at a working distance of 50mm away from the achromatic objective lens $L1$ with focal length of 50mm. The target object was a plane mirror masked with black paper forming an "M" shape, as shown in Figure 4-14. The VH lens was a $LiNbO_3$ crystal pre-recorded with the interference of two plane waves. The reference beam was incident normally to the crystal and the signal beam was set with 30^o incident angel. The radius and the thickness of the crystal was 15mm and 2mm, respectively. The VH lens was mounted on a Newport$^{\mathrm{TM}}$ 495CC rotation stage, and controlled by a computer through LabView$^{\mathrm{TM}}$. This rotation was used to implement the x direction scanning. Illumination was provided by a CUDA^{TM} halogen lamp, focusing to a line through a cylindrical lens with focal length of 50mm. The emission spectrum of the CUDA^{TM} halogen lamp was measured with an OceanOptics^{TM} USB spectrometer as shown in Figure 4-13. The illumination optics was placed on an rotation stage synchronized with the x scanning stage to scan the illumination line. At each scanning position, spectrograph of the Bragg-matched slit was imaged onto the CCD/CMOS detector array. The entire object plane is then covered by the scanning mechanism. Figure 4-15 shows the spectral images of the Bragg matched slits at different lateral scanning positions of the object. It can be seen clearly that the extent of these images along the y direction matches the height of the illumination line intersected with the "M" shape mask. This showed the spatial point-to-point imaging relation between the object slit and the spectrograph image formed by the hyper-spectral VHI system. These spectral images can be synthesized to form an 4D hyper-spectral image of the "M" object. In this experiment, the object we chose is actually flat(2D), so the synthesized hyper-spectral image reduced to 3D. Therefore, it can be plotted as shown in Figure 4-16. The x and y axes correspond to the two lateral dimensions of the object. The z axis denotes the wavelength or the spectral dimension. One can understand it by noting all the raw spectral images captured by the hyper-spectral VHI system are actually 2D slices extracted at different x positions from this 3D synthesized image. For a real 3D object,

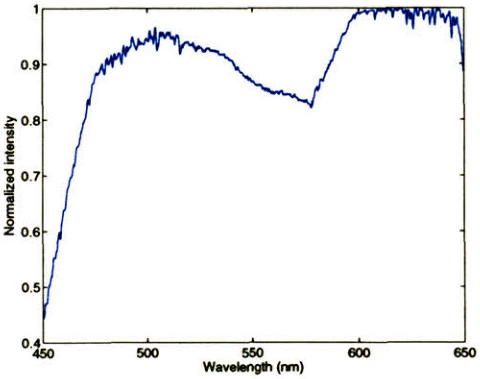

Figure 4-13: Spectrum of the broadband illumination source.

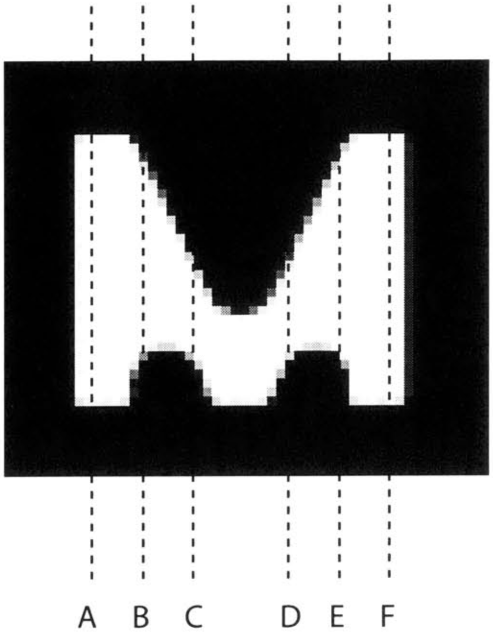

Figure 4-14: Illustration of the object used in hyper-spectral VHI experiments.

the circumstances becomes more complicated because the synthesized hyper-spectral image will be 4D and not easy to plot. However, what remains unchanged is that the hyper-spectral VHI system extracts two dimensional $y-\lambda$ slices and maps them onto the CCD/CMOS camera plane. Lateral x direction scanning is still accomplished by rotating the VH lens and illumination line. Depth direction (z) scanning requires additional translation of either the object or the hyper-spectral VHI system itself. Once the multi-dimensional hyper-spectral image is synthesized, it can be analyzed in multiple ways. A more intuitive alternative approach allows us to extract the 2D images at a specific depth and a specific wavelength band. For example, the images of "M" at λ = 480nm, 540nm and 630nm were extracted and are shown in Figure 4-17(a, b, c). It can be seen that because the object "M" is made of a metallic reflective mirror and the reflectance is nearly uniform over the entire visible band, the images at all three wavelength bands are nearly identical. We painted the "M" to red and blue with highlight markers and repeated the experiments. The images of "M" at $\lambda = 480$nm and 630nm are shown in 4-18(a, b). When the mirror was coated with red marker, the reflectance in blue wavelength was attenuated. Consequently,

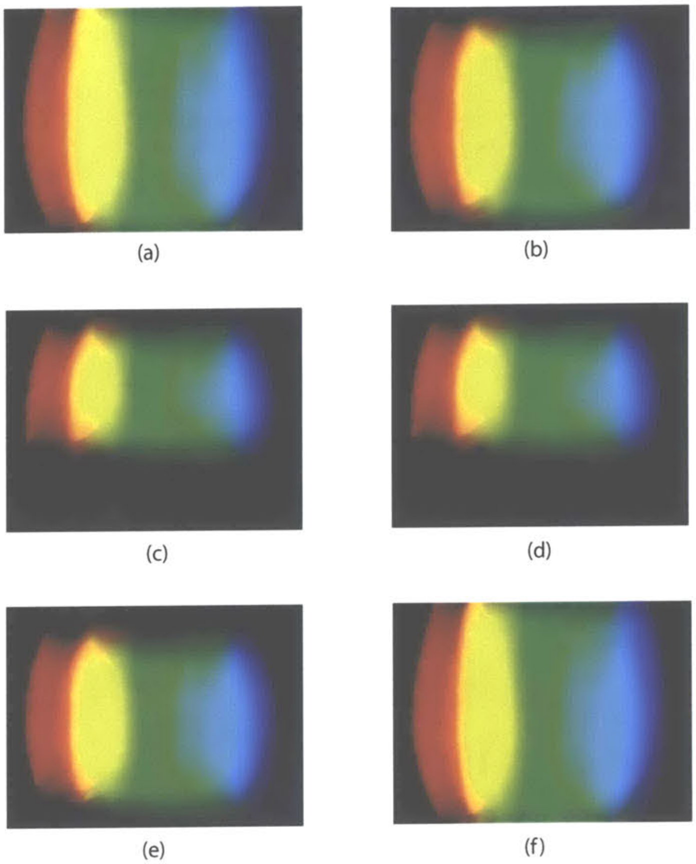

Figure 4-15: Spectral images of the "M" shape obeject while scanned at the position of (a) dashed line A, (b) dashed line B, (c) dashed line C, (d) dashed line D, (e) dashed line E, and (f) dashed line F as shown in Figure 4-14.

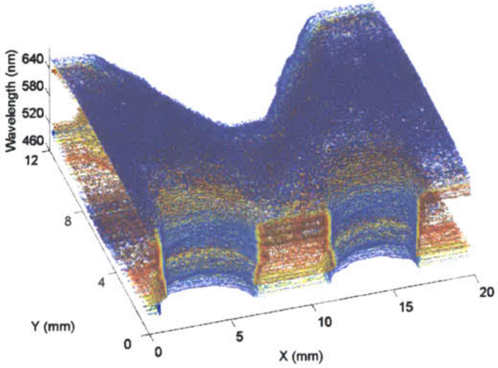

Figure 4-16: Reconstruction of the synthesized hyper-spectral image of the "M" shape object.

the image at $\lambda = 480$nm band is diminished compared to that at $\lambda = 630$nm band and vice versa when the object was coated with blue color.

To demonstrate the optical depth sectioning ability of the hyper-spectral VHI system, the reflecting mirror with "M" mask used in the previous experiment was tilted 1.5^o, so that the left edge of the "M" was 1.5mm closer to the imaging device than the right edge. The hyper-spectral VHI was set to focus at the depth of the right edge and lateral x scanning was implemented. The 2D images are extracted at the depth of the right edge of "M" and represented in $\lambda = 480$nm, 540nm and 630nm three channels. The image at $\lambda = 532$nm wavelength band is shown in Figure 4-19. It can be seen that the image is gradually attenuated along horizontal direction. This is because depth discrimination of the hyper-spectral VHI system. The image brightness variation along the y=4mm horizonal line is plotted in Figure 4-20. The brightness variation is not linear since the holographic lens diffracted intensity v.s. depth shift relation is nonlinear. With the exact physical parameter used in the experiments, this relation can be calculated by numerically integrating Eq.(2.34) or measured experimentally. Therefore, the surface profile of the tilted "M" can be reconstructed by inverting the brightness plot with the VHI depth selectivity curve. Figure 4-21 shows the surface profile at the height of 4mm. The surface profile is approximately liner, which agrees with the experiment setup that the object is a tilted flat mirror. The two little "humps" at approximate x=8 and 12mm were due to two scratches on the mirror surface. The accuracy of the surface profilometry in the depth direction is then characterized by the variation of the surface profile line with the two scratch "humps" filtered out. Consequently, the profilometry depth accuracy is around 15μm as shown Figure 4-21.

4.4 Summary

In this chapter, we first interpreted the wavelength degeneracy of VH lens by using the *K-sphere* approach. A rainbow illumination technique is applied to the VHI system to parallelize the imaging slits by wavelength multiplexing over the entire broadband

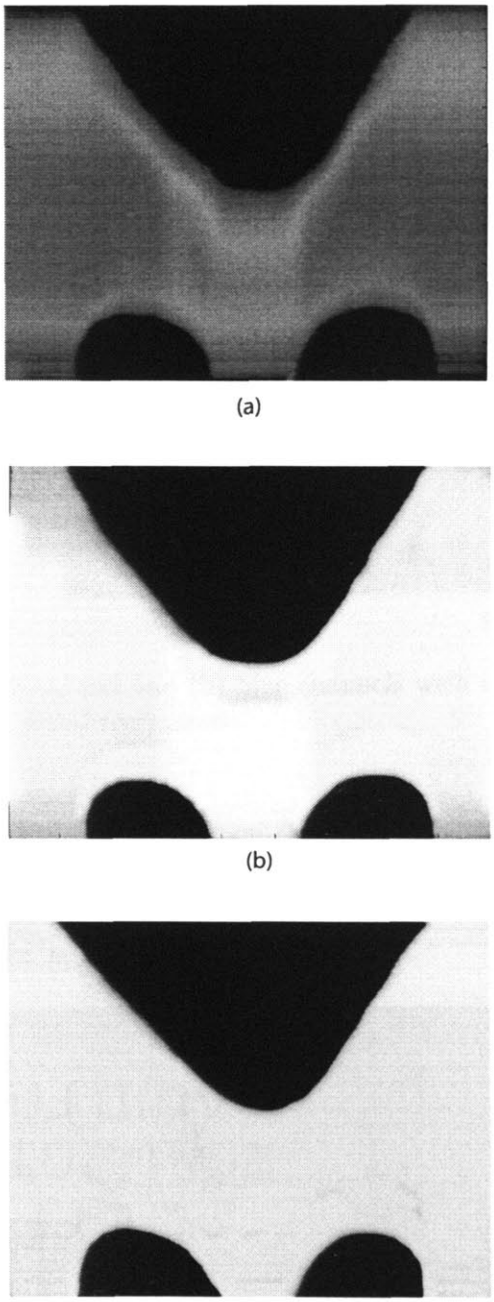

(a)

(b)

(c)

Figure 4-17: Images of the object "M" represented in (a)$\lambda = 480$nm, (b)$\lambda = 540$nm and (c)$\lambda = 630$nm imaging channels.

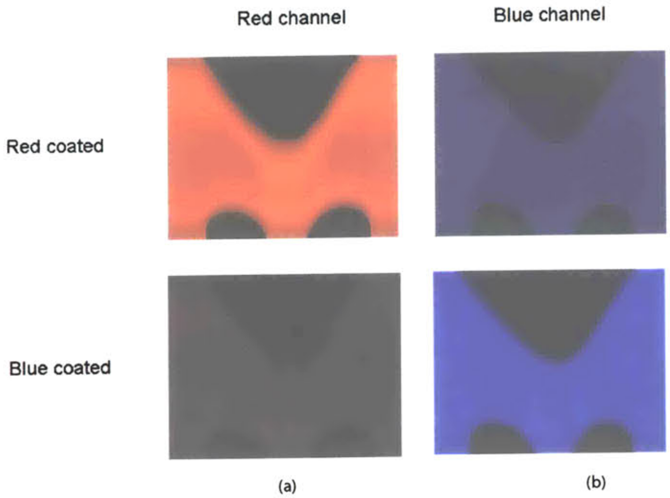

Figure 4-18: . Images at (a) red and (b) blue channels with the object coated with red(first row) and blue(second row) paint.

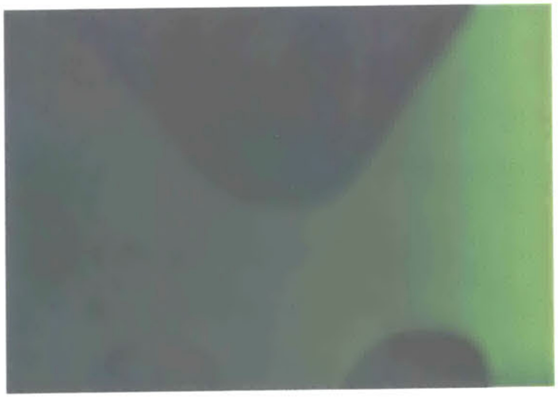

Figure 4-19: Raw image of the tilted object at the green channel.

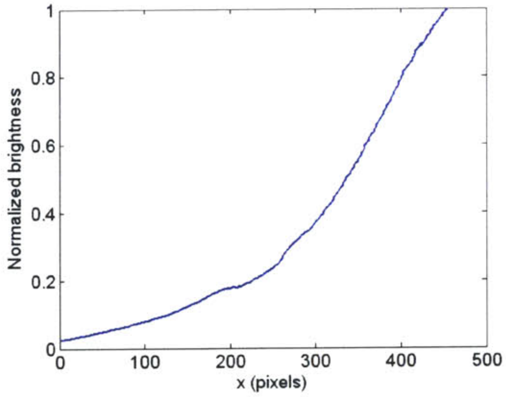

Figure 4-20: Crosssection of the raw brightness distribution across the tilt mirror. .

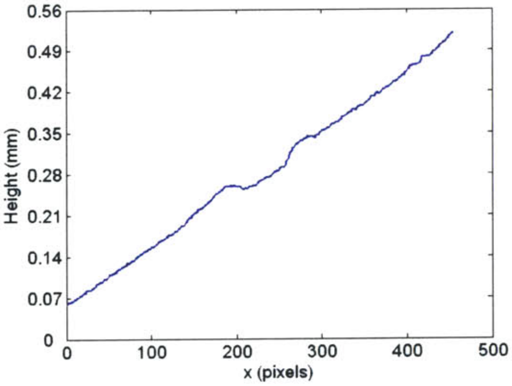

Figure 4-21: Crosssection of the restored surface profile of the tilt mirror.

spectrum. Theoretical analysis shows that the rainbow illumination has slightly degraded depth selectivity as compared to VHI using monochromatic illumination. Our experiments showed image quality comparable to that of monochromatic VHI system but with much larger FoV. Real-time VHI systems without scanning can be built based on this technique.

We also demonstrated a hyper-spectral imaging system design with the use of VH lenses. The hyper-spectral imaging system can investigate volumetric objects with high spatial resolution, and simultaneously acquire spectral information.

Chapter 5

Conclusion and future work

We have seen in this thesis as a 3D optical element the VH lens has rich functionalities in imaging applications. We showed that by using the VH lens as a pupil plane filter, some unique optical imaging properties which can not be realized with traditional lens, mirror, pinhole can be achieved. It has been presented in this thesis and our earlier publications that the VH lens has abundant application potential in areas such as long working distance, profilometry, spectral imaging, bio-imaging, chemical sensing, and *etc.* In this thesis, we mainly focused on investigation of the use of VH lens in profilometry. We first exploited the depth selectivity property of the VH lens, presented a laser illumination scanning VHI system with high resolution in profile profilometry. Then we focus our research interest on:

1. Improving the depth resolution over long working distance;
2. Reducing and eliminating scanning time to realize real time profilometry;
3. Exploiting the rich spectral filtering functionality of the VH lens for hyper-spectral imaging.

In this Chapter, we would like to firstly summarize this thesis in Section 5.1 and then discuss several potential directions which may be attractive in future research on this area.

5.1 Volume holographic profilometry summary

Our presentation in this thesis follows the following logic: First we quantitatively studied the unique optical behavior of the VH lens and formed a solid mathematical model based on 3D scalar diffraction theory. This model served as the basis to analyze various of our VHI designs. We then studied a specific class of the VH lens - the planar reference(PR) VH lens. The rest contents presented in this thesis are all concentrated on exploiting the rich functionalities and optimizing the profilometry imaging system based on the VH lens. We mainly address the two most important issues for optical profilometry: the *resolution improvement* and the *scanning reduction*. We studied the VHI system as a computational imaging system, therefore, besides optics design, we also devoted our efforts to post-processing algorithm study. Our goal of digital post-processing studies were also focused on the two main issues mentioned above. In the next several subsection, we would like to summarize them item by item in more details.

5.1.1 VH lens imaging frame work

The approach we took to study the general VH lens imaging behavior is to think of the VH lens as a spatial spectrum plane filter in a $4F$ system. The advantages of this approach are:

1. The VH lens optical properties are well described by its amplitude and phase modulation function $\epsilon(x, y, z)$. The optical interaction of the VH lens and the incident optical field can be explicitly written as a 3D filed filtering formation in the vicinity of the VH lens:

$$\mathbf{E}_{out}(x, y, z) = \mathbf{E}_{in}(x, y, z) \cdot \epsilon(x, y, z). \tag{5.1}$$

2. The two dimensional spatial spectrum filtering formulation is well developed. Therefore, it is very helpful to understand the unique optical properties of VH lens by comparing it with that of the 2D system.

The image at the output plane was obtained as (Eq.(2.3))

$$q_{3D}(x', y') = \sqrt{\eta} G_{3D} \left[\frac{x'}{\lambda f_2}, \frac{y'}{\lambda f_2}, \frac{1}{\lambda} \left(1 - \frac{x'^2 + y'^2}{2 f_2^2} \right) \right]$$

which is the 3D Fourier transform of the VH lens filtered optical field, evaluated on a parabolic 2D manifold. In comparison, the imaging formulation of the 2D system is given as:

$$q_{2D}(x', y') = G_{2D} \left(\frac{x'}{\lambda f_2}, \frac{y'}{\lambda f_2} \right). \tag{5.2}$$

The output image is the 2D Fourier transform of the filtered optical field, evaluated at the coordinates of $(x'/(\lambda f_2), y'/(\lambda f_2))$. It can be clearly seen that the 3D VH lens gives more degrees of freedom in designing the filtering function, as one more dimension can be used in design.

Based on this framework, we studied the shift variant imaging property a specific class of VH lens. We derived the angular selectivity, the shift degeneracy, and the wavelength degeneracy properties of the VH lens. The angular selectivity is exploited to generate depth selectivity by using the VH lens as a 3D pupil plane filter. The shift degeneracy allows the VHI system to image a line slit simultaneously. Therefore one lateral scanning is eliminated compared to using a pinhole as the filter. The wavelength degeneracy is the basis for rainbow illumination VHI to expand the VHI field of view from a slit to a wide window, thus the lateral scanning is totally eliminated.

5.1.2 Imaging with volume holographic lens

We have rigorously discussed the volume holograhic imaging with VH lens in this thesis. The straight line shaped refractive index modulation recorded in PR VH lens results in a straight degeneracy line. When probed with a unknown light source, the VHI system diffracts the Bragg-matched components of the incident illumination. The diffracted field is monitored by a detector or a detector array (CCD or CMOS camera). The diffracted field intensity captured by the detector is the "image" formed by the VHI system and can be used to determine the required object information like the 3D spatial and/or spectral characteristics of the object of interest.

We developed VHI system in the following three different categories:

1. **Monochromatic laser line scanning imaging system**: All the point sources along the y axis on the focal plane are Bragg matched simultaneously for imaging. Therefore, the line scanning scheme can be utilized in VHI for recovery of 3D and/or $2\frac{1}{2}$D objects.

2. **Rainbow illumination imaging system**: The illumination system for the object consists of a collimated white-light source, a diffraction grating to analyze it, and an achromatic cylindrical lens that focuses each color into a stripe. The color strips are oriented in the y dimension. The object is placed in the vicinity of the focal plane of the cylindrical lens. The light from the object is first directed to an objective lens and then diffracted from the volume hologram. A digital camera is placed on the diffracted beam arm at the Fourier plane of the collector lens. With this arrangement, we obtain depth-selective images simultaneously over the entire illuminated surface, *i.e.*, from each color in the rainbow.

3. **Hyper-spectral imaging system**: The hyper-spectral imaging system consists of a spectrographic subsystem and a rainbow VHI. The hyper spectral system uses a focused white light source as the illumination, therefore 2D scanning like the laser scanning system is necessary to encompass the entire object. The merit of the hyper-spectral system is that it can not only reconstruct the 3D spatial information of the object, but also capture the spectral information of the object with high resolution.

5.1.3 Digital post-processing

Our digital image post-processing study also focused on the two major issues in VHI: resolution improvement and scanning reduction. We studied the VHI imaging channel model based on treating the inter-layer and intra-layer imaging blur as an Inter-Symbol-Interference (ISI) function. Based on the object and image space discretization and digitization, we built two different imaging models according to different illumination schemes. The linear model for incoherent imaging, and the nonlinear model for coherent imaging. We studied the condition under which the coherent imaging post-processing can be approximated with the linear model with negligible error.

We formulated the image restoration problem as a ML estimation. We demonstrated the computational efficiency of using the Reduced Complexity Viterbi Algorithm (RCVA) to solve the ML problem, with the use of an object surface constraint. Both numerical simulation and experiments were implemented, the results showed the resolution can be improved by at least 5 times.

We also used the same digital processing approach to interpolate object features between the actual imaging scanning layers. Experimental results show interpolation of four depth layers by using the raw image information of one layer is applicable and the reconstruction error is very low with adequate illumination. We showed by combining the use of multiplexing multiple VH lenses and interpolation post-processing, the depth scanning can be eliminated.

5.2 Comparison to other 3D imaging methods

Figure 5-1 shows the potential applications of VHI profilometry. The horizontal axis is the desired resolution for the specific application, and the vertical axis denotes the typical working distance for the corresponding application. For example, the lower right corner of this chart denotes 3D microscopic imaging, where high resolution is highly desired, however the working distance can be very short. The most prevailing 3D imaging method in this area is confocal microscopy, two-photon and multi-photon absorption microscopy, *etc.*

We think it is worthwhile to quantitatively compare the VHI profilometry with other widely adapted optical 3D imaging methods in the following aspects: depth resolution, field of view, working distance, image time, post-processing, *etc.* The 3D

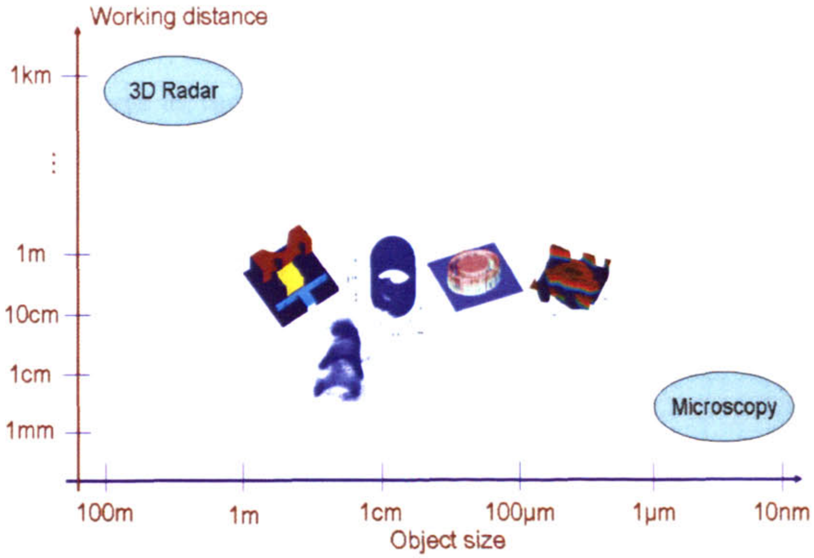

Figure 5-1: Applications of profilometry

imaging methods that we would like to compare to includes stereo imaging, depth from defocus, structured lighting, laser radar, *etc.*

1. **Stereo imaging** is one of the most widely used 3D imaging technique. It utilizes two or more cameras to capture images of the same object at several different view points. The depth information is acquired through parallax analysis with all these images. Stereo imaging is a passive profilometry method, *i.e.*, no active illumination is needed [65]. FoV is similar to regular photography, thus, imaging can be finished in real-time. The resolution of stereo imaging depends on the baseline between the two cameras or the baseline of the cameras array if multiple cameras are used, as well as the object distance. This is because the parallax analysis is based on triangulation calculation. For mid-range working distance ($\sim$ 1m), stereo imaging is able to achieve $<$ 1mm depth resolution. The lateral resolution is determined by the resolution of imagers. The downsides of stereo imaging is that to achieve high depth resolution, the baseline of the imaging system must be very long, or multiple imagers are needed to form a big camera array. Therefore, the system becomes bulky, costly and the image post-processing becomes complicated.

2. **Depth from defocus** utilize the shift-variant defocus response of regular imaging lenses, *i.e.*, the size of the defocus pattern increases with increasing defocus, to retrieve the depth information. Different from the stereo imaging, it deploys several cameras at the same view point, but with the lenses are set to focus at different depths. Therefore, the objects appears different defocus blur in all these images, and the differences can be used to estimate the object height map. Depth from defocus methods need multiple cameras to realize real time imaging. The depth resolution of depth from defocus is similar to that of the stereo imaging [66].

3. **Structured lighting** is another widely used 3D imaging method in machine vision. In this method, active lighting is necessary. A series of structured illumination patterns (usually black/white interlaced strips) are projected onto the object. The object height variation results in distortion of the structured lighting patterns. A regular photographic camera is used to capture images of these distorted illumination patterns. In the post-processing, the distortion is measured and used to calculate the height map of the object with triangulation [67].

4. **Laser radar** is a depth measuring method based on time-of-flight. In laser radar system, a visible or IR pulse laser is used to emitting optical pulses to the object. A high speed detector usually mounted beside the laser is used to received the reflected laser pulse. A very precise synchronization and time gating electronic system can measure the duration in which the laser pulse travels to the object and back to the detector. Once the time-of-flight is measured, the distance is known since the speed of light is a constant. Laser radar system usually works in long working distance applications (larger than hundreds of meters, typically several kilometers). The FoV is limited to the laser beam spot, usually scanning the laser beam is necessary to cover the entire object. The depth resolution of Laser radar is around 1cm for object at 100m away [68].

Compared to the typical existing optical profilometry techniques listed above, VHI realized profile measurement with simple monocular optics design with comparable depth resolution, though binocular or N-ocular VHI system can improve depth resolution. VHI designs discussed in this thesis need active illumination. However, it still possess a certain amount of depth discrimination ability at ambient illumination environment. The relatively weaker depth selectivity can still be useful in a number of applications, such as video matting [69]. Another advantage of VHI is with white light illumination (active or passive), it retrieves the spectral information of the object in addition to the 3D spatial information, forming four dimensional image.

5.3 Future work

So far, our profilometry imaging experiments are focused on applications with mid-range working distance (20cm to several meters) and medium resolution requirement (tens of microns to millimeters). Apparently, two major directions for future VHI profilometry system developments could be the applications denoted by the top left and low right corners as shown in Figure 5-1. The suggested future research can be summarized as

1. Long working distance profilometry system with the aim of resolution below 1 meter at the working distance at several kilometers. This system will be very useful for military reconnaissance, unmanned aviation vehicle navigation and related applications.

2. Short working distance high resolution bio-imaging. 3D microscopic imaging can be achieved with rainbow VHI in realtime. The main challenge of improving resolution is generating high quality illumination rainbow. This could be achieved by using novel broad band source, *e.g.* supercontinuum radiation [70, 71] from photonic crystal fiber [72].

3. We have restricted our analysis to simple Plane wave reference VH lens. However, it is not necessary that these systems should be optimal configuration for

every imaging applications

4. In Eq.(2.3), it can be seen the that output field is sampled at a parabolic manifold in the Fourier domain of the filtered optical field. This manifold is determined by the Fourier transforming lens. Therefore, it can be modified by using alternative optical elements, such as cubic phase maske, *etc.*

5. The nonliner 3D element can be used at the puiple plane to exploit even richer optical processing functionality.

Bibliography

[1] M. Born and E. Wolf. *Principles of optics.* The Cambridge University Press, Cambridge, UK, 7th edition, 1998.

[2] J. W. Goodman. *Introduction to Fourier Optics.* Mc Graw-Hill, New York, 2nd edition, 1996.

[3] D. J. Brady and Z. U. Rahman. Integrated analysis and design of analog and digital processing in imaging systems: introduction to feature issue. *Appl. Opt.*, 41(29):6049, 2002.

[4] W. T. Cathey and E. R. Dowski. New paradigm for imaging systems. *Appl. Opt.*, 41(29):6080–6092, 2002.

[5] C. J. R. Sheppard and C. J. Cogswell. Thress-dimensional imaging in confocal microscopy. In T. Wilson, editor, *Confocal Microscopy*, part 4, pages 143–169. Academic Press, San Diego, CA, 1990.

[6] D. Huang, E. A. Swanson, C. P. Lin, J. S. Schuman, W. G. Stinson, W. Chang, M. R. Hee, T. Flotte, K. Gregory, and C. A. Puliafito amd J. G. Fujimoto. Optical coherence tomography. *Science*, 254(5035):1178–1181, 1991.

[7] P. Grangeat. Mathematical framework of cone beam 3d reconstruction via the first derivative of the radon transform. In G. T. Herman, A. K Louis, and F. Natterer, editors, *Lecture Notes in Mathematics 1497: Mathematical Methods in Tomography.* Springer-Verlag, Berlin, 1991.

[8] D. Marr. *Vision.* W. H. Freeman & Co., New York, 1982.

[9] K. J. Gåsvik. *Optical Metrology.* Wiley and Sons, New York, 3rd edition, 2002.

[10] M. Minsky. Microscopy apparatus. US Patent 3,013,467, 12 1961. This is a full MISC entry.

[11] T. Wilson. *Confocal Microscopy.* Academic Press, San Diego, CA, 1990.

[12] G. Binnig, C. F. Quate, and C. Gerber. Atomic force microscope. *Phys. Rev. Lett.*, 56(9):930–933, 1986.

[13] G. Binnig, H. Rohrer, C. Gerber, and E. Weibel. 7×7 reconstruction on si(111) resolved in real space. *Phys. Rev. Lett.*, 50(2):120–123, 1983.

[14] W. Sun, A. Sinha, G. Barbastathis, and M. A. Neifeld. High-resolution volume holographic profilometry using the viterbi algorithm. *Opt. Lett.*, 30:1297–1299, 2005.

[15] E. Trucco and A. Verri. *Introductory Techniques for 3-D Computer Vision.* Prentice Hall, 1st edition, 1998.

[16] H. J. Tiziani, A. Rothe, and N. Maier. Dual-wavelength heterodyne differential interferometer for high-precision measurements of reflective aspherical surfaces and step heights. *Appl. Opt.*, 35:3525–3533, 1996.

[17] A. Sinha, W. Sun, T. Shih, and G. Barbastathis. Volume holographic imaging in transmission geometry. *Appl. Opt.*, 43:1533–1551, 2004.

[18] E. Hecht. *Optics.* Addison Wesley, 4th edition, 2001.

[19] P. J. van Heerden. Theory of optical information storage in solids. *Appl. Opt.*, 2(4), 1963.

[20] D. Gabor. A new microscopic principle. *Nature*, 161:777–779, 1948.

[21] E. Leith and J. Upatnieks. Wavefront recsontruction and communication theory. *J. Opt. Soc. Am.*, 52:1123–1134, 1962.

[22] J. Zhang, B. Tao, and J. Katz. Thress-dimensional velocity measurements using hybrid hpiv. In R. J. Adrian, D. F. G. Durao, F. Durst, M. V. Heitor, M. Maeda, and J. H. Whitelaw, editors, *Developments in Laser Techniques and Fluid Mechanics.* Springer-Verlag, Berlin, 1997.

[23] T. Zhang and I. Yamaguchi. Three-dimensional microscopy with phase-shifting deigital holography. *Opt. Lett.*, 23(15), 1998.

[24] J. H. Milgram and W. Li. Computational reconstruction of images from holograms. *Appl. Opt.*, 41(5):853–864, 2002.

[25] E. N. Leith, A. Kozma, J. Upatnieks, J. Marks, and N. Massey. Holographic data storage in three-dimensional media. *Appl. Opt.*, 5(8):1303–1311, 1966.

[26] H. Kogelnik. Coupled wave theory for thick hologram gratings. *Bell Syst. Tech. J.*, 48(9):2909–2947, 1969.

[27] D. Psaltis. Parallel optical memories. *Byte*, 17(9):179, 1992.

[28] D. Psaltis and F. Mok. Holographic memories. *Sci. Am.*, 273(5):70–76, 1995.

[29] J. F. Heanue, M. C. Bashaw, and L. Hesselink. Volume holographic storage and retrieval of digital data. *Science*, 265(5173):749–752, 1994.

[30] H. Lee, X.-G. Gu, and D. Psaltis. Volume holographic interconnections with maximal capacity and minimal cross talk. *J. Appl. Phys.*, 65(6):2191–2194, 1989.

[31] D. Brady, S. Lin, X. G. Gu, and D. Psaltis. Holography in artificial neural networks. *Nature*, 343:325–330, 1990.

[32] Y. S. Abu-Mostafa and D. Psaltis. Optical neural computers. *Sci. Am.*, 256(3):66–73, 1987.

[33] J. Hong. Applications of photorefractive crystals for optical neural networks. *Opt. Quant. Electr.*, 25(9):S551–S568, 1993.

[34] D. J. Brady, A. G.-S. Chen, and G. Rodriguez. Volume holographic pulse shaping. *Opt. Lett.*, 17(8):610–612, 1992.

[35] P.-C. Sun, Y. T. Mazurenko, W. S. C. Chang, P. K. L. Yu, and Y. Fainman. All-optical parallel-to-serial conversion by holographic spatial-to-temporal frequency encoding. *Opt. Lett.*, 20(16):1728–1730, 1995.

[36] P.-C. Sun, Y. Fainman, Y. T. Mazurenko, and D. J. Brady. Space-time processing with photorefractive volume holography. In *SPIE Proceedings*, number 2529, pages 157–170, 1995.

[37] K. Purchase, D. Brady, G. Smith, S. Roh, M. Osowski, and J. J. Goleman. Integrated optical pulse shapers for high-bandwidth packet encoding. In *SPIE Proceedings*, number 2613, pages 43–51, 1996.

[38] D. M. Marom, P.-C. Sun, and Y. Fainman. Analysis of spatial-temporal converters for all-optical communication links. *Appl. Opt.*, 37(14):2858–2868, 1998.

[39] C. Mead. Neuromorphic electronic systems. In *Proc. IEEE*, number 78 in 90, pages 1629–1636, 1990.

[40] C. A. Mead. Scaling of mos technology to submicrometer feature sizes. *Analog Int. Circ. & Signal Proc.*, 6(1):9–25, 1994.

[41] H. Coufal, D. Psaltis, and eds G. Sincerbox. *Holographic Data Storage*. Springer-Verlag, New York, 1st edition, 2000.

[42] G. Barbastathis, M. Balberg, and D. J. Brady. Confocal microscopy with a volume holographic filter. *Opt. Lett.*, 24(12):811–813, 1999.

[43] A.Sinha and G. Barbastathis. Volume holographic telecscope. *Opt. Lett.*, 27(5):1690–1692, 2002.

[44] A.Sinha and G. Barbastathis. Volume holographic imaging for surface metrology at long working distances. *Opt. Exp.*, 11(24):3202–3209, 2003.

[45] W. Liu, D. Psaltis, and G. Barbastathis. Real time spectral imaging in three spactial dimensions. *Opt. Lett.*, 27(5):854–856, 2002.

[46] G. Barbastathis, M. Levene, and D. Psaltis. Shift-multiplexing with spherical referece waves. *Appl. Opt.*, 35:2403–2417, 1996.

[47] G. Barbastathis and D. Psaltis. Shift-multiplexed hologaphic memory using the two-lambda method. *Opt. Lett.*, 21(6):429–431, 1996.

[48] D. Psaltis, F. Mok, and H.Y.-S Li. Nonvolatile storage in photorefractive crystals. *Opt. Lett.*, 19(3):210–212, 1994.

[49] W. Sun, G. Barbastathis, and M. A. Neifeld. Maximum likelihood restoration of volume holographic profilometery images at long working distance, in submission to. *Appl. Opt.*, 2005.

[50] W. Sun, G. Barbastathis, and M. A. Neifeld. Super-resolution optical profilometry using maximum likelihood estimation. Frontier in Optics, paper FThM4, Tucson, AZ.

[51] G. Forney. The viterbi algorithm. In *Proc. IEEE*, number 61, pages 268–278, 1973.

[52] C. Miller, B. Hunt, M. Marcellin, and M. Neifeld. Image restoration with the viterbi algorithm. *J. Opt. Soc. Am. A.*, 17:265–275, 2000.

[53] K. R. Castleman. *Digital image processing.* Prentice Hall, 1st edition, 1995.

[54] M. Petran and M. Hardravsky. Tandem-scanning reflection-light microscope. *J. Opt. Soc. Am.*, 58:661–664, 1968.

[55] S. Yin, G. Lu, J. Zhang, F. T. S. Yu, and J. N. Mait. Kinoform-based nipkow disk for a confocal microscope. *Appl. Opt.*, 34:5695–5698, 1995.

[56] M. A. Browne, O. Akinyemi, and A. Boyde. Confocal surface profiling utilizing chromatic aberration. *Scanning*, 14:145–153, 1992.

[57] H. J. Tiziani and H. M Uhde. 3-dimensional image sensing by chromatic confocal microscopy. *Appl. Opt.*, 33:1838–1843, 1994.

[58] M. Maly and A. Boyde. Real-time stereoscopic confocal reflection microscopy using objective lenses with linear longitudinal chromatic dispersion. *Scanning*, 16:187–192, 1994.

[59] S. L. Dobson, P. Sun, and Y. Fainman. Diffractive lenses for chromatic confocal imaging. *Appl. Opt.*, 34:4744–4748, 1997.

[60] P. C. Lin, P. Sun, L. Zhu, and Y. Fainman. Single-shot depth-section imaging through chromatic slit-scan confocal microscopy. *Appl. Opt.*, 37:6764–6770, 1998.

[61] S. Cha, P. C. Lin, L. Zhu, P. Sun, and Y. Fainman. Nontranslational three-dimensional profilometry by chromatic confocal microscopy with dynamically configurable micromirror scanning. *Appl. Opt.*, 39, 2000.

[62] W. Liu, G. Barbastathis, and D. Psaltis. Volume holographic hyperspectral imaging. *Appl. Opt.*, 43:3581–3599, 2004.

[63] A. Sinha and G. Barbastathis. Broadband voulume holographic imaging. *Appl. Opt.*, 43:5214–5221, 2004.

[64] W. Sun, K. Tian, and G. Barbastathis. Hyper-spectral imaging with volume holographic lenses. Conference on Laser and Electro-Optics (CLEO), paper CFP2, Baltimore, MD.

[65] W. E. L. Grimson. *A Computational Study of the Human Early Visual System.* MIT Press, Cambridge, MA, 1st edition, 1981.

[66] Yalin Xiong and Steven Shafer. Depth from focusing and defocusing. Technical Report CMU-RI-TR-93-07, Robotics Institute, Carnegie Mellon University, Pittsburgh, PA, March 1993.

[67] P. S. Huang and S. Zhang. 3-d optical measurement using phase shifting based methods. In *Proc. SPIE 6000*, Boston, MA.

[68] J. Busck and H. Heiselberg. Gated viewing and high-accuracy three-dimensional laser radar. *Appl. Opt.*, 43:4705–4710, 2004.

[69] W. Sun, S. OH, K. Tian, Z. Xu, and G. Barbastathis. Volume holographic imaging with natural and supercontinuum illumination. MIT Microsystems Annual Research Conference, Waterville valley, NH.

[70] J. K. Ranka, R. S. Windeler, and A. J. Stentz. Visible continuum generation in air-silica microstructure optical fibers with anomalous dispersion at 800nm. *Opt. Lett.*, 25:25–27, 2000.

[71] Goëry Genty. *Supercontinuum generation in microstructured fibers and novel optical measurement techniques.* PhD thesis, Helsinki University of Technology, 2004.

[72] J. C. Knight, T. A. Birks, P. S. Russell, and D. M. Atkin. All-silica single-mode optical fiber with photonic crystal cladding. *Opt. Lett.*, 21:1547–1549, 1996.